e-ISSN 2150-5551
CN 31-2103/TB

Nano-Micro Letters

REVIEW

https://doi.org/10.1007/s40820-023-01196-1

Advances on Axial Coordination Design of Single-Atom Catalysts for Energy Electrocatalysis: A Review

Cite as
Nano-Micro Lett.
(2023) 15:228

Received: 4 June 2023
Accepted: 28 August 2023

Linjie Zhang[1], Na Jin[1,2], Yibing Yang[1], Xiao-Yong Miao[3], Hua Wang[4], Jun Luo[4] ✉, Lili Han[1] ✉

HIGHLIGHTS

- The burgeoning research topic of axially coordinated single-atom catalysts (SACs) is briefly outlined in this review.
- A comprehensive summary of the recent advances on synthetic strategies and electrocatalytic applications of axially coordinated SACs is provided.
- The challenges and outlooks for future axially coordinated SACs study have been emphasized.

ABSTRACT Single-atom catalysts (SACs) have garnered increasingly growing attention in renewable energy scenarios, especially in electrocatalysis due to their unique high efficiency of atom utilization and flexible electronic structure adjustability. The intensive efforts towards the rational design and synthesis of SACs with versatile local configurations have significantly accelerated the development of efficient and sustainable electrocatalysts for a wide range of electrochemical applications. As an emergent coordination avenue, intentionally breaking the planar symmetry of SACs by adding ligands in the axial direction of metal single atoms offers a novel approach for the tuning of both geometric and electronic structures, thereby enhancing electrocatalytic performance at active sites. In this review, we briefly outline the burgeoning research topic of axially coordinated SACs and provide a comprehensive summary of the recent advances in their synthetic strategies and electrocatalytic applications. Besides, the challenges and outlooks in this research field have also been emphasized. The present review provides an in-depth and comprehensive understanding of the axial coordination design of SACs, which could bring new perspectives and solutions for fine regulation of the electronic structures of SACs catering to high-performing energy electrocatalysis.

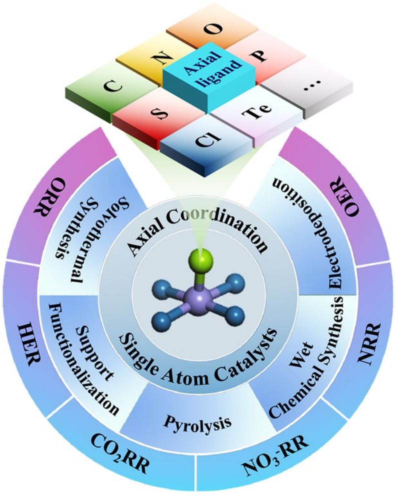

KEYWORDS Single-atom catalyst; Axial coordination; Synthetic strategy; Electrocatalytic application

---

✉ Jun Luo, jluo@uestc.edu.cn; Lili Han, llhan@fjirsm.ac.cn
[1] State Key Laboratory of Structural Chemistry, Fujian Institute of Research on the Structure of Matter, Chinese Academy of Sciences, Fuzhou 350002, People's Republic of China
[2] College of Chemistry and Materials Science, Fujian Normal University, Fuzhou 350117, People's Republic of China
[3] State Key Laboratory of ASIC and System, Shanghai Institute of Intelligent Electronics and Systems, School of Microelectronics, Fudan University, Shanghai 200433, People's Republic of China
[4] ShenSi Lab, Shenzhen Institute for Advanced Study, University of Electronic Science and Technology of China, Shenzhen 518110, People's Republic of China

1 Introduction

In the context of significant global interest in the low-carbon economy, energy issues have received intensive attention over the past decade. Despite fossil fuels currently serving as the primary energy source worldwide, their excessive utilization and various drawbacks, including land degradation, ecological deterioration, air pollution and greenhouse effect have compelled humans to explore clean and renewable low-carbon/zero-carbon energy alternatives [1, 2]. Developing sustainable and eco-friendly energy conversion technologies is crucial in addressing the growing global demand for energy while mitigating environmental concerns, including fuel cells, metal-air batteries, water electrolysis, CO_2 reduction to value-added chemicals and/or fuels, and N_2 fixation for ammonia synthesis [3, 4]. Electrochemical reactions such as oxygen reduction reaction (ORR) [5, 6], hydrogen evolution reaction (HER) [7, 8], oxygen evolution reaction (OER), CO_2 reduction reaction (CO_2RR) [9, 10], and N_2 reduction reaction (NRR) [11–13] catalyzed by electrocatalysts have seen a series of advances in these technologies [14]. Electrocatalysts play a pivotal role in these electrochemical processes [15], as they can significantly accelerate the reaction kinetics by reducing the energy barriers and altering reaction pathways, thereby improving overall energy conversion efficiency.

Developing efficient electrocatalysts is a crucial determinant for the future industrial-scale implementation of electrochemical reactions in energy conversion and storage technologies [16]. In recent years, the high efficiency of numerous electrocatalysts has been confirmed, including platinum (Pt) group metals (PGMs) [17], carbon-based metal-free catalysts [18], single-atom catalysts (SACs) [19] and so on. PGM-based catalysts exhibit superior catalytic performance, yet their exorbitant cost and limited availability impede their further development and application [20]. Despite the abundance and structural versatility of carbon-based metal-free catalysts, there remains lack of understanding regarding their doping effects and structural diversity [21]. Since Qiao et al. [22] discovered Pt_1/FeO_x SAC for CO oxidation in 2011, transition metal-based SACs have been extensively investigated for their remarkable electrocatalytic activity and promising development prospects. Particularly those transition metal-based SACs loaded on nitrogen (N)-doped carbon (M–N–C) [23], benefiting from their unique electronic and geometric structures as well as maximum atom utilization efficiency, they could exhibit diverse adsorption behaviors, and thus adjustable catalytic performance [24]. For instance, Wan et al. [25] demonstrated the application of concave Fe–N–C SAC for ORR catalysis in fuel cells, which has successfully met the activity target set by the United States in 2018 without resorting to a PGM catalyst. Currently, research on M–N–C type SACs has become a hot topic in electrocatalysis [26–28].

As widely recognized, the catalytic performance of SACs is determined by the intrinsic activity of their central atoms [29]. Specifically, the adsorption of active intermediates is constrained by the inherent properties of a single atomic site [30] and surface electronic structure [31]. Therefore, various types of metals have been tested as the atomic center, including conventional PGMs such as Pt and non-PGMs represented by Fe, Co and Ni [32]. In addition, the electrocatalytic activity of SACs can be further enhanced by precisely fine-tuning their structure [33], such as exploiting the interaction between metal atoms and supports, heteroatoms, and even adjacent metal atoms [34]. Up to now, numerous studies have been conducted to optimize the local structure of SACs for enhanced electrocatalytic performance [35–37]. Various methods including coordination engineering, heteroatom doping, construction of double or multiple atomic sites, support structure regulation, and catalytic site coupling have been proposed to regulate SACs [38, 39]. Among them, coordination engineering has been extensively studied in recent years as an effective approach to enhance the performance of SACs [40]. For instance, Yang et al. [41] prepared Mn-SAC with dual O and N atom coordination ($Mn–N_3O_1$) which demonstrated superb ORR performance. In the active site of $Mn–N_3O_1$, the coordination of O and N atoms tunes the *d-band* electronic structure of Mn to the optimal state, thereby exhibiting the fastest ORR kinetics. Guided by density functional theory (DFT) calculations, Chen et al. [42] synthesized $Co_1–N_3PS/HC$ SAC with single Co atom coordinated to N, P and S, which exhibited excellent ORR activity with a half-wave potential ($E_{1/2}$) of 0.920 V in alkaline medium. Besides, in electrocatalytic CO_2 reduction, the optimized $Co–N_2C_2$ active sites displayed higher activity and selectivity compared to the prototypical $Co–N_4$ active sites [43]. In OER electrocatalysis, a single Ni atom coordinated with either O or both N and S exhibited superior performance compared to traditional $Ni–N_4$ sites [44, 45]. At the same time, with the development of

https://doi.org/10.1007/s40820-023-01196-1

characterization techniques such as spherical aberration-corrected high-angle annular dark field scanning transmission electron microscopy (AC HAADF-STEM), X-ray photoelectron spectroscopy (XPS), synchrotron radiation-based X-ray absorption spectroscopy (X-ray absorption structure spectroscopy (XANES) and extended X-ray absorption spectrum fine structure (EXAFS) and in combination with DFT simulation, the exact position and geometric structure of single atoms, the valence state and the atomic coordination environment can be clearly identified [46], thus promoting the knowledge about coordination regulation principle and gaining understanding of the structure–activity interplay in SACs.

Over the past two years, inspired by the active iron sites of natural enzymes like horseradish peroxidase (HRP) and cytochrome c oxidases (CcO), Fe–N–C-based SACs with penta-coordinated heme-like active site structure (Fe–N_5–C) have attracted great attention in electrocatalysts [47–51]. The fifth N ligand in the axial direction could exert an electron pull–push effect and/or steric effect on the single-atom sites, which modulates the binding strength between the active sites and reaction intermediates and consequently enhanced the activity of the axially modified SACs. In this background, axial coordination engineering is proposed to be a new coordination tuning method for tuning local coordination structure of the single-atom sites in SACs. In contrast to typical M–N_4 SACs, the axial coordination design will bring forth new types of coordination configurations that hold great potential for achieving significantly boosted catalytic activity in certain active site-specific catalysis applications. By introducing one or multiple additional ligands in the axial position perpendicular or non-coplanar to the planar M–N_4 sites in SACs, it is anticipated that the electron distribution symmetry will be disrupted and the electronic structure of the central single-atom active sites will be efficiently altered, thus optimizing the adsorption behavior and decreasing energy barriers for the intermediate sorption. Moreover, the axial ligand introduced over the central single-atom sites could alternatively serve as the new adsorption site to synergize with the M–N_4 site for catalysis, ultimately changing the reaction pathways to be more energetically favorable. To date, various ligands such as N-containing ligands [52] (N, NH_2, macrocyclic compounds, etc.), O-containing ligands [53] (O, OH, etc.), halogen-containing ligands [54] (Cl, Br, I), carbon-containing ligands (C, CNT, graphene, etc.), metal-containing ligands (PtO_2, Te cluster, etc.) and other types of ligands have been introduced to the axial position of SACs. Figure 1 depicts the recently reported as well as the potential axial coordination configurations of SACs based on the classical planar MN_4 configuration. The axial coordination could significantly alter the electrocatalytic performance of SACs by introducing external atoms, functional groups, and even molecules into the metal atom center of SACs [55]. Through the axial coordination design of SACs, novel properties are conferred upon the central metal atom, thereby enabling regulation of the electrocatalytic activity, selectivity and stability of SACs. Generally, axial ligands serve three primary functions: (1) anchoring functional complex onto the electrode surface; (2) serving as molecular wires to facilitate electron transport between the electrode and metal center; (3) modifying the electron density of the metal center and altering its reactivity [56]. In this review, we will focus on the discussion of the recent development of axial coordination modification of SACs for electrocatalytic applications in energy conversion. We first provide a comprehensive summary of various synthetic strategies employed for achieving axial-coordinated SACs. Furthermore, we present a comprehensive demonstration of the efficacy of axial coordination design of SACs in energy electrocatalysis, encompassing a range of reactions including ORR, CO_2RR, HER, OER, NRR and beyond.

2 Synthetic Strategies of Axial Coordination Design of SACs

Due to the high surface energy of atoms, aggregation and deactivation are prone to occur during the preparation and catalytic processes, which imposes higher requirements on the synthetic process of SACs [57]. Therefore, reviewing the synthetic strategies is instrumental in establishing a theoretical basis for innovative endeavors aimed at proposing more efficient approaches in the future. So far, many strategies have been developed for the synthesis of axially coordinated SACs, with high-temperature pyrolysis being the most commonly employed method. However, precise control of catalyst structure is challenging due to the intricate reaction mechanisms at elevated temperatures. Therefore, alternative methods have been further developed and provide a solid foundation for constructing axially coordinated SACs with well-defined structures. In this section, we present a summary of the latest synthetic strategies for designing axially

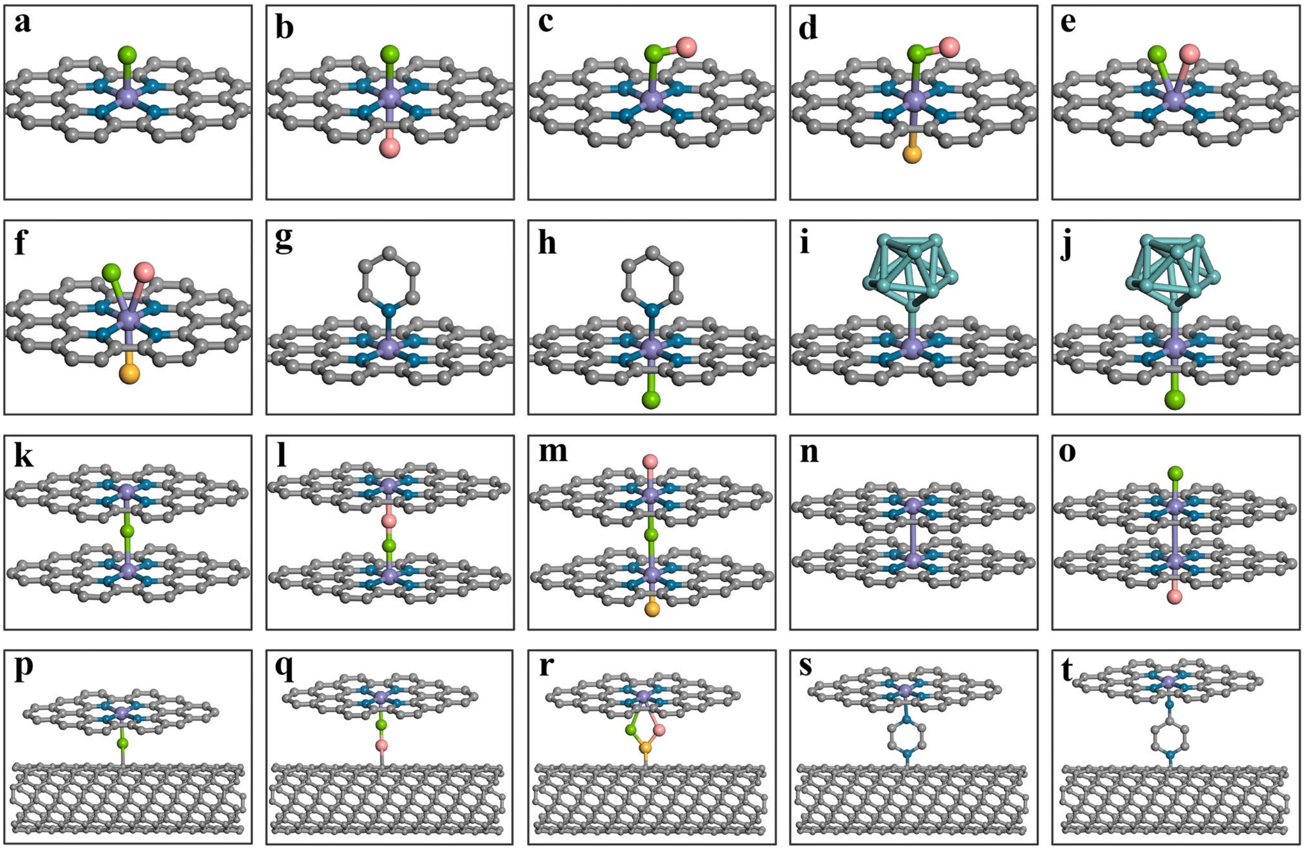

Fig. 1 Representative and proposed possible configurations of axial ligand (denoted by letter X) coordinated MN_4 SACs. **a** MN_4 SAC with one axial ligand ($X–MN_4$). **b** MN_4 SAC with two axial ligands in opposite direction ($X_1–MN_4–X_2$). **c** MN_4 SAC with one axial group ligand ($X_1–X_2–MN_4$). **d** MN_4 SAC with one axial ligand and one axial group ligand in opposite direction ($X_1–X_2–MN_4–X_3$). **e** MN_4 SAC with two axial ligands in the same direction ($X_1/X_2–MN_4$). **f** MN_4 SAC with two axial ligands in the same direction and one axial ligand in the opposite direction ($X_1/X_2–MN_4–X_3$). **g** MN_4 SAC with one axial pyridine ligand ($Py–MN_4$). **h** MN_4 SAC with one axial pyridine ligand and one axial ligand in opposite direction ($Py–MN_4–X$). **i** MN_4 SAC with one axial metal cluster ligand ($M_{cluster}–MN_4$). **j** MN_4 SAC with one axial metal cluster ligand and one axial ligand in the opposite direction ($M_{cluster}–MN_4–X$). **k** Two MN_4 SACs bridged by one axial ligand in between ($MN_4–X–MN_4$). **l** Two MN_4 SACs bridged by two axial ligands in between ($MN_4–X_1–X_2–MN_4$). **m** Two MN_4 SACs bridged by one axial ligand in between and with one axial ligand in each of the opposite direction ($X_2–MN_4–X_1–MN_4–X_3$). **n** Two MN_4 SACs axially bridged by their central metal atoms ($MN_4–MN_4$). **o** Two MN_4 SACs axially bridged by their central metal atoms and with one axial ligand in each of the opposite direction ($X_1–MN_4–MN_4–X_2$). **p** MN_4 SAC with one axial ligand grafted on CNT support ($MN_4–X–CNT$). **q** MN_4 SAC with one axial group ligand grafted on CNT support ($MN_4–X_1–X_2–CNT$). **r** MN_4 SAC with two axial ligands in the same direction and co-grafted on CNT support ($MN_4–X_1/X_2–X_3–CNT$). **s** MN_4 SAC with one axial pyrazine ligand grafted on CNT support ($MN_4–Pyr–CNT$). **t** MN_4 SAC with one axial 4-pyridylamine ligand grafted on CNT support ($MN_4–NH_2–Py–CNT$)

coordinated SACs, including high-temperature pyrolysis, solvothermal synthesis, wet chemical synthesis, support functionalization method, and electrodeposition method.

2.1 High-Temperature Pyrolysis

High-temperature pyrolysis is a commonly employed method for the preparation of axially coordinated SACs, involving calcination of precursors under an inert atmosphere at temperatures ranging from 600 to 1000 °C [58]. Xiao et al. [59] successfully prepared atomically dispersed Fe–N–C SAC through a one-step pyrolysis of the ZIF-8 precursor. During this process, Fe atoms were immobilized within the N-doped porous carbon skeleton through coordination with four N atoms in the plane and two O atoms in the axial direction. Similarly, $Ni–N_4–O/C$ catalysts with O axial coordination were synthesized by Wang et al. [60] via direct carbonizing of the precursor followed by acid etching (Fig. 2a). Through EXAFS curve fitting analysis of $Ni–N_4–O/C$, precise structural parameters surrounding the central Ni atom

https://doi.org/10.1007/s40820-023-01196-1

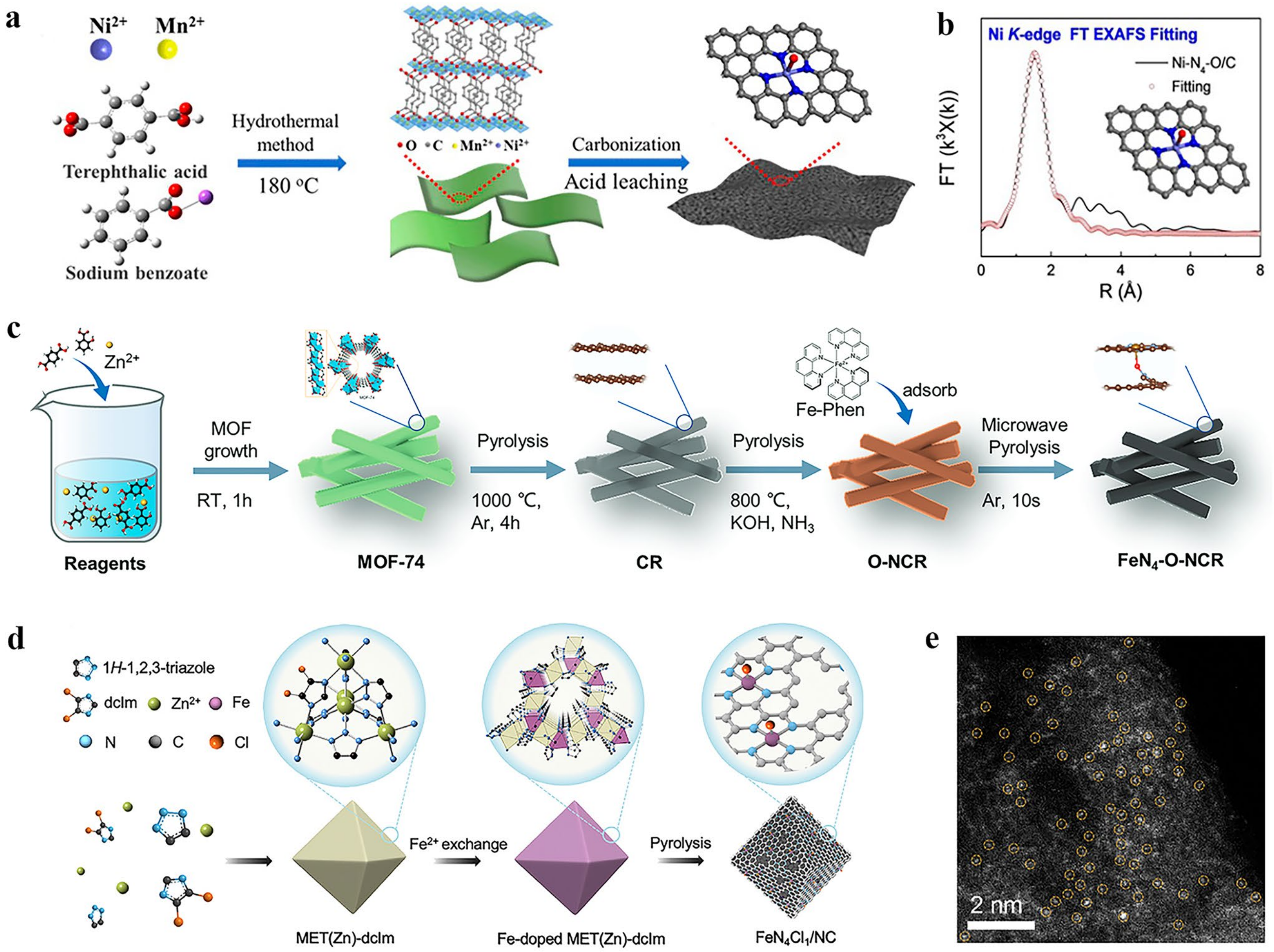

Fig. 2 Synthesis of SACs with axial coordination by high-temperature pyrolysis. **a** Illustration of the synthetic process of Ni–N_4–O/C. **b** EXAFS fitting curve of Ni–N_4–O/C in R space, inset is the corresponding schematic model of Ni–N_4–O/C. Reproduced with permission [60]. Copyright: 2020, Wiley-VCH GmbH. **c** Schematic illustration of the synthesis of FeN4–O–NCR catalyst. Reproduced with permission [61]. Copyright: 2022, Wiley-VCH GmbH. **d** Preparation route and **e** AC HAADF-STEM image of FeN_4Cl_1/NC. Reproduced with permission [64]. Copyright: 2022, Wiley-VCH GmbH

were obtained, which further elucidated that the coordination configuration of single Ni atom adopts a planar Ni–N_4 configuration with one axial Ni–O bond (Fig. 2b). Besides direct high-temperature pyrolysis, stepwise pyrolysis is also a viable and important method for preparing SACs. Peng et al. [61] initially subjected the MOF-74 precursor to pyrolysis at 1000 °C in an Ar atmosphere, resulting in the formation of one-dimensional carbon nanorods. Subsequently, they employed a molten salt (KOH) assisted pyrolysis strategy under NH_3 atmosphere to prepare O, N-doped carbon nanorods (O–NCR). The Fe-phenanthroline complex was then electrostatically adsorbed onto the O-NCR, and rapid microwave-assisted carbonization was performed to yield the final axially coordinated FeN_4–O–NCR catalyst (Fig. 2c). The Fe K-edge X-ray absorption spectroscopy (XAS) was employed to determine the detailed atomic structures of FeN_4–O–NCR and FeN_4/CR. The Fe K-edge XANES spectra of both samples exhibit a close resemblance to that of iron phthalocyanine (FePc), indicating the presence of cationic Fe states in the sample. The fitting results indicate that the average oxidation state of Fe in FeN_4–O–NCR (+2.7) is higher than that in FeN_4/C (+2.4). This higher average valence of Fe in FeN_4–O–NCR is consistent with the presence of an additional axial O ligand bound to Fe. The average Fe–N distances of FeN_4–O–NCR and FeN_4/CR in R space are 1.97 and 1.99 Å, respectively, indicating that the planarity of FeN_4 moiety is not significantly altered by the presence of axial O ligand.

However, the preparation of axially coordinated SACs may not always be achieved by a simple high-temperature pyrolysis method alone, which has prompted researchers to explore its combination with other techniques. For example, after synthesizing Fe/N-G-800 catalysts through high-temperature pyrolysis at 800 °C, Xu et al. [62] employed impregnation method to anchor FePc molecules onto the Fe/N-G-800 matrix via axial coordination, resulting in the final product of Fe@Fe/N-G-800 catalyst. The XAS measurements were utilized to investigate the chemical environment of Fe atoms in Fe@Fe/N-G-800, revealing that the oxidation state of Fe is between + 2 and + 3 based on the Fe K-edge XANES results. Besides, EXAFS spectroscopy results confirmed that the Fe species in Fe/N-G-800 predominantly exist in the atomically dispersed Fe–N_4 and Fe–O configurations, with coordination numbers of 3.8 and 1.0, respectively. Therefore, an axial O bridge bond of Fe–O–Fe and an O–FeN_4 structure were proposed. In the course of synthesizing Sn–N–C SAC with O axial coordination, Luo et al. [63] employed multiple pyrolysis steps in conjunction with additional processes of reflux and ball milling. Prior to high-temperature pyrolysis of the precursor for obtaining the axial Cl-coordinated FeN_4Cl_1/NC catalyst, Hu et al. [64] employed a post-synthetic ion-exchange technique to substitute partial Zn^{2+} ions in MET (Zn)-dcIm nanocrystals with Fe^{2+} ions, which facilitated the subsequent pyrolysis (Fig. 2d, e).

2.2 Solvothermal Synthesis

Due to its ease of operation, simplicity of procedures, and high level of safety compared with the high-temperature pyrolysis method, solvothermal method has gained widespread popularity for synthesizing SACs. Therefore, researchers are dedicated to employing this approach for the production of axially coordinated SACs. Of course, in order to synthesize axially coordinated SACs and not just SACs, hydrothermal precursors must use materials that can perform the fifth coordination, such as FePc. Huang et al. [65] synthesized FePc/AP GA composites using a one-step hydrothermal method. In this process, both the loading of FePc and the formation of 3D graphene hydrogel were achieved (Fig. 3a). An aqueous solution of FePc in tetrahydrofuran and sodium ascorbate were added to the AP-GO dispersion, followed by reaction at 100 °C for 2 h in a high-pressure reactor. The molded graphene hydrogel was then extracted using tweezers and soaked in deionized water for two days to eliminate any residue or weakly adsorbed FePc. Finally, the hydrogel underwent freeze-drying to yield FePc/AP-GA. The functional groups present in the products were initially analyzed using Fourier transform infrared spectroscopy (FTIR). The results indicate that FePc molecules were anchored to the graphene surface via coordination interaction with the axial 4-aminopyridine (4-AP) linker. Although solvothermal synthesis of SACs is relatively common, the synthesis of SACs with axial coordination structure by this method is not yet widespread. Therefore, the development of efficient solvothermal method to precisely engineer axial ligands in SACs is highly desired.

2.3 Wet Chemical Synthesis

The wet chemical synthesis is a commonly employed method for synthesizing SACs, including those with axial coordination structures. This synthetic approach involves the thorough mixing of metal salts with appropriate supports, gradual adsorption of metal ions onto the surface or pore structure of the supports, and subsequent large-scale production of SACs through drying and reduction processes [66]. Different from the simple wet chemical synthesis of conventional SACs, in the synthetic processes of axially coordinated SACs, the metal precursors impregnated on the support basically contains M–N_4 configuration, or the supports themselves have the M–N_4 moiety, which is also a prerequisite for the formation of axial coordination configuration of SACs. For example, Zhao et al. [67] employed a facile wet-impregnation method to synthesize Pt-ACs/CoNC featuring axial Co–O–Pt bonding, in which the Pt atomic clusters were axially anchored onto Co–N–C single atom sites. Besides, Dai et al. [68] treated the $Ti_3C_2T_x$ MXene nanosheets in NaOH solution to generate alkaline $Ti_3C_2(OH)_x$ MXene (Alk MXene), which was then combined with FePc via ultrasonic mixing, producing an Alk-MXene/FePc hybrid catalyst featuring an Fe–N_4O_1–OC quasi configuration (Fig. 3b). To further elucidate the local coordination geometry and electronic states, XANES and EXAFS analyses were conducted. The Fe K-edge of Alk-MXene/FePc falls between FeO and Fe_2O_3, indicating the oxidation state of Fe is between + 2

https://doi.org/10.1007/s40820-023-01196-1

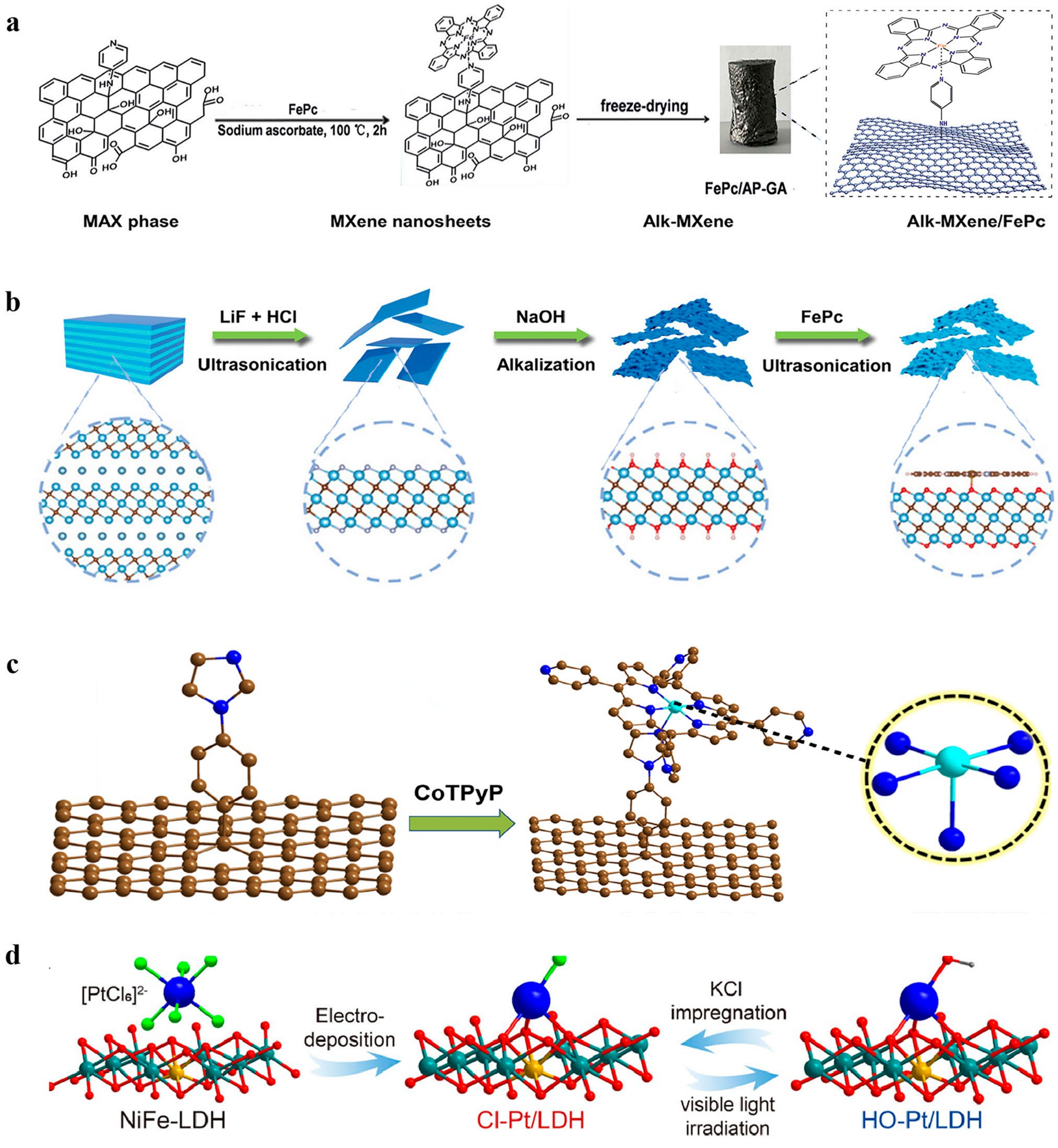

Fig. 3 **a** Fabrication process of the 3D FePc/AP-GA catalyst by solvothermal synthesis. Reproduced with permission [65]. Copyright: 2018. The Royal Society of Chemistry. **b** Schematic synthesis of Alk-MXene/FePc catalyst by wet chemical synthesis. Reproduced with permission [68]. Copyright: 2023, Wiley-VCH GmbH. **c** Schematic illustration of the synthesis of CoTPyP@Im-RGO by support functionalization method. Reproduced with permission [71]. Copyright: 2022, Elsevier Ltd. **d** Schematic illustration for the synthesis of Cl-Pt/LDH catalyst by electrodeposition method and the following reversible axial ligand exchanging procedures. Atoms are indicated by spheres: Pt (blue), Ni (olive), Fe (yellow), O (red), Cl (green), and H (gray). Reproduced with permission [77]. Copyright: 2022, Springer Nature. (Color figure online)

and + 3. The FT-EXAFS spectra of FePc and Alk-MXene/FePc exhibit main peaks at 1.41 and 1.50 Å in R-space, respectively. The increased height of the main peak confirms the presence of an axial Fe–O bond within the first coordination sphere. Furthermore, the WT-EXAFS contour maps reveal a maximum intensity of 7.6 $Å^{-1}$ for FePc and 6.9 $Å^{-1}$ for Alk-MXene/FePc, suggesting that axial coordination with Fe–O may alter the coordination environment of the Fe center. Moreover, Guo et al. [69] employed the same method to synthesize Fe-SACs with axial O coordination. The FePc perchlorate ($FePc·ClO_4$) was rapidly added to the GO aqueous dispersion system in acetonitrile, followed by a reduction using $NaBH_4$ and hydrazine hydrate to obtain the FePc/RGO catalysts. X-ray photoelectron spectroscopy (XPS) revealed a decrease in the binding energy of N atoms within Fe–N (N_2, pyrrol-N) bonds and a consequent change in the coordination number of Fe atoms from 4 to 5 when compared with FePc. The Fe K-edge XANES analysis provided further insights into the structural characteristics of FePc/RGO SAC, indicating that FePc is axially coordinated to RGO via an O bridge.

2.4 Support Functionalization Method

Support functionalization techniques are predominantly employed to tether metal phthalocyanine or porphyrin onto CNTs or graphene via intermediates such as pyridine, which simplifies the synthesis of the classical axial coordination structure of such SACs [70]. For example, Yang et al. [71] used this method to anchor a Co porphyrin molecule, CoTPyP, onto functionalized reduced GO (Im@RGO) and provided an axial ligand to the cobalt center (Fig. 3c). The synthesis involved diazotization of 4-imidazole-1-yl-aniline to reduce GO and form Im@RGO, followed by co-refluxing of CoTPyP and Im@RGO in N, N-dimethylformamide (DMF) under an N_2 atmosphere to yield CoTPyP@Im-RGO. The electronic structure and coordination environment of CoTPyP@Im-RGO were investigated using XANES and EXAFS techniques, revealing that Co is present as a single atom with a positive charge, and the average valence state of Co ranges from + 2 to + 3. The Co active center forms both a planar Co–N_4 structure by bonding with N atoms from porphyrin and axial coordination with N on carbon support to create a Co–N_5 structure. This method has also been employed in other studies for the synthesis of metal phthalocyanines with axial coordination structure. Riquelme et al. [72] synthesized CoPc-Py-CNT catalysts using this method. They functionalized CNTs with pyridine (Py) through diazotization reaction to yield Py-CNT, followed by the introduction of CoPc onto the surface of Py-CNT by refluxing in N_2 at 150 °C in DMF to yield CoPc-Py-CNT. The synthesized catalyst possesses a Co–N_5 structure, with four N atoms forming a planar arrangement with Co and one N atom coordinating axially with Co. Later, Fan et al. [73] also synthesized CoPc-Py-CNT catalysts with axial N coordination using the same method. After grafting pyridine onto CNTs (CNT-Py), a mixture of CNT-Py and CoPc was refluxed in tetrahydrofuran (THF) for 1 h under Ar protection, thus giving rise to N-axially coordinated Co-SACs.

2.5 Electrodeposition Method

Electrodeposition for axial coordination design of SACs is a recently developed method that involves the dissolution of bulk metal into a solution, resulting in the formation of atomic metal species that are subsequently anchored onto a support using electrochemical means [74]. During the synthesis of SACs, metal ions are transformed into metal atoms by electrodeposition and deposited as SACs onto the supports on the working electrode [75]. In contrast, in the synthesis of axially coordinated SACs, metal coordination ions transform to metal atoms while serving as an axial ligand to the SACs that already formed on the support [76]. Moreover, the metal ligand can also be replaced into a series of other ligands by certain methods. Zhang et al. [77] employed NiFe-LDH nanosheet arrays as the support, and used the electrodeposition method to synthesize the Cl–Pt/LDH catalyst (Fig. 3d). The Cl–Pt/LDH was prepared in 1 M KOH solution containing $PtCl_6^{2-}$ anions using a three-electrode system, with NiFe-LDH serving as the working electrode. During the process of electrolysis, $PtCl_6^{2-}$ anions were electrodeposited and adsorbed onto the surface of LDH to generate atomically dispersed Pt sites with axial Cl coordination. Notably, the axial ligand can be altered by a further photochemical method. Upon visible light irradiation in water, the axial Cl ligand was replaced by a hydroxide group. Noteworthily, the exchanged hydroxyl group can be reversibly switched back to the axial Cl ligand after a KCl impregnation treatment. Currently, the development of electrochemical methods for constructing axially coordinated

https://doi.org/10.1007/s40820-023-01196-1

SACs is still very limited. However, electrodeposition offers a promising avenue for the synthesis of SACs with axial coordination.

3 Axial Coordination Design of SACs in Energy Electrocatalysis Applications

Due to their cost effectiveness, maximized atom utilization efficiency and highly tunable properties, the use of transition metal SACs in electrocatalysis has become a prominent research [78]. The intrinsic activity and density of metal active sites are key factors that influence the catalytic ability of SACs [79]. Consequently, various SACs featuring diverse active sites and matrices have been designed and studied. It is widely accepted that M–N–C (M = Fe, Co, Ni, Mn, Cu, etc.) structures primarily serve as active sites for SACs [80], and precisely manipulating the environmental structure surrounding metal atoms can significantly improve the electrochemical performance of catalysts [81]. In a bid to further enhance the activity of SACs, several strategies have been investigated and implemented [82, 83]. One such strategy involves changing the coordination number of central transition metal atoms from four to five or six by adding axial coordination ligands, which alters the coordination environment and electronic structure of the central atom and allows for the regulation of electrocatalytic performance of SACs. To date, reported axial coordination designs of SACs used in electrocatalytic reactions can be categorized into five categories based on the axial ligands used: (1) nitrogen-containing ligands, (2) oxygen-containing ligands, (3) sulfur-containing ligands, (4) halogen-containing ligands, and (5) other ligands. In the following section, we focus on discussion of the electrocatalytic performance of SACs coordinated with the above axial ligands in various energy-related electrochemical reactions.

3.1 Oxygen Reduction Reaction

The oxygen reduction reaction (ORR) is an important and extensively studied electrochemical reaction [84]. It is a multistep process and generally involves two distinct reaction pathways, depending on the number of electron transferred [85]. Specifically, O_2 molecules can be reduced to either H_2O through a four-electron ($4e^-$) reaction pathway (Eqs. (1) and (2)) or to H_2O_2 through a two-electron ($2e^-$) reaction pathway (Eqs. (3) and (4)) [86].

$4e^-$ processes:

In acidic medium (pH = 0):

$$O_2 + 4H^+ + 4e^- \rightarrow 2H_2O, E^\circ = 1.23\ \text{V}\ \ \text{vs. SHE} \tag{1}$$

In alkaline medium (pH = 14):

$$O_2 + 2H_2O + 4e^- \rightarrow 4OH^-, E^\circ = 0.40\ \text{V}\ \ \text{vs. SHE} \tag{2}$$

$2e^-$ processes:

In acidic medium (pH = 0):

$$O_2 + 2H^+ + 2e^- \rightarrow H_2O_2, E^\circ = 0.06\ \text{V vs. SHE} \tag{3}$$

In alkaline medium (pH = 14):

$$O_2 + 2H_2O + 2e^- \rightarrow H_2O_2 + 2OH^-, E^\circ = 0.70\ \text{V}\ \ \text{vs. SHE} \tag{4}$$

The $4e^-$ reaction pathway in electrochemical ORR is composed of two distinct mechanisms (Eqs. (5) and (6)). The $2e^-$ reaction pathway includes only one *OOH reaction intermediate (Eqs. (7)). The ORR reaction mechanism is illustrated below [87]:

$4e^-$ processes:

$$O_2 + 4\left(H^+ + e^-\right) \rightarrow * \text{OOH} + 3\left(H^+ + e^-\right) \rightarrow * \text{O} + 2\left(H^+ + e^-\right) \rightarrow * \text{OH} + 1\left(H^+ + e^-\right) \rightarrow H_2O \tag{5}$$

$$O_2 + 4\left(H^+ + e^-\right) \rightarrow 2 * \text{OH} + 2\left(H^+ + e^-\right) \rightarrow H_2O \tag{6}$$

$2e^-$ processes:

$$O_2 + 2\left(H^+ + e^-\right) \rightarrow * \text{OOH} + 1\left(H^+ + e^-\right) \rightarrow H_2O_2 \tag{7}$$

Both $4e^-$ ORR and $2e^-$ ORR processes have significant importance in scenes of daily life and industrial chemicals synthesis. The $4e^-$ transfer process in the cathodic ORR reaction is specifically desirable for proton-exchange membrane fuel cells (PEMFCs) and metal-air batteries [85]. However, due to the sluggish reaction kinetics of ORR, even the most efficient Pt-based catalysts require a high Pt loading to attain an optimal fuel cell performance [88]. As a consequence, extensive research has been carried out to develop cost-effective and available electrocatalysts for PEMFCs, encompassing advanced Pt alloys, heteroatom-doped nanocarbons, SACs and so on [89]. SACs are a kind of important electrocatalysts to remarkably improve the performance of ORR, and various strategies have been developed to regulate the active site structures of SACs [90, 91]. For instance, Yuan et al. [92] reported a Co-SAC featuring abundant carbon defects, which can significantly decrease the adsorption free energy of *OOH on Co–N_4 sites, thereby enhancing the ORR catalytic performance. Zhang et al. [93] prepared an S-doped FeN_3S active site and evaluated its electrochemical ORR performance. Their findings revealed that the FeN_3S SAC exhibited exceptional ORR performance after S doping, potentially due to the optimized charge and spin distribution in Fe–N–C materials.

Additionally, another significant application of ORR is the generation of H_2O_2 through the $2e^-$ pathway. As one of the most crucial chemicals, H_2O_2 has a vast array of industrial applications, such as chemical synthesis [94], pulp and paper bleaching [95], wastewater treatment [96], and others. The current industrial method for producing H_2O_2 is primarily the anthraquinone oxidation process, which suffers from drawbacks such as high energy consumption, complex infrastructure, and significant waste generation [97]. In recent years, the electrochemical synthesis of H_2O_2 from ORR through $2e^-$ transfer process has been extensively investigated due to its advantages of mild reaction conditions and pollution-free waste [98]. The utilization of SACs also confers significant benefits in facilitating $2e^-$ ORR. In principle, to achieve highly selective synthesis of H_2O_2 via $2e^-$ ORR, it is essential to avoid O–O bond cleavage. Due to the unique structure of SACs, where metal centers are atomically dispersed, O_2 adsorption on SACs typically follows Pauling-type coordination rather than side-on coordination, which reduces the feasibility of O–O bond breaking [99]. Therefore, SACs are promising candidates for H_2O_2 synthesis via $2e^-$ ORR.

Axial coordination has emerged as an effective means of regulating the structure of SACs, holding great promise in modulating their performance in ORR. To date, SACs modified with various axial ligands including N-containing, O-containing, S-containing, halogen-containing ligands and other ligands have been investigated for their ability to regulate the ORR properties. Table 1 summarizes the recent axial coordination designs of SACs for ORR.

3.1.1 Nitrogen (N) Ligand Axially Coordinated SACs for ORR

Since the mid-1960s [100], metal macrocyclic compounds such as metal phthalocyanine have been extensively investigated in the field of electrocatalysis. Because their well-defined M–N_4 configuration could serve as an excellent model for investigating the ORR mechanism and regulating the catalytic activity of SACs [101]. However, metal macrocyclic compounds lack long-term stability [102], making them inadequate for practical electrocatalytic applications. To address this challenge, researchers have explored various approaches, such as modifying the chemical structure and incorporating functional groups, atoms, or various substrates, to modulate the catalytic activity of metal macrocycles [103].

Graphene [104], carbon nanotubes (CNTs) [105, 106], and carbon nanofibers [107] are known to exhibit excellent catalytic activity for ORR. Recently, electrocatalysts comprising of metal phthalocyanine with pyridine or imidazole fixed on carbon nano-materials have gained increasing attention due to their low ORR overpotential [108]. The axial coordination of electron-donating ligands onto metal phthalocyanine facilitates the adsorption of O_2 molecules and switches the formation of *OOH intermediates to be the rate-limiting step. In addition, the re-hybridization of Fe 3d-orbitals with axially coordinated ligand orbitals leads to significant alterations to both electronic and geometric structures, thereby greatly enhancing the rate of ORR. Zhang et al. [109] have demonstrated that the electrochemical ORR performance of functionalized multi-walled CNTs (CNT-R, R = NH_2, COOH, or OH) can be enhanced by loading iron phthalocyanine molecules onto them (FePc/CNT-R) through the axial coordination of functional groups to the Fe center atoms in iron phthalocyanine molecules (Fig. 4a). The FePc/CNT-NH_2 with NH_2 axial coordination exhibited an $E_{1/2}$ of 0.92 V and remarkable electrocatalytic activity towards ORR (Fig. 4b). Cao et al. [110] reported a novel FePc-Py-CNTs electrocatalyst through covalent functionalization of single-walled CNTs with FePc. In this catalyst, pyridine was modified on CNT and coordinated to the Fe atom in FePc, forming a unique N-axial coordination structure (Fig. 4c). This structure exhibited superior electrocatalytic activity for ORR, with an $E_{1/2}$ of 0.915 V compared to the benchmark Pt/C catalyst ($E_{1/2}$ = 0.88 V), and demonstrated robust durability when cycled in an alkaline medium. To elucidate the origin of enhanced catalytic activity and excellent durability of FePc-Py-CNTs catalyst, researchers employed spin polarization DFT to calculate both FePc models with and without axial coordination. It was found that in comparison with

Table 1 Summarized electrocatalytic ORR activity of typical axial coordination modified SACs

Axial-coordinated SACs	Coordination structure	Axial atom	Electrolyte	Pathway	$E_{1/2}$ (V vs RHE)	H_2O_2 yield (%)	Refs
FePc/CNT-R	FeN_4–NH_2	N	0.1 M KOH	$4e^-$	0.92	< 3	[109]
FePc–Py–CNTs	FeN_4–Py	N	0.1 M KOH	$4e^-$	0.915	< 1.5	[110]
FePc/NGM-0.25	FeN4–N	N	0.1 M KOH	$4e^-$	0.90	< 1.25	[111]
Fe-SAC/N–C	FeN_4–N	N	0.1 M KOH	$4e^-$	0.89	< 1	[115]
Fe–N–C/rGO	FeN_4–N	N	0.1 M KOH	$4e^-$	0.90	< 5	[116]
Mn–NC-SA-950	MnN_4–N	N	0.1 M KOH	$4e^-$	0.852	< 5	[117]
Fe@Fe/N-G-800	FeN_4–O	O	0.1 M KOH	$4e^-$	0.866	< 3	[62]
O–Zr–N–C	ZrN_4–O	O	0.1 M KOH	$4e^-$	0.91	< 8	[120]
Co-SA@N-CNFs	CoN_4–O	O	0.1 M KOH	$4e^-$	0.85	< 20	[121]
V–N_1O_4	V–O_3N_1–O	O	0.1 M KOH	$4e^-$	0.865	< 10	[122]
o-MQFe	FeN_3O–O–Ti	O	0.1 M KOH	$4e^-$	0.861	< 5	[123]
FeAB–O	FeN_4–O	O	0.1 M KOH	$4e^-$	0.90	< 1	[124]
$N_4Ni_1O_2$/OCNTs	NiN_4–2O	O	1.0 M KOH	$2e^-$	0.68	> 90	[126]
Fe–N/S–C	Fe–N_3S_1OH	O	0.1 M KOH	$4e^-$	0.882	< 3.2	[127]
Fe (Zn)–N–C	HO–FeN_4–O–FeN_4–OH	O	0.1 M $HClO_4$	$4e^-$	0.83	< 7	[128]
S1–Cr1N4–C	Cr_1N_4–S	S	0.1 M KOH	$4e^-$	0.90	< 12	[129]
S-modified Fe–N–C	FeN_4–S	S	0.1 M KOH	$4e^-$	0.88	< 7	[130]
Co–ZIFs-60	CoN_4–S	S	0.5 M H_2SO_4	$4e^-$	0.793	< 2.2	[131]
FeN_4Cl_1/NC	FeN_4–Cl	Cl	0.1 M KOH	$4e^-$	0.91	< 4	[64]
Fe–N/C-SAC	FeN_4–Cl	Cl	0.1 M KOH	$4e^-$	0.91	< 6	[132]
$FeCl_1N_4$/CNS	FeN_4–Cl	Cl	0.1 M KOH	$4e^-$	0.921	< 1	[133]
Fe^{Zn}/CNP (1)	FeN_4–Cl	Cl	0.1 M KOH	$4e^-$	0.88	< 10	[134]
FeN_4Cl SAC	FeN_4–Cl	Cl	0.1 M HClO4	$4e^-$	0.818	< 1	[135]
YN_4–Cl catalyst	YN_4-Cl	Cl	0.1 M KOH	$4e^-$	0.85	–	[137]
FePc–RCNTs	FeN_4–C	C	0.1 M KOH	$4e^-$	0.86	< 2	[139]
FeNPC	FeN_4–PO_4	P	0.1 M KOH	$4e^-$	0.88	< 5.6	[144]
Pt_1@Fe–N–C	FeN_4–PtO_2	PtO_2	0.5 M H_2SO_4	$4e^-$	0.80	< 2	[145]
FeN_4–Te_n	FeN_4–Te_n	Te	0.1 M KOH	$4e^-$	0.867	–	[146]

the FePc-CNT system, the FePc-Py-CNT system exhibits a higher degree of O–O bond stretching, facilitating easier dissociation of O_2 molecules. The binding energies of O_2 and *OOH on FePc-Py-CNT are slightly higher than those of FePc-CNT, indicating a more favorable adsorption process on active sites in FePc-Py-CNT and hence superior electrocatalytic ORR performance. Moreover, Xia et al. [111] immobilized FePc onto N-doped graphene nanonets (NGMs), where the axial interaction between the Fe–N_4 moiety of FePc and the N in the NGM graphene matrix generates an Fe–N_5 structure exhibiting exceptional catalytic activity for ORR.

In addition to FePc, CoPc is also widely studied to be anchored on CNTs for ORR via the axial coordination with the functional groups on CNTs. Vier et al. [112] synthesized three distinct Co catalysts, namely CoPc, perfluoro CoPc (16(F)CoPc), and cobalt octaethylhexyl phthalocyanine (8(2-Et-$C_6H_{11}O$)CoPc), which were anchored on the pyridine (Py)-modified CNT. In these Co catalysts, the Co atom is coordinated with five N atoms, with an axial N from the Py. The electron paramagnetic resonance (EPR) and XPS spectra revealed that the signals of CNTs modified with various CoPcs exhibited distinct differences. Specifically, 8(2-Et-$C_6H_{11}O$) CoPcPy-CNT features a high-spin ($S=3/2$) Co(II) species at its metal center, while both CoPc-Py-CNT and 16(F)CoPcPy-CNT comprise of low-spin configuration ($S=1/2$) Co(II) species and intermediate spin ($S=1$) Co(III) species, respectively. Further studies indicated that the pyridine ligand in 8(2-Et-$C_6H_{11}O$) CoPcPy-CNT and CoPc-Py-CNT functions as an electron-withdrawing group, while that in 16(F)CoPc-Py-CNT acts as an electron-donating group. This is attributed

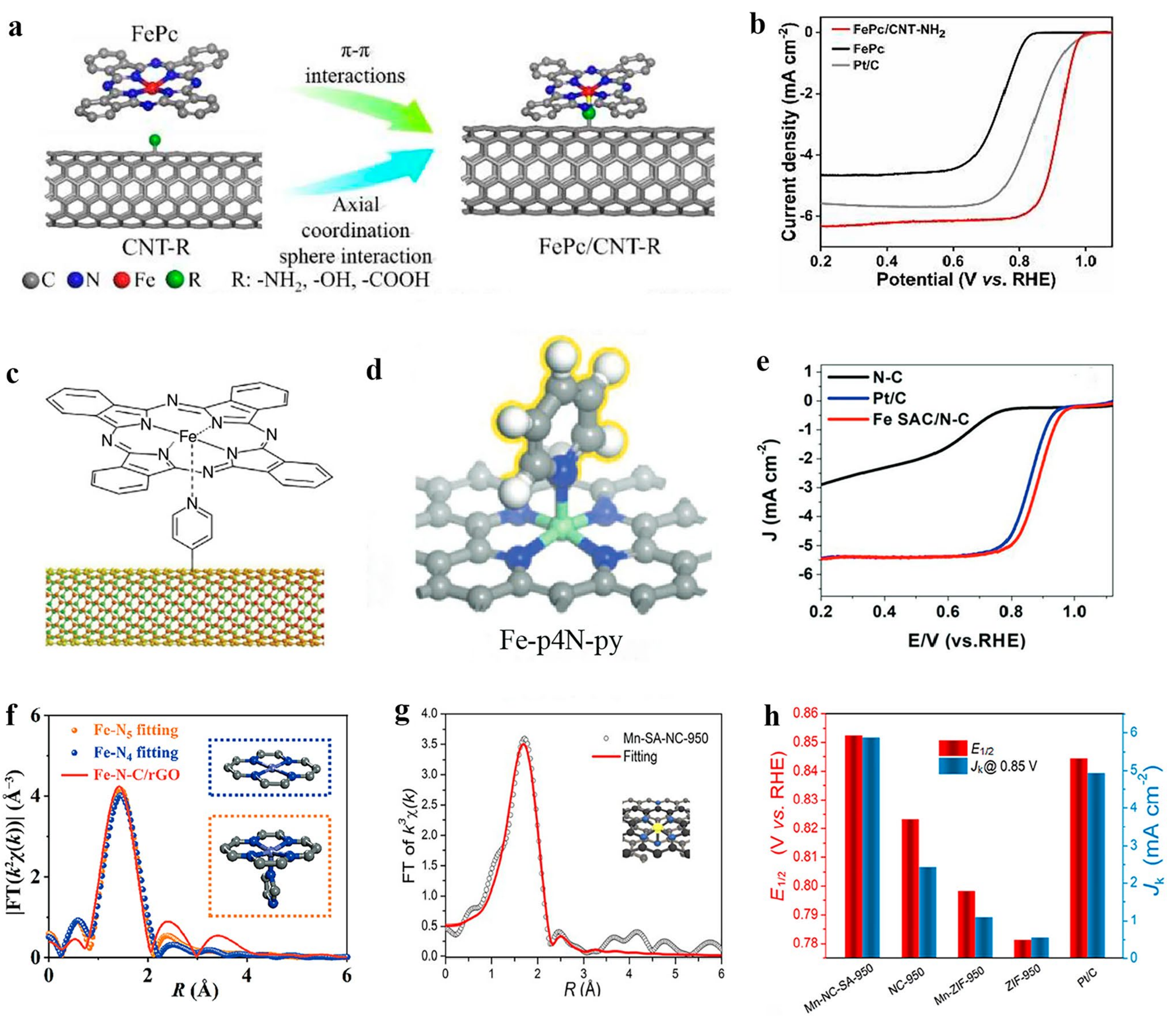

Fig. 4 **a** Schematic representation of the self-assembly process of the FePc/CNT–R catalyst. **b** LSV curves of FePc, FePc/CNT–NH_2, and Pt/C in O_2-saturated 0.1 M KOH. Reproduced with permission [109]. Copyright: 2021 Wiley-VCH GmbH. c Schematic diagram of the structure of FePc–Py–CNTs composite. Reproduced with permission [110]. Copyright: 2013, Nature Publishing Group. **d** Top view of Fe-SACs models with Fe–p4N–py coordination configuration. **e** LSV curves of Fe-SAC/N–C, N–C, and commercial Pt/C in O_2-saturated 0.1 M KOH with a sweep rate of 10 mV s^{-1} and a rotating rate of 1600 rpm. Reproduced with permission [115]. Copyright: 2019 WILEY-VCH Verlag GmbH & Co. KGaA, Weinheim. **f** R space fitting curve of Fe–N_4 configuration (marked by blue dotted frame) and Fe–N_5 configuration (marked by orange dotted frame, here hydrogen atoms on the imidazole ring are hidden to make the structure more visible). Reproduced with permission [116]. Copyright: 2022 Springer Nature. **g** Mn K-edge EXAFS fitting curve at R space of Mn-NC-SA-950. **h** $E_{1/2}$ and J_k at 0.85 V of the prepared catalysts and Pt/C catalyst in O2-saturated 0.1 M KOH solution at a scan rate of 10 mV s^{-1}. Reproduced with permission [117]. Copyright: 2023, ELSEVIER B.V. and Science Press

to the pull–push electronic effect induced by F residues within the coordinated Co–N_4 atomic plane. But the impact of axial coordination surpasses that of the same-plane residues attached to the molecule. Therefore, the three complexes investigated in this study demonstrated comparable ORR activity, with a total electron transfer number of approximately 3.2 and a Tafel slope of around –50 mV dec^{-1}.

Besides the N-containing functional groups or molecules on carbon-based substrates, other types of N-containing axial ligands have also been investigated to modify the structures and properties of metal phthalocyanines. Pizarro et al. [56] constructed four self-assembled catalysts with different configurations by binding pyridine salt molecules to FePc and then anchoring them on the surface of Au (111) electrodes. They investigated the effects of axial coordination of two pyridine isomers (Up and Down) with FePc and 16(Cl) FePc on the ORR properties of catalysts. DFT calculations showed that pyridine molecular wire, as an axial ligand, can decrease the electron density of the active site and alter Fe–O_2 binding. Therefore, pyridine molecules play a crucial role in regulating and enhancing the activity of FePc towards ORR. After conducting electrochemical tests to study the ORR properties of various catalyst configurations, it was discovered that among all self-assembled catalysts tested, the Au (111)/Up/FePc system exhibited the highest level of catalytic activity.

DFT calculations also predict that the Fe–N_5–C SACs with axial N coordination could exhibit superior electrocatalytic ORR activity compared to the typical Fe–N_4–C SACs [113]. In addition to the Fe–N_5 active sites engineered on FePc, other Fe–N_5 SACs with axial N ligand have also been achieved, and demonstrate high electrocatalytic ORR activity. Liu et al. [114] successfully synthesized an Fe–N_5/C@G SAC with an Fe–N_5 active site on the surface of single-layer graphene utilizing FePc powder as a precursor. In the ORR process, an efficient 4e^- transfer process occurred on the Fe–N_5/C@G catalyst. Lin et al. [115] have successfully synthesized Fe-SAC/N–C catalysts featuring axial N-coordination in Fe–N_5 structure which exhibits excellent ORR activity ($E_{1/2} = 0.89$ V) and improved stability (Fig. 4d). Through DFT calculations, the ORR mechanisms of three SAC catalyst models (Fe–4pN, Fe–4pN–OH, and Fe–4pN–py) were studied and compared (Fig. 4e). It was discovered that axially coordinated pyridine can effectively regulate the interaction strength between Fe atoms and O-containing intermediates, thereby enhancing ORR activity. Li et al. [116] synthesized Fe–N–C/rGO-SAC, which features distinctive penta-coordinated Fe centers bound to five N atoms (Fig. 4f). The single Fe site is stabilized by four equatorial and one axial N atoms provided by a N-doped carbon matrix and an imidazole ring, respectively. This results in the formation of an asymmetric electron depletion region at the metal center, improving the electrocatalytic activity of ORR. It has also been reported that precise adjustment of the coordination number of Mn single atoms can significantly enhance ORR activity. Qin et al. [117] successfully synthesized atomically dispersed Mn–N_5 catalyst, which exhibited lower energy barrier and higher O_2 adsorption performance compared to traditional unit point Mn–N_4 catalyst and Pt/C due to its uneven distribution of electronic charges. This accelerates ORR kinetics and results in a significant increase in catalyst activity.

3.1.2 Oxygen (O) Ligand Axially Coordinated SACs for ORR

Oxygen (O)-containing ligands (such as O, OH, etc.) are also an important class of axial coordination groups in modifying the M–N–C configuration. The electronic structure can be tuned by axial O-containing ligands, which in turn adjust the binding energy between intermediates and active sites. This adjustment effectively enhances the catalytic activity of a single metal atom. In recent years, studies on SACs with axial coordination of O-containing ligands have been developed, and various atomic configurations have been documented [118].

The exploration of functional substrates and precise control over the electronic structure of atomic metal active species with a medium spin state holds great significance [119]. According to the transition metal *d-band* center theory, the performance of the catalyst is governed by the electronic structure of its catalytic center, which in turn determines the adsorption kinetics of intermediates. Wang et al. [120] reported Zr single atom site with a five-coordination configuration including an axial O ligand (denoted as O–Zr–N–C). The structure of O–Zr–N–C and its synthetic process are shown in Fig. 5a, b. The presence of the O axial ligand results in a lowered *d-band* center of Zr, which contributes to the stable local structure and appropriate adsorption capacity for intermediates. As a result, the ORR performance of O–Zr–N–C is significantly better than that of commercial Pt/C, with an $E_{1/2}$ of 0.91 V and excellent durability, as demonstrated by a current retention rate of 92% after 130 h. Similarly, Zhang et al. [121] also synthesized Co-SAC with axial O coordination (Co-SA@N-CNFs). The local coordination configuration of single Co atom was proposed as a Co–N_4O portion with an O atom in the axial direction perpendicular to the Co–N_4 plane. Such axial coordination design contributed to excellent ORR activity. Compared to Pt/C (62 mV dec^{-1}), the Co-SA@N-CNFs showed impressively

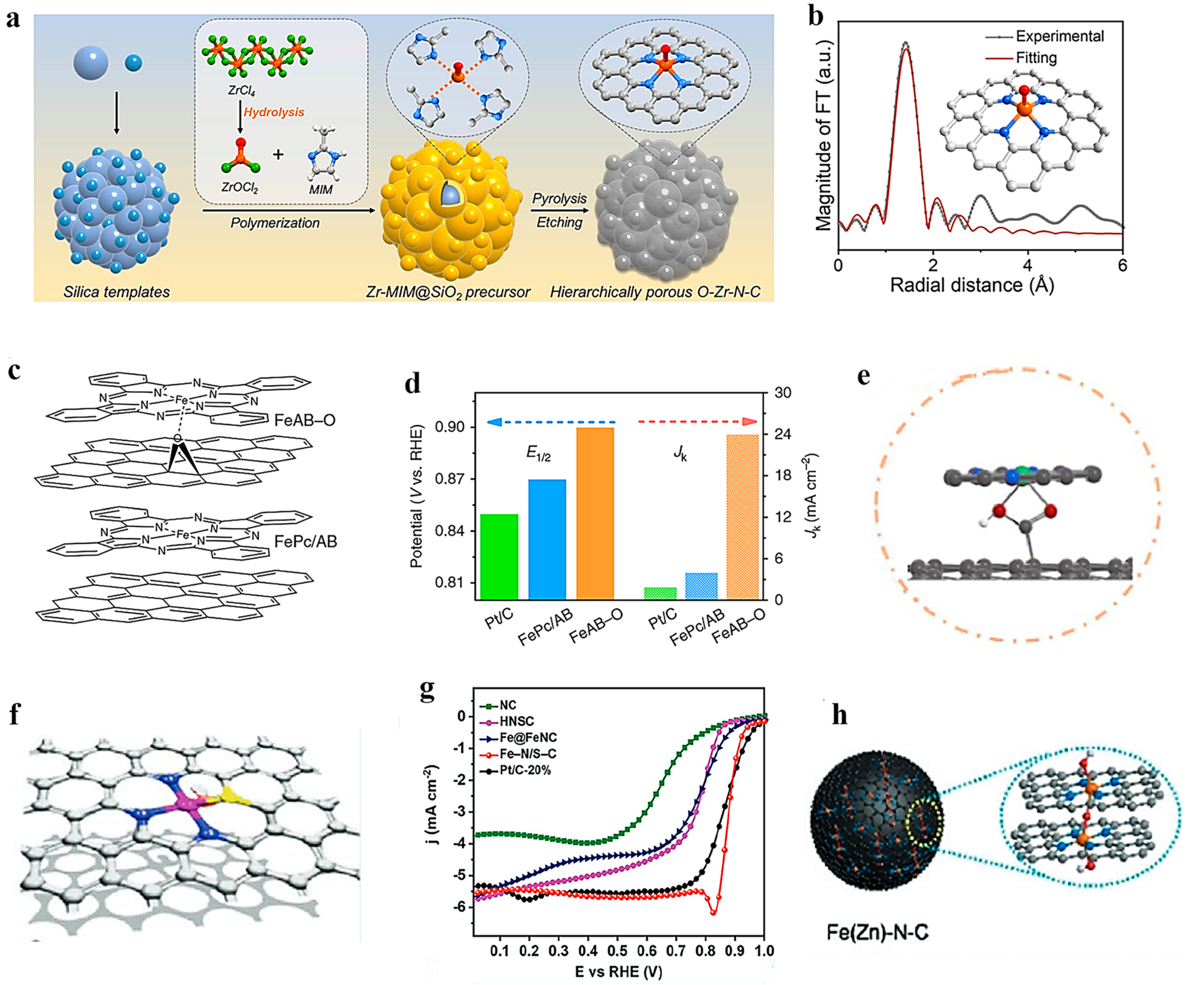

Fig. 5 **a** Schematic diagram illustrating the synthetic route of O–Zr–N–C. **b** R space curve-fitting of O–Zr–N–C. Inset depicts the fitted structure of Zr site in O–Zr–N–C, the spheres in grey, blue, orange, and red represent C, N, Zr, and O atoms, respectively. Reproduced with permission [120]. Copyright: 2022 Wiley-VCH GmbH. **c** Molecular structure models of FeAB–O and FePc/AB. **d** $E_{1/2}$ and J_k values at 0.88 V for FeAB-O, FePc/AB, and Pt/C. Reproduced with permission [124]. Copyright: 2020, Springer Nature. **e** Structural model of $N_4Ni_1O_2$. Reproduced with permission [126]. Copyright: 2022 Wiley-VCH GmbH. f Structural model of Fe–N/S–C. g LSV polarization curves of NC, HNSC, Fe@FeNC, Fe–N/S–C and Pt/C at 1600 rpm in 0.1 M KOH aqueous solution. Reproduced with permission [127]. Copyright: 2021 Wiley-VCH GmbH. h The structural model of Fe(Zn)–N–C catalyst. Reproduced with permission [128]. Copyright: 2020 Wiley-VCH Verlag GmbH & Co. KGaA, Weinheim

low Tafel slope of 50 mV dec^{-1}, highlighting its exceptional ORR kinetics.

In addition to the commonly reported plane-symmetric M–N_4 configuration with axially coordinated O atoms, the asymmetric coordination structure of the central metal single atoms at the plane can also be further modified with additional axial O coordination. For example, the valence state of V element is variable, and its electronic structure can be modulated by an appropriate coordination structure. Cheng et al. [122] constructed a unique V–N_1O_4 co-coordinated with N and O embedded in a carbon matrix utilizing glycine as a chelating agent. In this compound, V is coordinated with one N and three O atoms to form a planar structure, while the other O atom is located axially at the center of the V atom. The V-SACs exhibited an $E_{1/2}$ of 0.865 V in alkaline solution and demonstrated favorable performance even under acidic conditions. Likewise, Liu et al. [123] proposed an axial Fe–O–Ti ligand-regulated spin state transition strategy to enhance the performance of ORR. An axial Fe–O–Ti bridge bond was initially established in FeN_4–O–Ti and FeN_3O–O–Ti models, and the DFT calculations were conducted. The differential charge distribution of FeN_3O–O–Ti is wider than that of FeN_4–O–Ti, indicating a larger area of electrons participation in the electronic transition of FeN_3O–O–Ti. As a result, the magnetic moment of Fe increases from 1.51 μ_B (FeN_3O) to 3.52 μ_B (FeN_3O–O–Ti), which facilitates favorable e–g filling and enhances the low-to-medium spin transition of Fe with increased O_2 affinity. Moreover, compared to other configurations, FeN_3O–O–Ti exhibited superior O_2 adsorption energy ($\Delta E_{ads}(O_2)$, 1.84 eV) and integrated-crystal orbital Hamilton population (ICOHP) value (1.88 eV), resulting in its optimal binding strength with O_2. It concludes that FeN_3O–O–Ti could possess exceptional ORR activity. Based on this conclusion, a novel FeN_3O–O–Ti catalyst named o-MQFe was synthesized and subjected to electrochemical performance testing. Consistent with the DFT calculation results, the synthesized catalyst demonstrated exceptional ORR activity, as evidenced by $E_{1/2}$ and E_{onset} values of 0.861 and 0.96 V, respectively.

Axial O ligands are also used to modify the ORR properties of FePc. Chen et al. [124] proposed an electron localization strategy through axial Fe–O coordination to enhance O_2 adsorption, and ultimately leads to high ORR performance. They designed a catalyst (FeAB–O) by coordinating FePc molecules with O-functionalized groups on the acetylene black (AB–O) treated by O_2 plasma (Fig. 5c). The material exhibited exceptional ORR performance, with a remarkable $E_{1/2}$ of 0.90 V and a calculated kinetic current density (J_k) of 24.0 mA cm^{-2} at 0.88 V, surpassing FePc/AB ($E_{1/2}=0.87$ V, $J_k=1.9$ mA cm^{-2} at 0.88 V) and Pt/C ($E_{1/2}=0.85$ V, $J_k=4.0$ mA cm^{-2} at 0.88 V) (Fig. 5d). Xu et al. [62] reported a Fe@Fe/N-G-800 SAC material, which was designed and synthesized by bonding FePc molecules to graphene-like Fe–N–C materials with axial O–FeN_4 coordination sites. The central Fe atom in FePc can coordinate with the O atom in O–FeN_4 site from Fe/N-G-800, thus forming a unique Fe–O–Fe structure. The formation of Fe–O–Fe bridge bonds between Fe–N_4 sites effectively reduced ORR overpotential. While axial coordination between metal atoms and O atoms has significantly increased the ORR electrocatalytic activity of most SACs, it cannot be simply concluded that such coordination inevitably leads to improved electrocatalytic ORR activity. Cao et al. [125] prepared Co-SACs by coordinating CoPc with O atoms from different positions in the carbon plane and evaluated their electrochemical ORR performance. They found that the ORR electrocatalytic performance of the catalyst could be significantly enhanced only when the axial O was located on the carbon defect sites.

In addition to a single axial O atom ligand, some other types of axial O ligands have also been investigated and documented, including those with two O atoms or OH groups. Xiao et al. [126] synthesized Ni-SAC with Ni atom coordinated by four planar N atoms and two axial O atoms (N_4–Ni–O_2) loaded on carboxyl functionalized MCNTs, as illustrated in Fig. 5e. In contrast to the other type Ni-SACs synthesized, the N_4–Ni–O_2 SAC exhibited a greater propensity towards 2e$^-$ ORR, with a H_2O_2 Faradaic efficiency (FE) of about 96% at a current density of 200 mA cm^{-2}, surpassing other reported SACs. This research is one of the few that aim to enhance the performance of 2e$^-$ ORR through axial O ligand modification of SACs. Similarly, Xiao et al. [59] employed the zeolite imidazolium framework (ZIF-8) as a self-template to synthesize Fe-SACs with uniform dispersion, in which each Fe atom coordinates with four N atoms in the plane and two O atoms in the axial direction. The optimized Fe–N–C catalyst demonstrates outstanding ORR activity in both acidic and alkaline solutions, with $E_{1/2}$ of 0.81 and 0.90 V, respectively. This multiple axial coordination design offers a new strategy for further optimizing SACs for various reactions. Li et al. [127] prepared Fe–N/S–C catalysts with axial OH coordination by embedding an asymmetric N–S coordinated Fe single atom into N–S co-doped porous carbon nanospheres (Fig. 5f). The quantitative structural parameters of Fe in Fe–N/S–C were obtained by EXAFS fitting, which revealed that the coordination numbers for the Fe–N, Fe–S, and Fe–O bonds were 2.8, 1.2, and 1.0, respectively, forming an Fe–N_3S_1–OH structure. The prepared catalyst exhibited exceptional electrocatalytic activity for ORR ascribing from its high specific surface area, open-layered porous structure, and excellent conductivity. Among all tested samples, Fe–N/S–C showed the highest E_{onest} of 0.970 V and $E_{1/2}$ of 0.882 V. Additionally, this catalyst demonstrated remarkable methanol resistance and durability (Fig. 5g). Gong et al. [128] proposed a novel selective manipulation strategy aimed at introducing axial O to the Fe site, which led to the successful preparation of Fe(Zn)–N–C catalysts. Interestingly, in this catalyst, O and OH are co-axially coordinated at the central site of the single atom of Fe. The O modification is stabilized by forming an axial Fe–O–Fe bridge bond, while the remaining axial coordination positions at the two FeN_4 sites are connected to OH groups (Fig. 5h). The resulting modulation of energy levels confers these sites with intrinsic activity more than 10 times higher than that of ordinary FeN_4 sites, thereby enabling the development of ORR electrocatalysts with significantly enhanced activity.

3.1.3 Sulfur (S) Ligand Axially Coordinated SACs for ORR

In recent years, researchers have successively reported $M–N_4$ SACs with different metal atomic centers that coordinate axially with S ligands. The studies have confirmed that axial S-ligands can disrupt the electronic localization around the planar $M–N_4$ active center, thereby promoting the rate-limited reduction release of *OH and accelerating the entire ORR process. Using the synthetic route shown in Fig. 6a, Guo et al. [129] have successfully created an atomically dispersed Cr catalyst featuring a five-coordinated active site ($S_1–Cr_1N_4–C$). Through various characterization methods, including an EXAFS study, it was determined that $S_1–Cr_1N_4$ comprises of four Cr–N bonds, each with a length of 1.34 Å, and one Cr–S bond with a length of 2 Å. It was thus inferred that the configuration of single Cr atom site is most likely an axially S-coordinated Cr_1N_4 configuration (Fig. 6b). The resulting $S_1–Cr_1N_4–C$ catalyst exhibited significantly improved ORR activity, enhanced methanol tolerance, and superior stability. In similar research, Li et al. [130] synthesized a controllable local coordination environment for an S-modified Fe–N–C catalyst, where the Fe atom was coordinated with four in-plane N atoms and one external axial S atom (as depicted in Fig. 6c). DFT calculations indicated that the electron density of the Fe atom in $S–FeN_4$ is lower than that of the Fe atom in FeN_4 (Fig. 6d). This observation suggests that the presence of the external S atom influences the electronic distribution of the active site of FeN_4 as well as the spin state of Fe. The emergence of a higher valence state and spin state of Fe signifies an augmentation in the number of unpaired electrons. As a result, an optimized reactant adsorption and desorption capability was achieved at the active site of FeN_4, leading to enhanced ORR activity with the most positive E_{onset} of 0.99 V and $E_{1/2}$ of 0.88 V among all catalysts (Fig. 6e). Moreover, Chen et al. [131] developed a strategy that combines matrix activation with controlled induction to design and construct $Co_1N_4–S_1$ active site with axial Co–S coordination by inducing the coordination of cobalt Por (CoPor) molecules with S and N co-doped carbon materials. The AC-HAADF-STEM image and corresponding structure details of the active site are illustrated in Fig. 6f, g. Benefiting from these unique structural characteristics, $Co_1N_4–S_1$ showed high ORR reactivity and remarkable ORR kinetics in alkaline solution, with $E_{1/2}$ of 0.897 V and J_k of 6.1 mA cm^{-2} (Fig. 6h).

3.1.4 Halogen (Cl/I) Ligand Axially Coordinated SACs for ORR

Apart from typical axial ligands that contain N, O and S atoms, halogen ligands can also be introduced to axial coordination site of M–N–C catalysts. Axial Cl coordination offers an effective means for modulating the surface electronic structures, thereby expediting the 4e$^-$ pathway kinetics by near-optimal adsorption of intermediates. Xin et al. [132] synthesized Fe–N/C SACs, and the structural characteristics of the catalyst were confirmed by EXAFS analysis. The Fe atom is situated at the center of a double-vacancy cavity, which is bonded by four in-plane N atoms and one axial Cl atom, forming the $FeN_4–Cl$ active site anchored within the graded porous carbon matrix (Fig. 7a, b). The catalytic performance of Fe–N/C SACs is enhanced by the Cl axial coordination to the active site, exhibiting excellent alkaline ORR activity with $E_{1/2} = 0.91$ V and J_k up to 55 mA cm^{-2} at 0.85 V in 0.1 M KOH, which are respectively 20.8 and 11.5 times higher than those of N/C and Pt/C catalysts (Fig. 7c).

Notably, the ORR catalytic activity of SAC can be further increased through the synergistic effect of axial Cl coordination and S-doping in the carbon substrate. Using the thermal migration method, Han et al. [133] fabricated an atomically dispersed $FeCl_1N_4$/CNS catalyst. Figure 7d, e illustrates respectively the synthetic strategy of $FeCl_1N_4$/CNS and the outstanding ORR activity of the catalyst in alkaline solution, with $E_{1/2} = 0.921$ V, surpassing that of non-noble metal electrocatalysts reported to date, including FeN_4/CN counterpart. Experiments and DFT calculations demonstrated that the electronic state of a single Fe active center can be modulated by its surrounding chemical environment, elucidating

https://doi.org/10.1007/s40820-023-01196-1

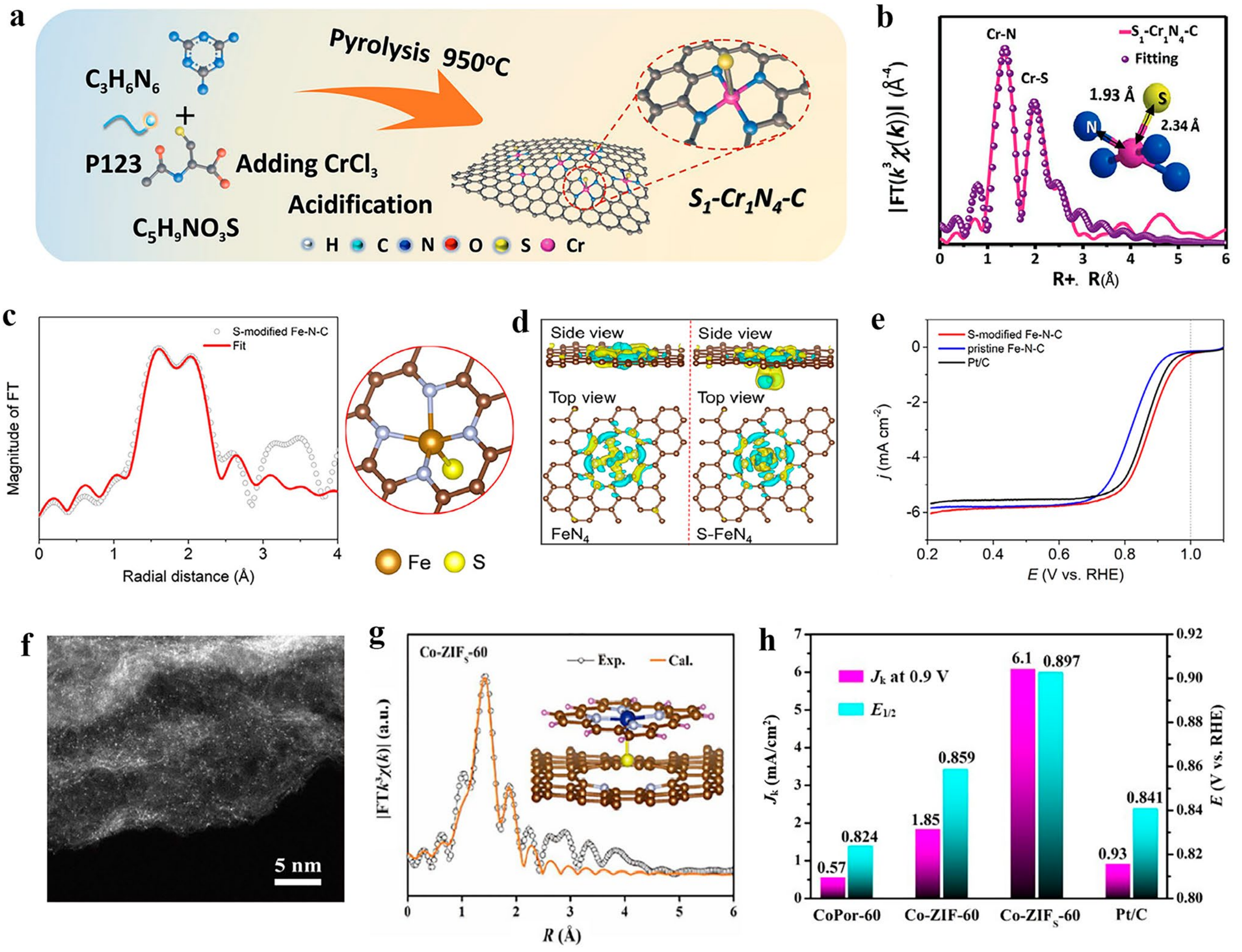

Fig. 6 **a** Synthetic procedure of the Cr single-atom anchored on N, S co-doped porous carbon nanosheet (S_1–Cr_1N_4–C). **b** Cr K-edge EXAFS fitting analysis of S_1–Cr_1N_4–C in K space. Reproduced with permission [129]. Copyright: 2023 Wiley-VCH GmbH. **c** EXAFS fitting at R space for S-modified Fe–N–C and the proposed model for S–FeN4. **d** Spatial charge density difference isosurfaces of S–FeN4 and FeN4. Yellow and blue iso surfaces represent electron accumulation and electron depletion, respectively. **e** LSV curves at 1600 rpm of S-modified Fe–N–C, pristine Fe–N–C, and Pt/C. Reproduced with permission [130]. Copyright: 2023 Wiley-VCH GmbH. **f** AC-HAADF-STEM image of Co-ZIFS-60 sample. **g** The experimental and calculated FT-EXAFS spectra of Co1N4-thiophene S1 (Co-ZIFS-60) based on the DFT model shown in the inset. Schematic model, Co (blue), N (blue), C (gray), S (yellow), and H (pink). **h** Comparison of J_k at 0.90 V and $E_{1/2}$ of different samples. Reproduced with permission [131]. Copyright: 2022, Springer Nature Switzerland AG. (Color figure online)

the reason for the superior ORR activity of $FeCl_1N_4$/CNS. Besides, Zhang et al. [134] obtained axial Cl coordinated Fe–N_4 catalyst bearing resemblance to tetraphenyl porphyrin (FeTPPCl) with the FeN_4 component predominantly adopting a twisted square-cone coordination geometry. The synergy between the rich N-doping in the carbon substrate and the axial Cl coordination in Fe–N_4 active site enables the catalysts an outstanding ORR performance.

To uncover the origin of the high ORR activity after axial coordination, Ding et al. [135] synthesized Cl-axially modified Fe–N–C SACs (FeN_4Cl SAC) to evaluate its electrocatalytic performance for ORR. Subsequently, they constructed various structural models for FeN_4Cl SAC and conducted DFT calculations to further clarify the nature of active sites. The results showed that the original FeN_4Cl–C configuration exhibited the most significant exothermic behavior and strongest ORR activity compared to FeN_4Cl (FeN_4Cl–C-1 and FeN_4Cl–C-4) with carbon defect structures. The introduction of Cl facilitated charge transfer within the Fe active site from N atom to Cl atom in the

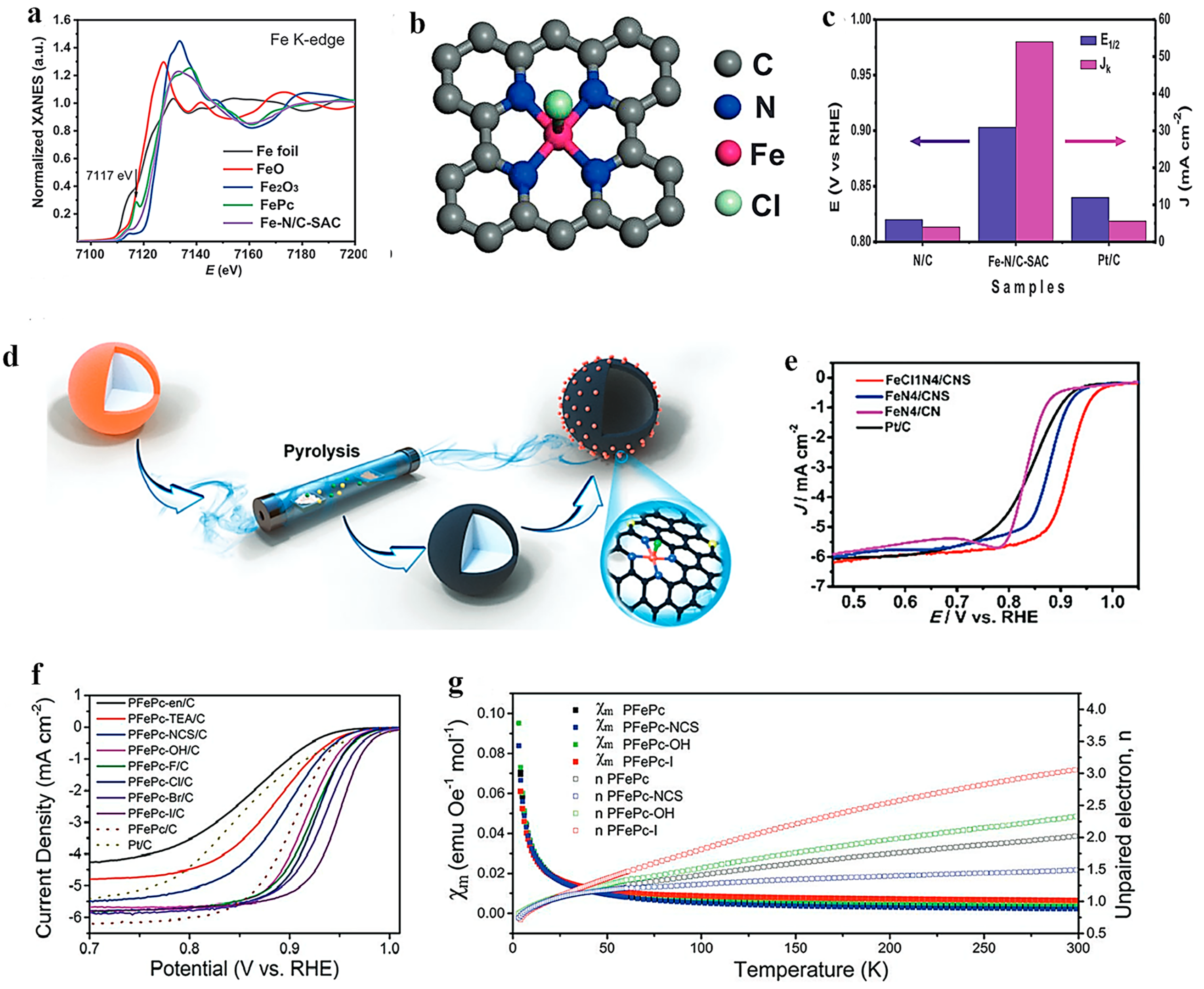

Fig. 7 **a** Fe K-edge XANES spectra for Fe–N/C-SAC. **b** The proposed Cl–Fe–N_4 structural model. Fe, N, Cl, and C atoms are shown in pink, blue, green, and gray, respectively. **c** Comparison of J_k at 0.85 V and $E_{1/2}$ of N/C, Pt/C, and Fe–N/C-SAC. Reproduced with permission [132]. Copyright: 2021 Wiley-VCH GmbH. **d** Schematic illustration of the synthesis of FeCl1N4/CNS. **e** ORR polarization curves in O2-saturated 0.1 M KOH. Reproduced with permission [133]. Copyright: 2018 The Royal Society of Chemistry. **f** LSV curves at a scan rate of 10 mV s^{-1} on the as-prepared PFePc-L/C and Pt/C electrodes under a rotation rate of 1600 rpm in a 0.1 M KOH electrolyte at room temperature. **g** M–T curves and the calculated number of the unpaired electrons in the Fe 3d orbitals in PFePc, PFePc–NCS, PFePc–OH, and PFePc–I. Reproduced with permission [138]. Copyright: 2022 Wiley-VCH GmbH. (Color figure online)

graphene structure, thereby enhancing the ORR activity. The projected density of states (PDOS) of different configurations of Fe d-orbitals, N p-orbitals, and Cl p-orbitals further demonstrates the exceptional ORR catalytic activity of FeN_4Cl–C. Compared to FeN_4–C SAC, the FeN_4Cl–C configuration exhibits a stronger intensity near the Fermi level, which can lead to an enhancement in ORR activity.

In recent years, the utilization of metal–organic frameworks (MOFs) as precursors for the preparation of SACs has attracted significant attention from researchers [136]. As a type of porous crystalline solids, MOFs with readily structural modifications hold great potential as precursors/self-sacrificial templates for the synthesis of SACs with axial coordination. Hu et al. [64] obtained SACs by pyrolysis of 4,5-dichloro imidazole-modified Zn/Fe- bimetallic triazole (MET) framework with high N content. Thanks to the unique properties of MET with rich concentration of N atoms in triazole, the high-density Fe singe-atom with an FeN_4Cl_1 configuration was achieved. FeN_4Cl_1/NC shows excellent ORR activity in both alkaline and acidic electrolytes. DFT calculations demonstrate that the presence of Cl can optimize the adsorption free energy of Fe sites for *OH, thus promoting the ORR process. Besides the commonly used ORR active transition metals like Fe, the generally non-active transition metal elements can also exhibit high ORR activity by axial coordination design in their corresponding SACs. For example, Ji et al. [137] synthesized various YN_4 SACs with different axial coordination designs using different ligands. After comparing a series of axial ligands, it was discovered that the axial Cl coordination can significantly enhance the ORR activity of YN_4 SAC in alkaline solutions, which is comparable to that of Pt/C catalyst. DFT calculations found that there was moderate coupling between the 3p orbital of Cl atom and the 4d orbital of Y, so the covalent bond of YN_4–Cl was extended adaptively to promote the binding of intermediates in ORR process.

In addition to Cl ligand, I ligand has also been utilized in the investigation of the axial coordination of SACs. To elucidate the actual structure and catalytic mechanism of Fe–N_4 SAC, Zhao et al. [138] used poly (iron phthalocyanine) (PFePc) as a model electrocatalyst and investigated the ORR catalytic activity mechanism via axial coordination control on the active site. They selected a series of ligands with different field strengths including strong-field ligands such as ethylenediamine (en), triethylamine (TEA), and NCS, and weak-field ligands such as OH, F, Cl, Br, I to axially coordinate with the Fe–N_4 site in PFePc (denoted as PFePc–L, L = axial ligand). The study revealed a positive correlation between ligand field strength and the ORR catalytic activity of Fe–N4, as evidenced by the gradual increase in both $E_{1/2}$ and J_k of ORR on the PFePc-L/C electrode with decreasing ligand field strength (Fig. 7f). In particular, the PFePc–I/C catalyst displayed a remarkably high $E_{1/2}$ of 0.948 V, which stands out as the highest among all reported Fe–N_4 based catalysts. Experimental results indicated that by axially coordinating the Fe center with ligands of varying field strengths, the three-dimensional orbital configuration and electron spin state of Fe–N_4 can be manipulated according to the crystal-field theory (Fig. 7g). DFT calculations further demonstrated that axial ligand coordination not only rearranges the Fe 3d-orbital configuration but also leads to a reduction in orbital energy levels, resulting in higher ORR activity.

3.1.5 Other Ligands Axially Coordinated SACs for ORR

Apart from the aforementioned heteroatom-based axial ligands, carbon-based ligands can also function as axial coordination ligands in SACs. In such cases, the axial C atom is usually from the carbon support, this coordination aims to enhance the metal-support interaction and stabilize the metal atom in the catalyst. In the study conducted by Yan et al. [139], the FePc molecules were initially subjected to oxidation and doping via the Hummer method. Then, carbon-anchored FePc composites (FePc-RCNTs) were synthesized by integrating FePc precursor and oxidized MWCNTs at room temperature, in which an axial covalent bond between the carbon matrix and Fe–N_4 site was established. FePc-RCNTs exhibited a positive $E_{1/2}$ of 0.86 V in ORR, and the Tafel analysis indicated that the strong interaction between FePc and MWCNTs facilitated the kinetic process in ORR catalysis.

In addition to direct coordination with C atoms from carbon substrate, other C-containing groups as axial ligands are also reported. For example, Luo et al. [140] designed a two-dimensional metal–organic material Fe-Pp flake with an axial cyanide (–CN) ligand. DFT calculation revealed that the Fe-Pp–CN sheet exhibits higher ΔG_{*OOH}, ΔG_{*O}, and ΔG_{*OH} values compared to those of the pristine Fe-Pp sheet, indicating a weakened binding interaction between these intermediates and the Fe-Pp sheet upon axial CN ligand coordination. Combined with external tensile strain, the ORR activity of the Fe-Pp–CN sheet can be further enhanced, even surpassing that of Pt. In order to evaluate the impact of axial C ligands, researchers employed DFT calculations to conduct a series of investigations into the effects of various axial ligands on the catalytic performance of SACs for ORR. For instance, She et al. [141] studied the ORR performance of CrN4-Gra modified with diverse axial C ligands, including –CH, –CH_2, –CH_3, –NH, –NH_2, –NH_3, –C_6H_5 (benzene), –C_6H_5–NH_2 (aniline), and –C_6H_5–NO_2 (nitrobenzene). It was determined that CrN_4-Gra modified with ligands –CH_3, –C_6H_5, –C_6H_5–NH_2, and –C_6H_5–NO_2 exhibited favorable ORR activity with low overpotentials of 0.37, 0.35, 0.37, and 0.29 V respectively. Moreover, after axial coordination of these ligands with various MN_4-Gra compounds, they further found that –C_6H_5–NO_2 and –C_6H_5 exhibit the highest catalytic activity. Specifically, FeN_4-Gra/C_6H_5–NO_2 demonstrated the highest catalytic activity, followed by RuN_4-Gra/C_6H_5–NO_2 and FeN4-Gra/C_6H_5. These findings provide valuable guidance for future experimental investigations into highly efficient ORR catalysts. Furthermore Lu et al. [142] conducted a systematic investigation on the catalytic activity and ligand coordination effects of 17 five-coordinated Fe–N–C catalysts (Fe–N–C–X, X represents axial ligands) through DFT calculations. The findings indicated that the axial coordination effect can diminish the orbital hybridization between Fe active sites and ORR-related intermediates, thereby expediting ORR. More importantly, it was observed that the catalytic activity of Fe–N–C–X exhibited an upward trend as the electronegativity of the X ligand decreased. Among the 17 Fe–N–C catalysts modified with axial ligands, the –SCN ligands modified electrocatalyst exhibited the most favorable OH adsorption energy, resulting in superior ORR activity and a lower overpotential of 0.28 V.

Phosphorus (P) is another heteroatom-based axial ligand reported for the modification of SACs. Studies have shown that the Co single atom coordinated by N and P-doped porous carbon (Co–N, P–C) exhibits slightly higher ORR catalytic activity compared to that coordinated by only N-doped porous carbon (Co–N–C), indicating the advantageous role of P-related species in ORR electrocatalysis [143]. Therefore, employing P-related species as axial ligand in SACs has emerged as a promising strategy to enhance their ORR performance. Zhu et al. [144] synthesized a hollow carbon structure embedded with N, P-coordinated iron atoms (FeNPC) via a facile polymerization-carbonization route. The co-coordination of Fe atoms with N and P on the surface of carbon spheres serves as the active center for ORR, where FeN_4 is axially coordinated with PO_4 group. Impressively, the prepared FeNPC catalyst showed remarkable ORR performance in both alkaline and acidic electrolytes.

Besides the well-documented non-metallic heteroatoms serving as axial ligands, principally single metal atoms, metalloid clusters and metal-containing molecules may also function as ligands to fine-tune the ORR electrocatalytic activity of SACs. However, research on the axial coordination of SACs with metal ligands is limited. Zeng et al. [145] synthesized Pt single-atom grafted Fe–N–C SACs (Pt_1@Fe–N–C), which introduced a novel active site of Pt_1O_2–Fe_1N_4 with axial coordination of Pt_1O_2. They employed X-ray absorption spectroscopy, encompassing both XANES and EXAFS techniques, to propose two plausible configurations for the novel Pt_1O_2–Fe_1N_4 moiety in Pt_1@Fe–N–C. In PEMFC testing, the grafted Pt_1O_2 not only imparted Pt_1@Fe–N–C a high power density, but also had a protective effect on slightly reduced Fe^{3+} atoms, thereby mitigating the catalytic Fenton's reaction of Fe centers. This approach presents a novel perspective on the Fe–N–C system and its potential functional expansion. In addition to metal atoms, metalloid clusters can also act as axial ligands in SACs. By mimicking the conformational kinetics of enzymes during the reaction process, Ji et al. [146] introduced p-block metalloid cluster Te_n into the pyrolytic FeN_4-carbon framework to synthesize an axial Te_n ligand modified catalyst (FeN_4–Te_n). The atomic-resolution aberration-corrected HAADF-STEM revealed the well-dispersed Fe atoms in the carbon support, and a significant number of Te clusters were present in the catalyst. Fe single atoms (Fe-SAs) were observed to be distributed around Te clusters, indicating a strong interaction between them. Synchrotron radiation XAS measurements at the Fe K-edge further determined the chemical state and coordination environment of FeN_4–Te_n at the atomic level. The results indicate that the isolated Fe single-atom is coordinated by four N atoms and approximately one Te atom. Further investigation demonstrated that the FeN_4–Te_n exhibited exceptional electrocatalytic ORR performance in alkaline medium. DFT calculations revealed that the coordination environment and electronic structure of the Fe center can be dynamically controlled by p–d orbital coupling between Te_n clusters and FeN_4 elements when $n > 2$. Moreover, the presence of a fifth electron-absorbing Te_n cluster ligand results in additional weakening of the binding energy of *OH on Fe centers.

3.2 Carbon Dioxide Reduction Reaction

The electrochemical reduction of CO_2 into high-value chemicals and fuels is a promising avenue for utilizing renewable electricity and mitigating CO_2 emissions [147], which has become a cutting-edge field of energy conversion and carbon neutrality [148]. Electrocatalytic CO_2RR is a complex process involving multiple proton-coupled and electron-transfer steps. By adjusting different catalytic systems and electrode potentials, the selectivity of products can be regulated while optimizing the reaction rate under ambient temperature and pressure conditions. In the process of electrocatalytic CO_2RR, CO_2 can be reduced by 1, 2, 4, 6, and 8 electrons under the action of different catalytic systems. Reduction products can be broadly classified into two categories: C_1 products (such as CO, formic acid, and methane) and C_2/C_{2+} products (including ethylene and acetone). Due to the similar reaction potentials, HER is the main competitive reaction in the CO_2RR process. According to the analysis of reaction pathways based on existing literature, it has been found that different products may share common initial or intermediate stages. Among various reaction intermediates, *CO plays a crucial role in both C_1 and C_2/C_{2+} reaction pathways. Based on some mainstream views, the *CO intermediates may undergo direct desorption, further hydrogenation to form C_1 product, or experience dimerization and hydrogenation during C_2/C_{2+} reaction pathway. This is closely related to the binding energies between intermediates and the surface of the catalysts.

In recent years, the development of SACs for CO_2 conversion has rapidly progressed due to their high atomic utilization and demonstrated high specific product selectivity. SACs for CO_2RR can be classified into two categories based on the type of active metal center: noble metals and non-noble metals. However, non-noble metal SACs are currently limited by their impractical current density and suboptimal catalytic selectivity. To meet the economic demands of large-scale industrial applications, it is critical to design and develop exceptional non-noble metal SACs with significant electrocatalytic performance. Various strategies have been developed to improve the electrocatalytic CO_2RR performance of non-noble metal SACs, including coordination structure control [149], deposition of single atom sites onto highly porous supports [150], heteroatom doping, single atom alloying, increasing site density and introducing defect sites [151]. It is worth mentioning that the axial coordination of SACs has emerged to be an intriguing method for effectively regulating the catalytic activity, selectivity, and stability of single atom sites toward CO_2RR. The introduction of axial ligands can lead to the formation of asymmetric coordination for metal single atoms, which disrupts the electronic structure balance of metal single atoms, resulting in variations in electron density distribution that ultimately impact catalyst activity. While classic SACs with $M–N_4–C$ planar structures exhibit excellent performance in electrocatalytic CO_2RR, the high electronic structure symmetry of its $M–N_4$ site impedes electron transfer during catalysis, which hinders the optimization of its catalytic performance. Therefore, designing axial coordination environment to break the electronic structure symmetry of $M–N_4$ sites could be a feasible strategy for enhancing the intrinsic activity of central metal atoms and significantly improving the catalytic performance. As summarized in Table 2, the attempts reported so far mainly focus on $M-N_4$ (M: Fe, Co, Ni), and the central transition metal atoms determine these catalysts tend to the CO_2-to-CO reaction pathway, which has been proven in many previous studies. The axial coordination strategy can further suppress the side reaction HER and improve catalyst performance while keeping the main products unchanged. Therefore, our subsequent discussion will mainly focus on the impact of introducing axial coordination to SACs on electrocatalytic CO_2RR for CO production.

3.2.1 Nitrogen (N) Ligand Axially Coordinated SACs for CO_2RR

Atomically dispersed Fe atoms immobilized on an N-doped carbon matrix have gained significant attention in the field of CO_2RR. In most reports, $Fe–N_4$ has been identified as the active site of Fe–N–C catalysts owing to their excellent CO_2RR performance [172]. Based on the planar $Fe–N_4$ structure, introducing an axial Fe–N bond to form an $Fe–N_5$ structure is a common strategy for regulating the local coordination environment of the Fe site and enhancing CO_2RR performance. By incorporating aminated CNTs, Tuo et al. [152] successfully fabricated an axial $Fe–N_5$/CNT catalyst with four planar Fe–N coordination and one axial Fe–N coordination. Compared to the planar $Fe–N_4$/CNT, the additional axial Fe–N coordination effectively lowered the energy barrier for CO desorption, suppressed HER occurrence, and enhanced CO selectivity during CO_2RR process. Cheng et al. [153] synthesized an $Fe–N_5$ single-atom catalyst (Fe-SA/ZIF) via pyrolysis, and demonstrated its potential as a highly efficient catalyst material. This catalyst exhibited an FE_{CO} of 98% at –0.7 V vs. RHE, surpassing the majority of reported SACs to date. Its superior performance can be attributed to the out-of-plane coordinated axial pyridinic N, which led to a negative shift of the *d-band* center and weakened the binding strength between the adsorbent and active site according to the *d-band* theory. The partial density of states (PDOS) calculation indicated that the *d-band* centers of FeN_4 and FeN_5 experienced varying degrees of negative shifts due to orbital hybridization between the C-2p orbit of the CO intermediate and Fe-3d orbit. The corresponding values are 0.91 and 1.15 eV for $Fe–N_4$ and $Fe–N_5$, respectively.

Table 2 Summarized electrocatalytic CO$_2$RR activity of typical axial coordination modified SACs

Axial-coordinated SACs	Coordination structures	Axial atom	Main products	FE[a]	Partial current density[b]	Stability (h)	Refs
Fe–N/CNT	Fe–N$_5$	N	CO	95.47%@-0.6 V	–	10	[152]
Fe–SA/ZIF	Fe–N$_5$	N	CO	98.0% @-0.7 V	7.1 mA cm^{-2}@-0.7 V	40	[153]
Fe–N$_5$/DPCF	Fe–N$_5$	N	CO	93.1% @-0.5 V	9.4 mA cm^{-2}@-0.49 V	25	[154]
Ni–N$_5$–C	Ni–N$_5$	N	CO	99.6% @-2.4 V	1.23 A cm^{-2}@-2.4 V	100	[155]
FeN$_5$	Fe–N$_5$	N	CO	97.0%@-0.35 V	0.5 mA cm^{-2}@-0.35 V	24	[156]
CoPc–py–CNT	Co–N$_4$–py	N	CO	98.8%@-0.63 V	9.9 mA cm^{-2}@-0.73 V	12	[157]
Co–N$_5$/HNPCSs	Co–N$_5$	N	CO	99.2%@-0.73 V	4.4 mA cm^{-2}@-0.73 V	10	[158]
Ni SAs/OMMNC	Ni–N$_4$–O	O	CO	99.0% @-0.6 V	5.1 mA cm^{-2}@-0.6 V	17	[159]
NiSA–N–PGC	Ni–N$_4$–O	O	CO	97.2%@-0.76 V	53 mA cm^{-2}@-1.1 V	40	[160]
NiN$_4$–O$_2$–FePc	Ni–N$_4$–O$_2$	O	CO	97.65%@-0.5 V	252 mA cm^{-2}@-0.5 V	20	[161]
Ni-NUK-900	Ni–N$_4$–O	O	CO	94.0%@-0.73 V	3.4 mA cm^{-2}@-0.73 V	12	[162]
O–Fe–N–C	Fe–N$_4$–O	O	CO	95.0% @-0.5 V	4.4 mA cm^{-2}@-0.5 V	30	[163]
Fe–N/O–C (MZ)	Fe–N$_4$–O	O	CO	96.0%@-0.57 V	5.4 mA cm^{-2}@-0.57 V	22	[164]
Fe–CON$_{400}$-400	Fe–N$_4$–O	O	CO	~100%@-0.83 V	-	12	[165]
SnPc/CNT–OH	Sn–N$_4$–O	O	HCOOH	89.4% @-1.0 V	74.8 mA cm^{-2}@-1.0 V	8	[166]
Ni–N$_4$–O/C	Ni–N$_4$–O	O	CO	99.2% @-0.9 V	23 mA cm^{-2}@-0.9 V	20	[66]
CdN$_4$S$_1$/CN	Cd–N$_4$–S	S	CO	99.7%@-2.4 V vs Ag/Ag$^+$	–	24	[167]
ZnN$_4$S$_1$/P–HC	Zn–N$_4$–S	S	CO	~100% @-0.6 V	15.8 mA cm^{-2}@-0.8 V	30	[168]
FeN4Cl/NC-7.5	Fe–N4–Cl	Cl	CO	90.5% @-0.6 V	10 mA cm-2@-0.8 V	15	[169]
(Cl, N)–Mn/G	Mn–N$_5$–Cl	Cl	CO	97% @-0.6 V	14.3 mA cm^{-2}@-0.8 V	–	[170]
Ni1–N–C(Cl)	Ni–N$_4$–Cl	Cl	CO	94.7% @-0.7 V	2.75 mA cm^{-2}@-0.7 V	10	[171]
Ni1–N–C(Br)	Ni–N$_4$–Br	Br	CO	83.3% @-0.65 V	0.9 mA cm^{-2}@-0.65 V	–	[171]
Ni1–N–C(I)	Ni–N$_4$–I	I	CO	69.4% @-0.65 V	0.4 mA cm^{-2}@-0.65 V	–	[171]

[a,b] The reported potentials are with respect to the reversible hydrogen electrode (V vs. RHE) unless otherwise stated

Therefore, Fe–N$_5$ with axial pyridine N coordination exhibited a greater advantage in CO desorption.

In addition, axial ligands can synergistically collaborate with defects to further improve the CO$_2$RR performance of the catalyst. Li et al. [154] designed a facile electrospinning and two-step annealing strategy to successfully prepare Fe–N$_5$ SACs on defect-rich porous carbon nanofibers, denoted as Fe–N$_5$/DPCF (Fig. 8a). As shown in Fig. 8b, c, Fe–N$_5$/DPCF exhibited significantly enhanced CO$_2$RR performance across a broad potential range compared to Fe–N$_x$/PCF. DFT calculations were performed to further investigate the structure–property–performance relationships resulting from axial coordination and defect-rich supports. The DOS calculation showed that the introduction of an axial N-ligand results in a negative shift in the *d-band* center of Fe atoms. Furthermore, due to the alterations in the nature of active site, defects further enhance this negative shift (Fig. 8d). As a result, the adsorption behavior of reactants and intermediates underwent changes during the reaction process, resulting in promoted *CO desorption and *COOH formation while inhibiting *H formation. Benefiting from these property modifications, the selectivity of the catalyst has been improved.

In addition to Fe–N–C materials, other M–N–C materials also show great potential as catalysts for CO$_2$RR, but their current density and durability are still insufficient. To address this issue, researchers have made diverse endeavors. Huang et al. [155] synthesized a Ni–N$_5$–C catalyst with an enzyme-like structure (Fig. 8e), which exhibited exceptional electrocatalytic performance for CO$_2$ to CO, achieving an ultra-high current density of 1.23 A cm^{-2} at–2.4 V vs. RHE and remarkable durability (Fig. 8f). The mechanism study showed that the introduction of axial N-coordination can improve the degree of electron delocalization on the active site surface and lead to a distinct Fe 3d orbital splitting in contrast to the classical Ni–N$_4$ structure. Additionally, a mesoporous nanosphere-supported

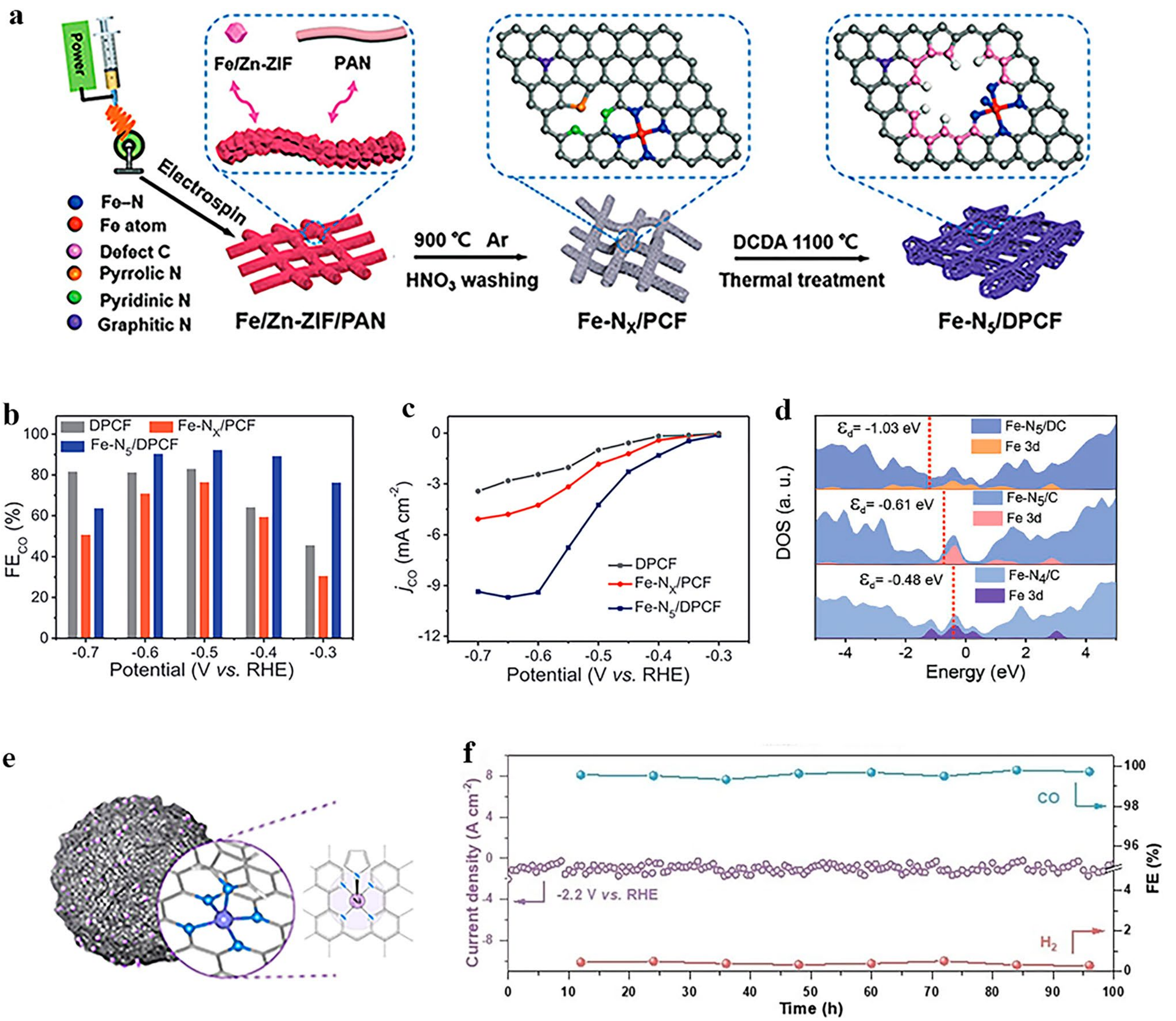

Fig. 8 **a** Schematic diagram of the preparation procedure of Fe–N_5/DPCF. **b** CO Faradaic efficiencies, and **c** CO partial current densities of DPCF, Fe–Nx/PCF, and Fe–N_5/DPCF at different potentials. **d** The total DOS (red-shaded areas) and d-states of Fe atom (blue-shaded areas) in the optimized structures of FeN_4/C, FeN_5/C, and FeN5/DC. Reproduced with permission [154]. Copyright: 2022 Wiley-VCH GmbH. **e** Coordination configuration of the Ni–N_5–C single-atom nanoenzyme. **f** Long-term stability test of Ni–N_5–C for CO_2RR operated at − 2.2 V vs. RHE. Reproduced with permission [155]. Copyright: 2022 Wiley-VCH GmbH

catalyst with axial Co–N_5 coordination and hierarchical pore structure was synthesized [173]. A series of experiments and theoretical calculations demonstrated that the initiation of localized d–p orbital hybridization by axial N-coordination can effectively enhance the oxidation state of Co. When combined with an optimized pore structure, the catalyst exhibited significantly improved performance in CO_2RR.

3.2.2 *Oxygen (O) Ligand Axially Coordinated SACs for CO_2RR*

The electronic structure of the metal central site can likewise be tuned by introducing an axial coordination of O atoms, and thus improving the activity of SACs in CO_2RR. With higher electronegativity of O than N, SACs axially coordinated with O ligands exhibit even greater performance enhancement compared to those coordinated with axial N ligands. The metal atoms of Ni–N_4 surrounded by four pyridinic N atoms can introduce additional axial O coordination through various synthetic strategies. Several studies have demonstrated that due to the adjustment of the local geometry and electronic structure of the central atom by axial O ligands, the adsorption and activation of CO_2 on the Ni site have been improved, resulting in changes in formation and adsorption energy barriers for various intermediates, ultimately leading to enhanced CO_2RR performance [159–161, 174]. Employing KOH as the O source, pore-forming agent, and promoter, a SAC with O axial coordination, denoted as Ni-NUK-900, was successfully synthesized, as depicted in Fig. 9a [162]. The XRD and Raman spectra confirmed the atomically dispersed Ni, and the coordination configuration was identified as Ni–N_4–O through EXAFS curve fitting. Ni-NUK-900 displayed excellent CO_2RR performance with a high FE_{CO} of 94% and TOF_{CO} of 11,362 h^{-1} (Fig. 9b). DFT calculations demonstrated that the axially coordinated O atom acts as an electronic regulator at the Ni site, thus optimizing the formation of *COOH and the desorption of *CO. Moreover, extensive research has been made by researchers to explore the Fe–N_4 structure [175], and both experimental and theoretical calculations confirmed the analogous contribution of axial O atoms in enhancing the catalytic CO_2RR performance [163, 164]. Chen et al. [165] proposed a fast-pyrolyzing and controllable-activation strategy to synthesize the atomically dispersed Fe–N_4 site with axial O coordination (Fe_1N_4–O_1), which exhibited nearly 100% FE_{CO} across a broad potential range. DFT calculations revealed that the lower occupancy of the antibonding state of the adsorbed species and Fe_1N_4–O_1 effectively regulated the binding interaction of CO_2RR intermediates. The calculation results further confirmed that the axial O atom with high electronegativity contributed to superior performance of the catalyst in promoting CO_2RR and inhibiting HER.

In a study by Zhao Li et al. [166], the incorporation of O into an Sn–N–C catalyst was investigated. They developed a series of Sn-SACs with well-controlled coordination and electronic structure to examine the activity of reducing CO_2 to HCOOH. The room-temperature Sn Mossbauer spectra revealed that the introduction of the O ligand results in a complete conversion of Sn(II) to Sn(IV), with the percentage reaching 100% (Fig. 9d, e). According to electrochemical performance test data, the ratio of Sn(IV) and Sn(II) positively correlates with the ability of catalyst for HCOOH and CO formation, suggesting Sn(IV) species are most likely the main catalytic sites for CO_2RR to HCOOH (Fig. 9h). Theoretical research confirmed that the O–Sn–N_4 species can adjust the adsorption configuration of *CO_2 by increasing the asymmetric distribution of Sn(IV) orbital electrons, which reduced the energy barrier for *OCHO species formation and hydrogenation, thereby promoting the conversion of CO_2 to HCOOH (Fig. 9g).

Although many studies have validated the practicality of using axial O coordination strategies to enhance the CO_2RR performance of catalysts, conventional methods pose challenges in achieving precise control over the type and content of O atoms. Therefore, it is imperative to explore the approach of incorporating O axial ligands more accurately. Moreover, the activity of the SACs hinges on the intrinsic characteristics of their constituent metal atoms [176]. Thus, selecting the appropriate metal atoms is equally important in obtaining high-performance M–N_4O_1–C SACs for CO_2RR.

3.2.3 *Sulfur (S) Ligand Axially Coordinated SACs for CO_2RR*

S atoms possess high spin density and charge delocalization, which can effectively lower the free energy barriers for intermediates sorption during CO_2RR [177]. Therefore, introducing S atoms as axial ligands into SACs could be a promising approach to enhance their catalytic performance. To investigate the synergistic effects of metal atoms and axial coordination structures on CO_2RR electrocatalysis, Wu et al. constructed various SACs models of diverse metals for DFT simulation calculations [167]. Notably, for Cd-SAC with relatively large atomic size of Cd, they were observed to be situated in the upper region of the graphene layer within the constructed SACs model (as depicted in Fig. 10a). Based on this, the author proposed a reasonable assumption that Cd atoms could potentially coordinate axially with N or S atoms on adjacent graphite layers. In general, the value of ($U_L(CO_2) - U_L(H_2)$) can serve as an indicator of catalyst selectivity. Specifically, a greater positive difference results in higher selectivity for CO_2RR on the corresponding catalyst and weaker competitiveness with HER. As depicted in Fig. 10b, CdN_4S_1 exhibits the most positive ($U_L(CO_2) - U_L(H_2)$) value among all constructed models, indicating its potential for optimal CO_2RR selectivity. Guided by these theoretical calculations, Cd was selected as the active metal and S as the axial coordination atom, the CdN_4S_1/CN catalyst was successfully prepared by calcining amine, hydroxylamine

https://doi.org/10.1007/s40820-023-01196-1

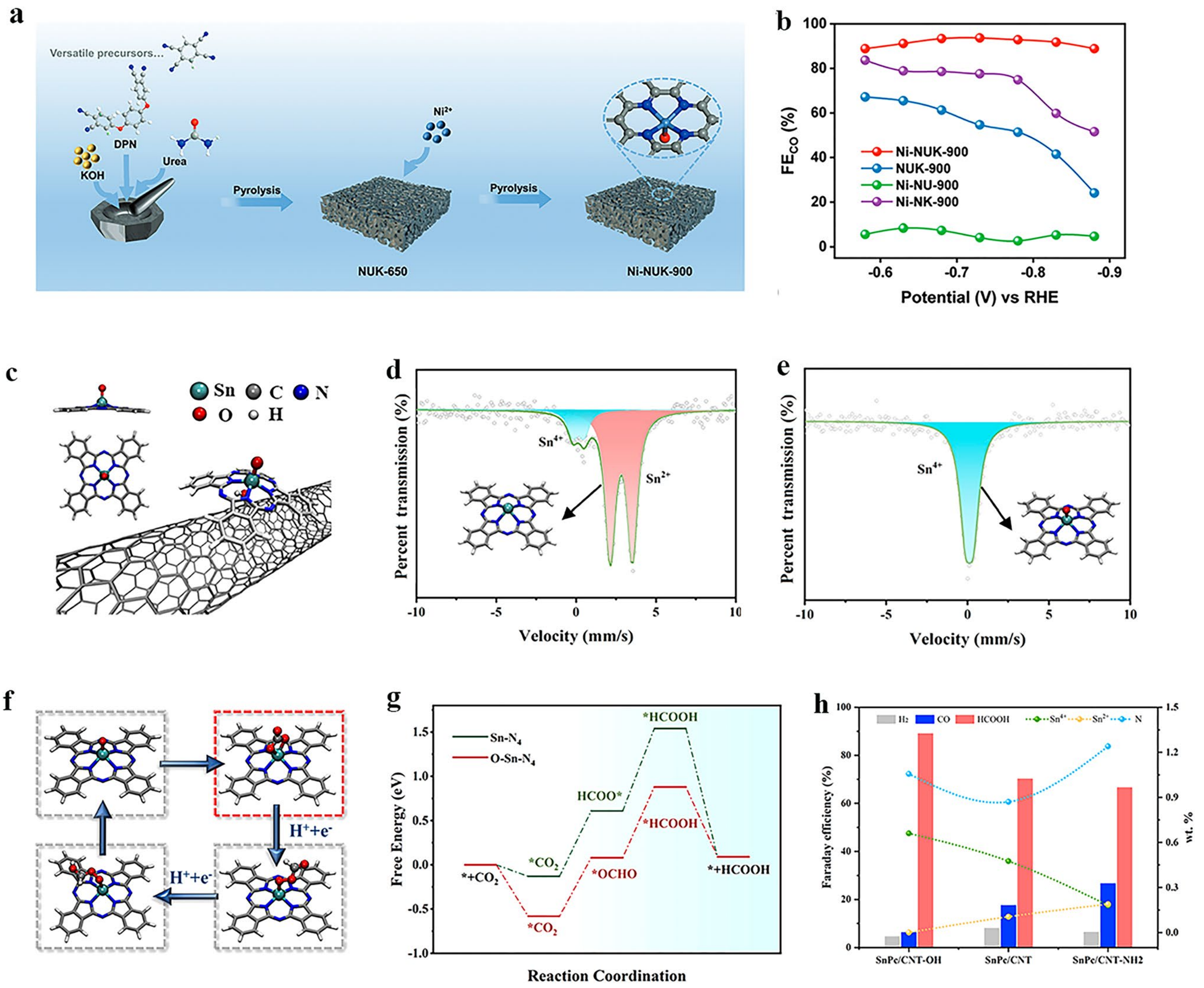

Fig. 9 **a** Schematic diagram of the synthetic process of Ni-NUK-900. **b** FE_{CO} of Ni-NUK-900, NUK-900, Ni-NU-900, and Ni-NK-900 at different applied potentials. Reproduced with permission [162]. Copyright: 2023 Wiley-VCH GmbH. **c** Schematic illustration for the preparation of SnPc/CNT-OH. **d**, **e** Room-temperature Sn Mossbauer spectra for SnPc and SnPc/CNT-OH, respectively. **f** Proposed reaction pathway for CO_2RR over the O–Sn–N_4 site. g Calculated Gibbs free energy diagrams for CO_2RR to HCOOH over O–Sn–N_4 and Sn-N_4 sites, respectively. **h** Correlation diagram of the CO_2RR Faradaic efficiency and the relative contents of Sn(II), Sn(IV), and nitrogen species of SnPc/CNT, SnPc/CNT-OH, and SnPc/CNT-NH_2: FE is indicated as column, while Sn(II), Sn(IV), and N contents are indicated as curves. Reproduced with permission [166]. Copyright: 2023 American Chemical Society

hydrochloride, cadmium chloride, and L-cysteine together in an N_2 atmosphere. The HAADF-STEM images revealed a homogeneous distribution of individual Cd atoms (Fig. 10c). Furthermore, comparison between the experimental and theoretically simulated XANES spectra confirm that the structure of the as-prepared catalyst is in agreement with the theoretical model (Fig. 10d). The FEco and current density of CdN4S1/CN were found to be higher than those of CdN5/CN at the overall potentials, which aligns well with the theoretical calculation results (Fig. 10e, f). The FEco and current density of CdN_4S_1/CN were found to be higher than those of CdN_5/CN at the overall potentials, which aligns well with theoretical calculation results (Fig. 10e, f).

Previous study has demonstrated that introducing P atoms into N-doped carbon materials to form P stabilized at various coordination shells around the central metal atom can effectively decrease the electronic density of metal sites. This significantly reduces the formation energy barrier of *COOH,

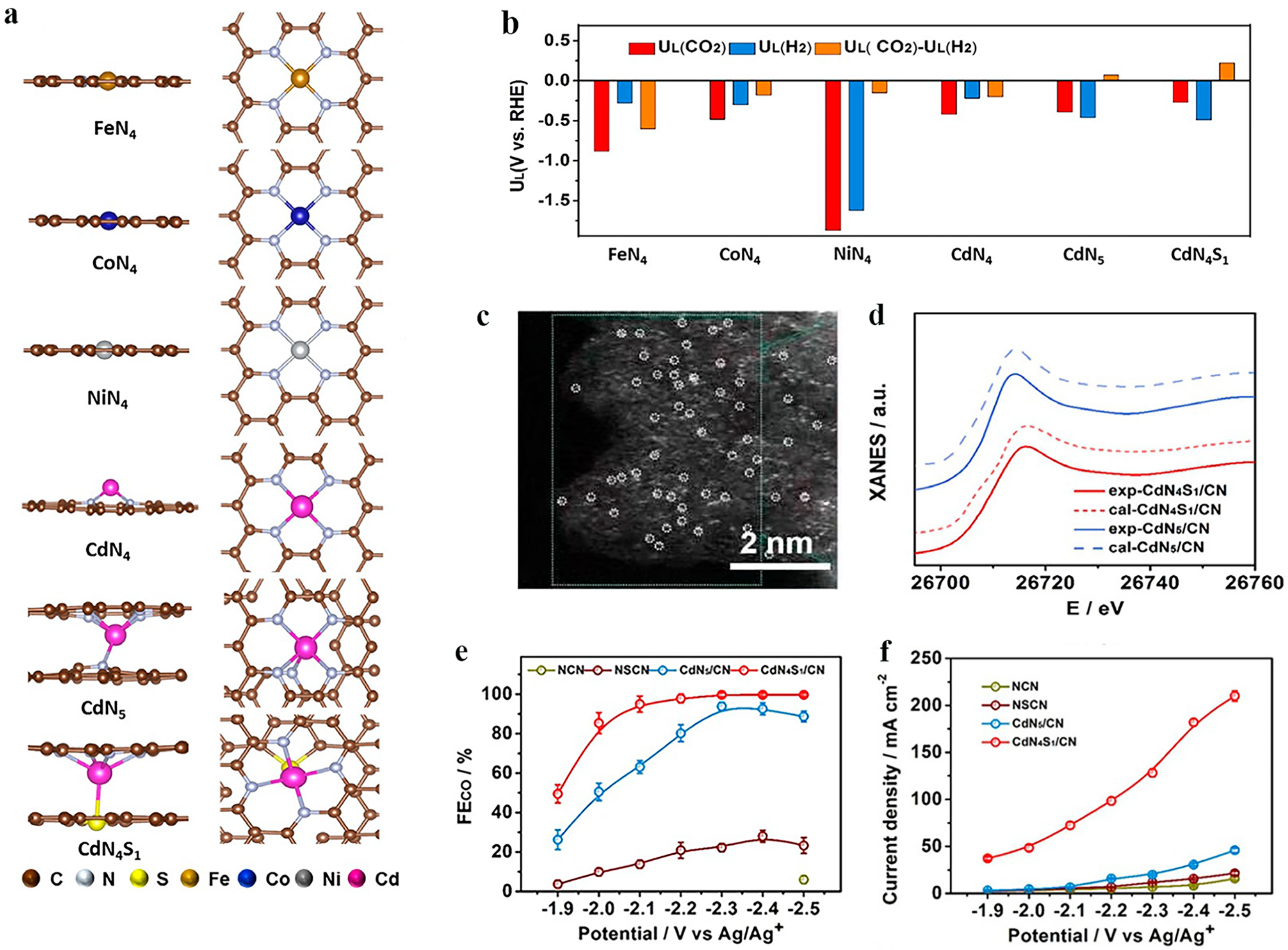

Fig. 10 **a** The side and top views of FeN_4, CoN_4, NiN_4, CdN_4, CdN_5, and CdN_4S_1 models. **b** Difference in limiting potentials for CO_2 reduction and H_2 evolution over different models. **c** HAADF-STEM image of CdN_4S_1/CN. **d** Comparison between the experimental and theoretically simulated XANES spectra of CdN_4S_1/CN and CdN_5/CN. **e** FEs of CO for NCN, NSCN, CdN_5/CN, and CdN_4S_1/CN at different applied potentials. **f** The total current densities for NCN, NSCN, CdN_5/CN, and CdN_4S_1/CN at different applied potentials. Reproduced with permission [167]. Copyright: 2021 Wiley-VCH GmbH

resulting in high CO_2RR performance at low overpotential [178]. Inspired by this, Hu and co-workers [168] employed a "synergistically near- and long-range regulation" strategy to fabricate a ZnN_4S_1/P-HC catalyst. This catalyst features an axial S ligand and is surrounded by P atoms in the carbon matrix, which exhibited excellent CO_2RR performance across a wide potential range, achieving over 90% FE_{CO} with nearly 100% FE_{CO} at −0.6 V vs. RHE. DFT calculations further confirmed that the electronic structures were optimized and the interaction between Zn–N_4 active sites and *COOH was greatly enhanced by synergistic regulation from axially coordinated S and long-range P atoms, which greatly enhanced the electrocatalytic CO_2RR performance. Additionally, a fascinating instance has been observed in which the S atom in diphenyl sulfide was axially coordinated with Co-SACs that were anchored on graphene [179]. The benzene ring of diphenyl sulfide exhibited a strong face-to-face stacking with graphene, and the axial coordination atoms acted as relay molecules to promote interfacial electronic exchange, thus further improving the CO_2RR activity of the catalyst.

3.2.4 *Halogen (Cl, Br, I) Ligand Axially Coordinated SACs for CO_2RR*

In the article reported by Li et al. [169], they demonstrated an example of incorporating axial Cl ligand into an FeN_4Cl/

NC catalysts through a two-step method involving pyrolysis and low-temperature hydrochloric acid incubation. The Fe single atoms exhibit in-plane coordination with four N atoms and one axial Cl ligand. It was found that the FE_{CO} of FeN_4Cl/NC is much higher than the counterpart FeN_4/NC over a wide potential range. Additionally, a high current density of 10.8 mA cm^{-2} was achieved at a low overpotential of 490 mV. DFT calculations revealed that electrons transfer from the axial Cl atom to the central Fe atom, causing a negative shift of the *d-band* center of FeN_4Cl. The reduction in the *d-band* weakens the bonding interaction between adsorbed species, which favors *CO desorption and suppresses *H adsorption, leading to a higher FE_{CO}. Zhang et al. [170] successfully synthesized an Mn-based heterogeneous catalyst through Cl and N dual-coordination tactics. The axial Cl coordination-induced distortion in the single atom Mn center facilitated the adsorption of CO_2 and *COOH, leading to a stable low-energy transition state that promotes final CO desorption. This modification resulted in a maximum FE_{CO} of 97% at 0.49 V vs RHE and an increased partial current density.

Axial halogen atoms with distinct electronegativity can perturb the charge distribution in the original plane of SACs and modulate the electronic state of the central atoms. A strategy of post metal halide modification (PMHM) was developed to precisely adjust the axial coordination environment of SACs at the atomic level. Based on this, Peng et al. [171] synthesized a series of Ni–N–C (X) (X = Cl, Br, I) materials with different halogen axial coordination (Fig. 11a, b). By combining experimental data with theoretical calculation, the crucial role of halogen axial coordination in CO_2RR has been systematically elucidated. Ni–N–C (Cl) possessed high CO partial current densities and a CO selectivity of up to 94.7% in CO_2RR, surpassing those Ni–N–C catalysts axially coordinated with Br and I (Fig. 11c, d). Through theoretical calculations, it was discovered that the axial halogen atom can facilitate the formation of intermediate *COOH, thereby accelerating CO_2RR for CO generation. The variation in electron delocalization degree of Ni atoms caused by the distinct electronegativity of axial halogen ligands is believed to impact the energy barrier of the reaction. For the three different axial halogen ligands studied in this work, it is evident that the electronegativity of axial halogen ligands follows the order $Cl > Br > I$. Therefore, it can be reasonably inferred that Ni transfers more electrons to Cl than Br and I, and Cl axial ligand coordinated Ni–N–C catalyst exhibited the lowest energy barrier for CO_2RR. To confirm this perspective, the free energy change of CO_2 reduction to CO was computed. In the process of CO_2 reduction to CO, the formation of *COOH is commonly regarded as a rate-limiting step. The calculation results showed that the adsorption energy of *COOH follows the sequence Ni–N–C (Cl) < Ni–N–C (Br) < Ni–N–C (I) for SACs with different axial halogen coordination (Fig. 11e), which is consistent with the electronegativity order of relevant halogen atoms. Meanwhile, there were fewer localized electrons between Ni–N–C (Cl) and *CO. The above findings suggest that the interaction between Ni–N–C (Cl) and *COOH is strong, while the interaction with *CO is relatively weak. The fine-tuned intermediate adsorption behavior results in the superior CO_2RR performance of Ni–N–C (Cl).

3.2.5 Other Ligands Axially Coordinated SACs for CO_2RR

With the modification of axial ligands on SACs, the rate-determination step (RDS) of CO_2RR for CO generation can shift from a non-electrochemical step (CO desorption) to an electrochemical control step. This opens up possibilities for optimizing catalyst performance by regulating the applied voltage, pH, and other reaction conditions. The electronic energy levels of central metal atoms can be effectively optimized by the appropriate acquisition or loss of electrons by axial ligands. Due to the differences in the electronegativity of the ligands introduced, metal atom sites experience varying degrees of electron loss. Experiments have shown that M–N–C SACs with axial coordination exhibit remarkable activity in CO_2RR, yet the current literature predominantly concentrates on ligands containing N, O, S, and halogen. Since diverse organic ligands have been employed for the stabilization of metal nanoclusters and nanoparticles. Therefore, in principle, it can also be applied to metal SACs through covalent grafting. Ma et al. [180] investigated a range of axial ligands including both common heteroatom-based ligands and organic ligands for the functionalization of Fe–N_4/Gra, Co–N_4/Gra, and Ni–N_4/Gra SACs. Theoretical calculation results confirmed the significant optimization of axial organic ligands for Fe–N_4/Gra and Co–N_4/Gra SACs. Conversely, the selectivity of Ni–N_4/Gra SAC is weakened by most axial ligands. Liu et al. [181] have

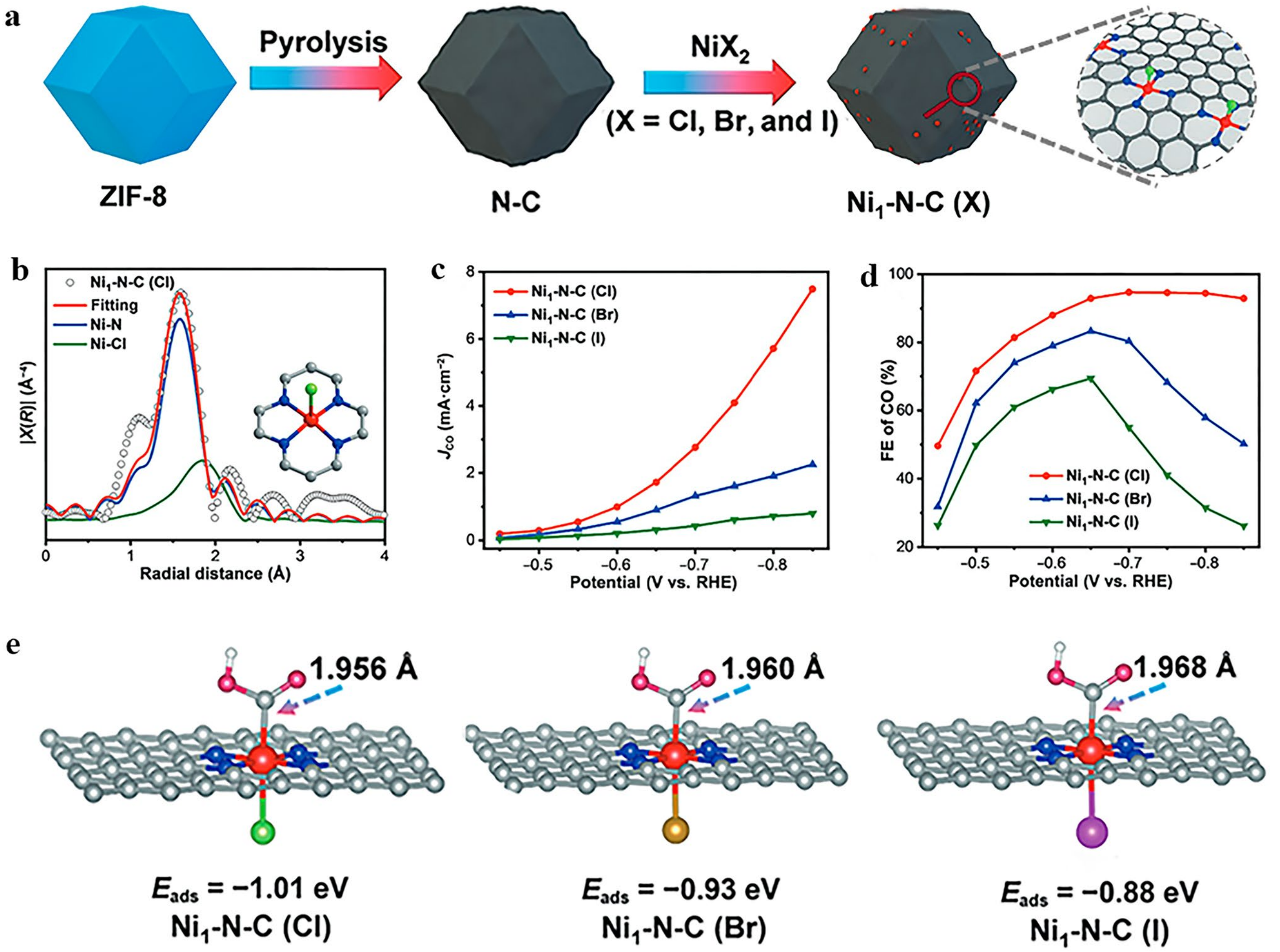

Fig. 11 **a** Illustration for the construction of Ni_1–N–C(X) (X = Cl, Br, and I) single-atom catalysts via a PMHM strategy. **b** EXAFS fitting of Ni_1–N–C(Cl) (inset: optimized coordination configuration of Ni atom). **c** CO partial current densities, and **d** CO FEs of Ni1–N–C(X) (X = Cl, Br, and I). **e** DFT-optimized configurations of Ni_1–N–C(X) (X = Cl, Br, and I) with *COOH adsorption and corresponding adsorption energy. Reproduced with permission [171]. Copyright: 2022, Tsinghua University Press

systematically studied more than 20 p-block elements as axial ligands to tailor the Mo–N_4 structure for CO_2RR. Theoretical calculations revealed the possibility of using p-block elements as axial ligands to improve the performance of the catalyst for two-electron CO_2RR. In contrast to conventional findings, the conclusion of this study highlighted the exceptional performance of Ge–MoN_4 structure in two-electron CO_2RR, providing theoretical evidence for the feasibility of utilizing metal atoms for axial coordination. This offers guidance for the rational design of SACs towards electrocatalytic CO_2RR.

3.3 Hydrogen Evolution Reaction

Electrocatalytic water splitting for hydrogen evolution is considered the best way for green hydrogen production due to its advantages including high energy conversion efficiency, cleanliness, and zero-[182, 183]. During the process, the cathode undergoes the hydrogen evolution reaction (HER), in which H^+ or H_2O obtains two electrons to generate H_2 gas [184]. There are two predominant pathways for HER, namely the Volmer–Tafel mechanism and the

Volmer–Heyrovsky mechanism, which involve subsequent processes.

Volmer step:

$$H^+ + e^- \rightarrow {}^*H \text{ (in acidic electrolyte)}$$

$$H_2O + e^- \rightarrow OH^- + {}^*H \text{ (in alkaline electrolyte)}$$

Tafel step:

$${}^*H + {}^*H \rightarrow H_2 \text{(in acidic and alkaline electrolyte)}$$

Heyrovsky step:

$${}^*H + H^+ + e^- \rightarrow H_2 \text{(in acidic electrolyte)}$$

$$H_2O + e^- \rightarrow H_2 + OH^- \text{(in alkaline electrolyte)}$$

However, this process necessitates crossing high-energy barriers that require catalysts to effectively reduce activation and reaction energies. Therefore, it is crucial to develop HER electrocatalysts with robust performance. SACs have emerged as a new frontier in HER catalysis due to their exceptional atomic utilization, selectivity, and catalytic performance [185]. Both theoretical comprehension and experimental validation have confirmed that SACs exhibit superior performance compared to traditional heterogeneous catalysts in HER catalysis [186]. The synthesis of SACs has attracted widespread attention in HER electrocatalysis. Previously, researchers were mostly committed to regulating the interaction between supports and metal atoms, screening carriers with unique properties, and pursuing the enhancement of single-atom active site loading [187]. In recent years, axial coordination optimization strategy has emerged as a prominent field in the structural design of SACs (Table 3). This section presents an overview of recent advances in the application of SACs modified with axial coordination for HER.

Among the numerous developed electrocatalysts, the excellent HER performance of Pt-based catalysts has been verified. Whereas, in consideration of the scarcity and high cost of noble-metal Pt, developing Pt-SACs and further optimizing their performance is necessary for electrochemical HER in large-scale applications. Therefore, an axial coordination strategy has been attempted by Zhang et al. [77], they synthesized Pt-SACs by anchoring Pt single atom onto NiFe-layered-double-hydroxides (NiFe-LDH). Meanwhile, a facile irradiation-impregnation procedure was employed to achieve a range of heteroatoms axially coordinated Pt-SACs, the final materials are denoted as X-Pt/LDH (X = F, Cl, Br, I, and OH) (Fig. 12a, b). This work explored the impact of various axial ligands with distinct electron affinities on Pt centers in Pt-SACs. The HER activity of X-Pt/LDH was found to follow the order of Cl–Pt/LDH > F–Pt/LDH > HO–Pt/LDH > Br–Pt/LDH > I–Pt/LDH under identical experimental conditions, suggesting the HER activity of Pt-SACs is significantly influenced by axial ligands coordination (Fig. 12c). Among these modified Pt-SACs, the Cl ligand axially coordinated Pt site exhibited optimal adsorption affinity for both *OH and *H due to the higher first electron affinity of Cl axial ligand, thereby promoting the kinetic limiting Volmer step for H_2O dissociation in alkaline HER (Fig. 12d, e). Moreover, there have been investigations on the axial coordination of C ligand to the metal center of SACs for HER. Yin et al. [188] investigated two Pt-SACs, the Pt-GDY1 owns five non-planar-coordinated C_1–Pt–Cl_4 configuration, and the Pt-GDY2 with four-coordinated C_2–Pt–Cl_2 configuration, which have the same ligand atom species but different configurations. Electrochemical testing results showed that Pt-GDY2 exhibited higher electrocatalytic HER activity compared to Pt-GDY1, with a more than threefold increase in mass activity. The performance difference indicates the

Table 3 Summarized electrochemical HER and OER activity of typical axially coordinated SACs

Axial-coordinated SACs	Coordination structures	Axial atom	Reaction	Electrolyte	η_{10} (mV)	Tafel slope (mV dec^{-1})	Refs
Pt–GDY1	C_1–$PtCl_4$	C	HER	0.5 M H_2SO_4	113	52.0	[188]
NiN_4–Cl SAs/N–C	NiN_4–Cl	Cl	HER	1.0 M KOH 0.5 M H_2SO_4	243 274	89.2 96.4	[189]
CoN_4–O/MX	CoN_4–O	O	OER	1.0 M KOH	350	–	[199]
V@NMCNFs	V–O_2N_3	O	OER	0.5 M H_2SO_4	196	25	[200]
P–CoPc@CNT	Co_1N_4–PO_4	P	OER	1.0 M KOH	300	41.7	[201]

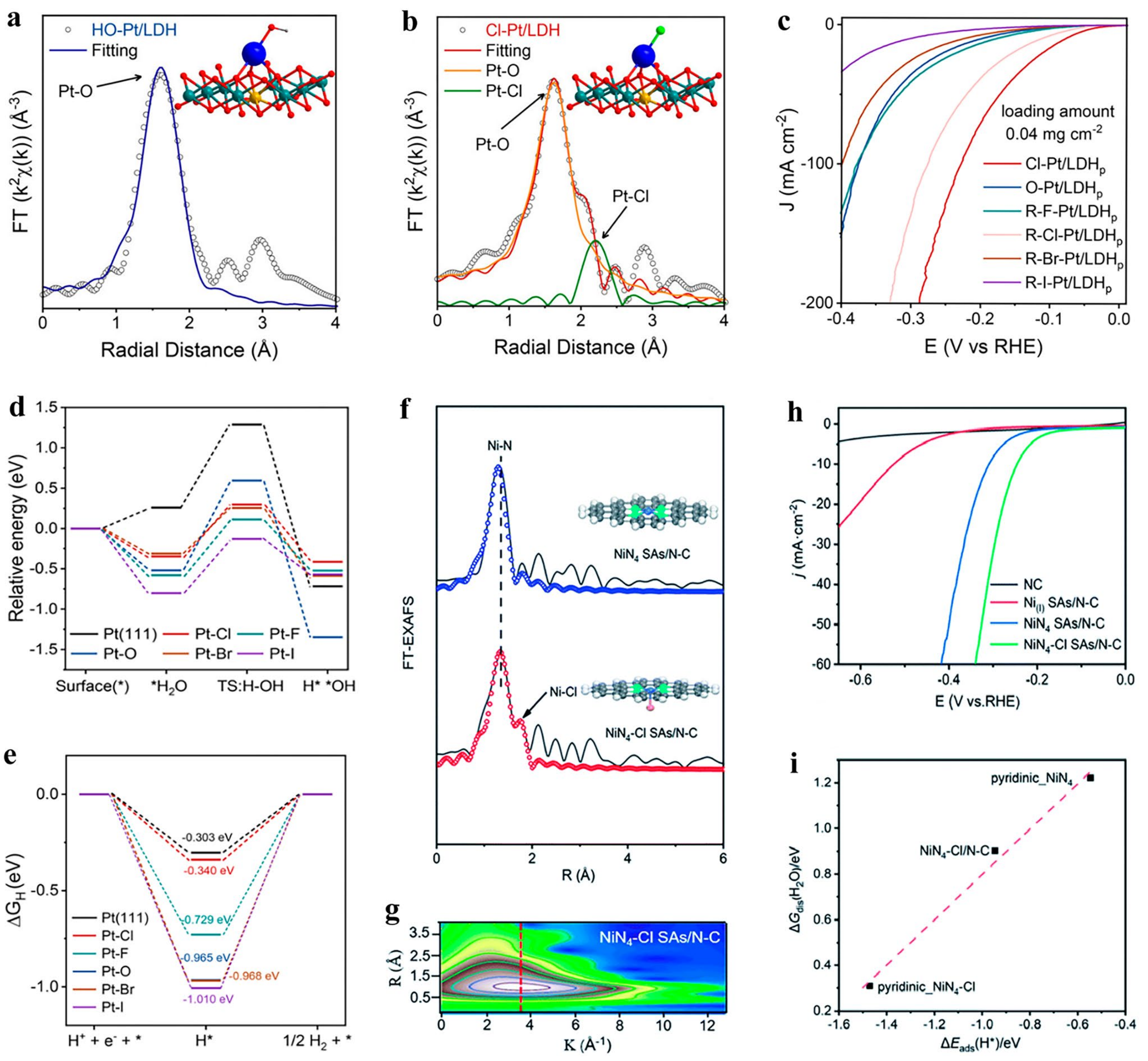

Fig. 12 EXAFS fitting curve (inset is the magnified local structure) of **a** Cl–Pt/LDH and **b** HO–Pt/LDH, the blue, olive, yellow, red, green, and gray spheres refer to Pt, Ni, Fe, O, Cl, and H atoms, respectively. **c** HER polarization curves of the Pt-SACs with different axial ligands. Calculated energy barriers of **d** water dissociation kinetics and **e** adsorption free energies of *H on the surfaces of the Pt-SACs, and the Pt (111) slab as a reference. Reproduced with permission [77]. Copyright: 2022, Springer Nature. **f** R space fitting diagram and theoretical spectra (the greyish-black, dark-green, blue, and orange balls refer to C, N, Ni, and Cl atoms, respectively). **g** Wavelet transform diagram of NiN4–Cl SAs/N–C. **h** HER polarization curves of NC, Ni(I) SAs/N–C, NiN4 SAs/N–C, and NiN4–Cl SAs/ N–C in 1 M KOH. **i** Illustration of the linear correlation between $\Delta G_{dis}(*H_2O)$ and $\Delta E_{ads}(*H)$. Reproduced with permission [189]. Copyright: 2022, Royal Society of Chemistry. (Color figure online)

importance of reasonable design of coordination configuration for improving the HER activity of SACs after determining the ligand atoms.

Apart from Pt-SACs, researchers have also explored axial optimization strategies for Ni-SACs. Li et al. [189] successfully constructed NiN_4–Cl active sites via a doping-adsorption-pyrolysis strategy. R-space EXAFS fitting and wavelet transform jointly demonstrate the presence of an axial Ni–Cl bond at the active site of $NiN_4–Cl_1$, and the change in coordination environment of the central Ni atom

(Fig. 12f, g). The synthesized NiN_4–Cl SAs/N–C catalyst exhibited higher HER activity, lower overpotential, and enhanced long-term stability compared to NiN_4 without axial coordination. To achieve the current density of 10 mA cm^{-2} in alkaline electrolyte, a low overpotential of 243 mV is required for NiN_4–Cl SAs/N–C (Fig. 12h). DFT calculations were applied to explain the role of axial Cl ligands in this catalyst. It indicated that the axial Cl coordination in NiN_4–Cl SAs/NC induces increased electron localization, which facilitates the adsorption and activation of *H intermediates, thereby accelerating the HER process (Fig. 12i).

3.4 Oxygen Evolution Reaction

The electrochemical oxygen evolution reaction (OER) is crucial in various energy conversion and storage devices, such as water electrolysis, metal-air batteries, and fuel cells [30]. The OER involves the conversion of water into oxygen gas and protons, which is a thermodynamically uphill process and requires activation energy to proceed. Its efficiency and performance are essential in determining the overall efficiency and performance of these devices. Therefore, research efforts aimed at improving the efficiency of the OER are crucial in advancing the development of sustainable energy technologies. The reaction mechanisms for OER in both acidic and alkaline solutions are as follows [190]:

In acidic medium:

$$H_2O + * \rightarrow OH_{ads} + H^+ + e^-$$

$$OH_{ads} \rightarrow O_{ads} + H^+ + e^-$$

$$O_{ads} + H_2O \rightarrow OOH_{ads} + H^+ + e^-$$

$$OOH_{ads} \rightarrow O_{2ads} + H^+ + e^-$$

$$O_{2ads} \rightarrow O_2 + *$$

$$2H_2O \rightarrow O_2 + 4H^+ + 4e^- (\text{overall reaction})$$

In alkaline medium:

$$OH^- + * \rightarrow OH_{ads} + e^-$$

$$OH_{ads} + OH^- \rightarrow O_{ads} + H_2O + e^-$$

$$O_{ads} + OH^- \rightarrow OOH_{ads} + e^-$$

$$OOH_{ads} + OH^- \rightarrow O_{2ads} + H_2O + e^-$$

$$O_{2ads} \rightarrow O_2 + *$$

$$4OH^- \rightarrow O_2 + 2H_2O + 4e^- (\text{overall reaction})$$

Generally, OER is plagued by high overpotential and sluggish kinetics, so it is necessary to develop highly active electrocatalysts [191, 192]. Various catalysts have been extensively investigated for their potential in electrocatalytic OER [193–196], wherein SACs are widely employed due to their unique structural characteristics and high efficacy. However, smaller particles tend to aggregate into clusters or particles due to their high surface energy [197]. Therefore, various strategies have been studied to make SACs as dispersed and stable as possible. Among them, axial coordination as a new strategy is gradually coming into view. Deng et al. [198] investigated the 2D transition metal-based tetracyanoquinodimethane (TM-TCNQ, TM = Cr, Cu, Ru, Ag, Pt, Ir) with single atom site structures for OER via DFT calculations. The Fe-TCNQ-Cl and Fe-TCNQ-CO catalysts, which respectively have axial coordination of Cl and CO in Fe-TCNQ material, exhibited higher OER activity and lower overpotential compared to pristine Fe-TCNQ, affirming the potential of axial coordination for improving OER performance. Currently, very few axial coordination designs have been reported as effective strategies for SACs used in OER (Table 3), and there is still significant research potential and promising prospects for further exploration of this strategy. For instance, Zhang et al. [199] incorporated axial O ligand into Co–N_4 single atomic site to form a Co–N_4O_1 configuration on MXene nanosheets (CoN_4–O/MX). The AC HADDF-STEM image of CoN_4–O/MX showed abundant bright isolated spots on the MXene substrate (highlighted with yellow circles), indicating the presence of atomically dispersed Co atoms (Fig. 13a). Additionally, the researchers conducted a least-squares fitting analysis of EXAFS on the catalyst, revealing the coexistence of Co–N and Co–O coordination bonds in CoN_4–O/MX, with respective coordination numbers of 4.0 and 1.0. This finding confirmed the axial regulation of the CoN_4–C active site by the epoxy group on surface of MXene (Fig. 13b). The CoN_4–O/MX catalyst exhibited outstanding OER performance, achieving a potential of 1.55 V at 10 mA cm^{-2} (Fig. 13c). This

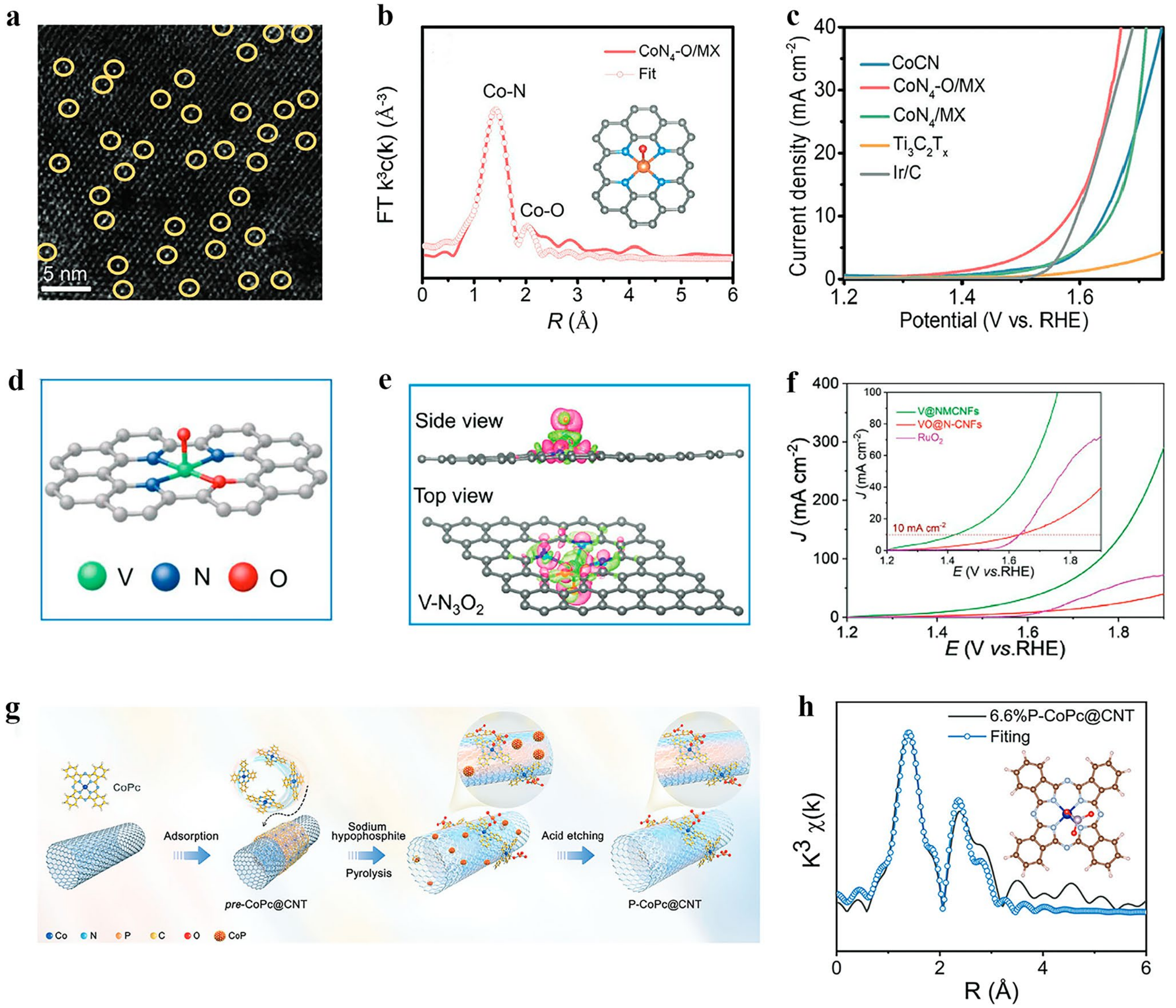

Fig. 13 **a** HADDF-STEM image of CoN$_4$–O/MX. **b** The EXAFS fitting curve in R-space for CoN$_4$–O/MX. **c** LSV curve of CoN$_4$–O/MX for OER. Reproduced with permission [199]. Copyright: 2022, Wiley-VCH GmbH. **d** Schematic atomic structure model of the proposed V–N$_3$O$_2$ configuration. **e** Differential charge density distributions for V–N$_3$O$_2$ (pink and light green colors represent charge accumulation and depletion, respectively). **f** LSV polarization curves of V@NMCNFs with other reported electrocatalysts. Reproduced with permission [200]. Copyright: 2022, Wiley-VCH GmbH. **g** Schematic illustration for the synthesis of 6.6%P-CoPc@CNT. **h** The corresponding EXAFS fitting curve of 6.6%P-CoPc@CNT in R space. Inset: Schematic model of 6.6%P-CoPc@CNT (C: brown, N: gray, Co: blue, P: mauve, O: red). Reproduced with permission [201]. Copyright: 2022, Wiley-VCH GmbH. (Color figure online)

surpasses the performance of other catalysts and highlights the positive impact of axial O regulation on enhancing OER activity. Similarly, Li et al. [200] successfully constructed atomically dispersed V sites with O axial coordination on N-doped multi-channel carbon nanofibers support (V@NMCNFs). Based on both experimental and theoretical calculations, it was proposed that the configuration of central V atom in V@NMCNFs is a five-coordinated V-N$_3$O$_2$ moiety with axial O atom coordination (Fig. 13d). The analysis of charge density difference revealed significant charge accumulation on the V atom of the V-N$_3$O$_2$ moiety, leading to charge depletion on adjacent carbon substrates, thereby improving the charge transfer ability and conductivity of the V-N$_3$O$_2$ moiety (Fig. 13e). The V@NMCNFs catalyst demonstrated superior OER activity compared to the reference samples (VO@N-CNFs and commercial RuO$_2$ benchmark), exhibiting the highest OER activity with the lowest overpotential and largest current response (Fig. 13f). This makes it one of the most competitive OER electrocatalysts among non-noble metals reported to date.

In addition to O ligands, other ligands have also been excavated to be axially coordinated with SACs to improve their OER electrocatalytic activity. Liu et al. [201] achieved axial PO_4 coordination at the Co_1N_4 site of cobalt phthalocyanine adsorbed on carbon nanotubes (P-CoPc@CNT) to enhance OER activity. They synthesized the P-CoPc@CNT catalyst by mixing CoPc@CNT with excess sodium hypophosphite (NaH_2PO_2) followed by pyrolysis and acid etching (Fig. 13g). The EXAFS spectrum of 6.6% P-CoPc@CNT was analyzed in R space, and the bond lengths corresponding to the two characteristic peaks were 1.92 and 2.49 Å (phase shift correction), respectively (Fig. 13h). The bond lengths are consistent with the planar Co–N and axial Co–O bond present in the CoPc-PO_4 model, providing further evidence for the axial coordination structure of 6.6% P-CoPc@CNT. The 6.6% P-CoPc@CNT catalyst with tailored axial PO_4 group exhibited excellent OER performance, with a low overvoltage of 300 mV and a Tafel slope of 41.7 mV dec^{-1}, which is significantly superior to the CoPc@CNT without axial PO_4 coordination. Apart from experimental approaches, DFT calculations had also been utilized to study the impact of axial PO_4 ligands on OER performance. The results revealed that after coordinating axial PO_4 ligands, the adsorption strength of reaction intermediates on central Co sites can be optimized, thereby improving the OER activity of the catalyst.

3.5 Nitrogen/Nitrate Reduction Reaction

Axial coordination design of SACs has also been applied to other electrochemical reactions, such as NO_3^- reduction reactions (NO_3RR) and electrochemical nitrogen reduction reaction (NRR) [202]. The electrocatalytic activity of Fe–N_4–C catalysts for NO_3RR was investigated through DFT calculations, focusing on the impact of various ligands axially coordinated at the central Fe atoms [203]. It has been found that the axial coordination of ligand X (X = O, OH, F, Cl, Br, I) to the Fe center of Fe–N_4–C can significantly improve its catalytic activity in electrocatalytic reduction of NO_3^- to NH_3. Simultaneously, further investigation of the mechanism underlying its remarkable NO_3RR activity confirmed that the significant catalytic activity is attributed to the orbital hybridization of Fe^{3dxz}/Fe^{3dyz} and $NO^{\pi*}$, and a moderate *NO adsorption free energy (ΔG_{*NO}). In addition, when preparing a series of single-atom Fe/NC electrocatalysts through pyrolysis at different temperatures, Liu et al. [204] found that the active site of Fe_1/NC-800 catalyst is OH axially coordinated Fe–N_4 (a square-based cone with OH at the top). The axial coordination of OH disrupts the electronic balance of the FeN_4 active site, thereby improving its NO_3RR electrocatalytic performance to some extent. However, its NO_3RR electrocatalytic activity does not exceed that of Fe_1/NC-900 with an Fe–N_3 triangular cone configuration, which showed excellent NO_3RR performance with a FE of 86.7% and a yield rate of 18.8 mg_{NH3} h^{-1} $mg_{cat}{}^{-1}$. Although the attempt has been made on axial coordination design to enhance the electrocatalytic performance of SACs for NO_3RR, it is evident that challenges remain in this field, and further exploration and efforts are required by researchers. Wu et al. [205] designed Co-SAs/N–C with a sixfold coordination structure by a tandem non-thermal plasma-electrocatalysis strategy, which achieved efficient N_2 fixation to NH_3 in NRR. The best-fit analysis of EXAFS data in R-space and k-space suggested four planar Co–N and two axial Co–O bonds in the first coordination shell of Co-SAs/N–C. DFT calculation results confirmed the superior impact of the axial coordination structure of the catalyst on *NH_3 desorption and *H adsorption, providing compelling evidence for its exceptional catalytic performance. Although the axial coordination design of SACs in N-cycling electrocatalysis is largely unexplored, these endeavors hold significant reference value for enlightening the synthesis of high-value compounds through the utilization of other small molecules (e.g., NO, CO, CO_2, CH_4…).

4 Summary and Perspectives

We herein present a comprehensive review of the latest advances in the development of axial coordination design of SACs, covering their synthetic strategies to energy electrocatalysis applications. In this review, the efficient axial coordination synthetic strategies of SACs have been categorized and summarized, and their electrocatalytic performance as well as reaction mechanisms toward different electrochemical reactions have been overviewed. The high feasibility and promising potential of the axial coordination strategy of SACs to improve their activity and selectivity in electrocatalysis have been successfully demonstrated. It clearly elucidates the crucial roles played by axial ligands in modulating both the geometric and electronic structures of the metal single sites, endowing breakthroughs of knowledge in electrocatalytic SACs regarding the activity and reaction mechanism. However, considering the diverse couplings between axial ligands and metal single sites in SACs, there is great space for the exploration of axially coordinated SACs library tailored to various catalytic reactions with enhanced activity, selectivity and optimized reaction pathways. Consequently, the understanding of SACs will undoubtedly be further discovered and deepened. Despite significant advances and good prospects, axial coordination design for regulating the electrocatalytic activities and stabilities of SACs is still in its infancy. Therefore, challenges and opportunities exist in this rapidly developing field (Fig. 14).

(1) Although several synthetic methods have been reported for preparing axial ligand modified SACs, it is still a big challenge to achieve precise control of the exotic ligand to be axially coordinated to the single atom sites. Consequently, facile, efficient and generalized routes are expected to be developed to realize elaborate axial coordination design on SACs. Considering the complicated and uncontrolled synthetic processes for SACs, the post-modification on the axial position of a pre-synthesized planar SAC by chemical bonding or electrodeposition could be a promising route for the rational construction of the axially coordinated SACs. Moreover, the exploration of a comprehensive understanding of the principles of axial coordination for the guide of rational design and synthesis of axially coordinated SACs is also essential.

(2) Due to the intricate nature of the local coordination environment of SACs, especially those with high coordination numbers, the exact position of the axial ligand needs to be rigorously scrutinized. So far, reported axial coordination design of SACs is predominantly confirmed by synchrotron XAS study. However, it heavily relies on empirical interpretation and data quality. In addition, in certain cases it is hard to differentiate whether the ligand atom is located in the axial direction or the second coordination sphere. Therefore, meticulous study is necessary to prevent interference from the pseudo-coordination of surrounding atoms in proximity to the single atom sites. And the complementary synchrotron techniques like high-energy-resolution fluorescence-detected XANES (HERFD-XANES) and valence-to-core X-ray emission spectroscopy (V2C XES) are believed to provide a great help.

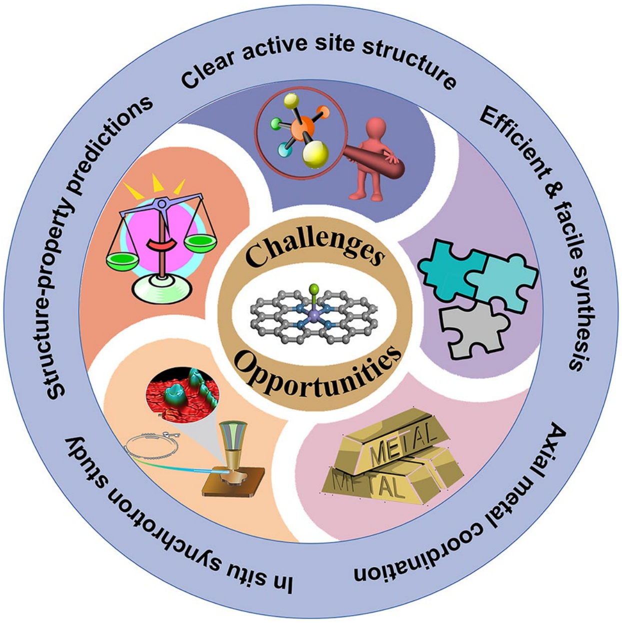

Fig. 14 Illustration of the challenges and opportunities in the future development of axially coordinated singe-atom catalysts

(3) Till now, the majority of axial ligands reported for SACs are restricted to nonmetallic heteroatoms as summarized in this review. Although very few studies on axial coordination by metal atoms has been reported, particularly the metal clusters, the related research is rarely explored. Since there have been already numerous reports on diatomic site catalysts, which generally exhibit higher activity than SACs due to the unique synergy of the adjacent metal atoms. Besides, there is also a rise in study of the concerted catalysis between SACs and metal clusters owing to the activity enhancement. Thereby, the cultivation on diverse axial coordination design of metal clusters to SACs holds great promise in acquiring much improved catalytic performance.

(4) The structural advantages of axial coordination modification of SACs have to be clarified. As shown in this review, axial coordination design is not always a panacea for the performance enhancement. In a few cases, it is not so catalytically active as the typical planar M–N_4 coordination structure. Therefore, a systematic investigation into the structure–property correlation of axially coordinated SACs is necessary, with particular attention paid to parameters such as the types, numbers, sizes and other physicochemical properties of axial ligands. Moreover, the dynamic coordination structural

evolution of axially coordinated SACs during the reaction process remains unexplored and largely overlooked, posing a significant concern in this field. As such, deep insights from the in situ/operando studies during the catalytic process are of significant importance.

(5) Although the feasibility of axial coordination design for SACs has been verified and widely investigated in various energy-conversion related electrochemical reactions, their applications have mostly been limited to ORR and CO_2RR. Therefore, there is significant potential for further exploration of the concept of axial coordination design in SACs for other electrocatalytic reactions, such as hydrogen oxidation reaction (HOR), nitrogen oxide reduction reaction (NORR), C–C/C–N coupling reactions, and even extending to the domains of photocatalysis, thermocatalysis, Li–S batteries and Zn–I_2 batteries, etc. Additionally, further consideration must be given to their industrial applications in fine chemical productions.

Acknowledgements The authors acknowledge financial support from the National Key R&D Program of China (2022YFA1505700), National Natural Science Foundation of China (22205232, 51971157 and 21601187), and Shenzhen Science and Technology Program (JCYJ20210324115412035 and ZDSYS20210813095534001).

Declarations

Conflict of interests The authors declare no interest conflict. They have no known competing financial interests or personal relationships that could have appeared to influence the work reported in this paper.

References

1. A. Slamersak, G. Kallis, D.W. O'Neill, Energy requirements and carbon emissions for a low-carbon energy transition. Nat. Commun. **13**, 6932 (2022). https://doi.org/10.1038/s41467-022-33976-5
2. K. Zhang, W. Guo, Z. Liang, R. Zou, Metal-organic framework based nanomaterials for electrocatalytic oxygen redox reaction. Sci. China Chem. **62**, 417–429 (2019). https://doi.org/10.1007/s11426-018-9441-4
3. G.A. Abdalrb, I. Mircioiu, M. Amzoiu, I. Belu, V. Anuta, Microwave preparation of catalyst layer for enhancing the oxygen reduction of air cathode in microbial fuel cells. Curr. Health Sci. J. **43**, 214–219 (2017). https://doi.org/10.12865/CHSJ.43.03.05
4. T. Matthews, T.A. Mashola, K.A. Adegoke, K. Mugadza, C.T. Fakude et al., Electrocatalytic activity on single atoms catalysts: synthesis strategies, characterization, classification, and energy conversion applications. Coordin. Chem. Rev. **467**, 214600 (2022). https://doi.org/10.1016/j.ccr.2022.214600
5. H. Tian, A. Song, H. Tian, J. Liu, G. Shao et al., Single-atom catalysts for high-energy rechargeable batteries. Chem. Sci. **12**, 7656–7676 (2021). https://doi.org/10.1039/d1sc00716e
6. Y. Zheng, Y. Jiao, Y. Zhu, Q. Cai, A. Vasileff et al., Molecule-level g-C_3N_4 coordinated transition metals as a new class of electrocatalysts for oxygen electrode reactions. J. Am. Chem. Soc. **139**, 3336–3339 (2017). https://doi.org/10.1021/jacs.6b13100
7. L. Xue, Y. Li, X. Liu, Q. Liu, J. Shang et al., Zigzag carbon as efficient and stable oxygen reduction electrocatalyst for proton exchange membrane fuel cells. Nat. Commun. **9**, 3819 (2018). https://doi.org/10.1038/s41467-018-06279-x
8. D. Gao, R.M. Arán-Ais, H.S. Jeon, B. Roldan Cuenya, Rational catalyst and electrolyte design for CO_2 electroreduction towards multicarbon products. Nat. Catal. **2**, 198–210 (2019). https://doi.org/10.1038/s41929-019-0235-5
9. D. Zhao, Z. Chen, W. Yang, S. Liu, X. Zhang et al., MXene (Ti_3C_2) vacancy-confined single-atom catalyst for efficient functionalization of CO_2. J. Am. Chem. Soc. **141**, 4086–4093 (2019). https://doi.org/10.1021/jacs.8b13579
10. X. Zuo, K. Chang, J. Zhao, Z. Xie, H. Tang et al., Bubble-template-assisted synthesis of hollow fullerene-like MoS_2 nanocages as a lithium ion battery anode material. J. Mater. Chem. A **4**, 51–58 (2016). https://doi.org/10.1039/c5ta06869j
11. L.-N. Zhang, Z.-L. Lang, Y.-H. Wang, H.-Q. Tan, H.-Y. Zang et al., Cable-like Ru/WNO@C nanowires for simultaneous high-efficiency hydrogen evolution and low-energy consumption chlor-alkali electrolysis. Energy Environ. Sci. **12**, 2569–2580 (2019). https://doi.org/10.1039/c9ee01647c
12. L. Han, X. Liu, J. Chen, R. Lin, H. Liu et al., Atomically dispersed molybdenum catalysts for efficient ambient nitrogen fixation. Angew. Chem. Int. Ed. **131**, 2343–2347 (2019). https://doi.org/10.1002/ange.201811728
13. L. Han, Z. Ren, P. Ou, H. Cheng, N. Rui et al., Modulating single-atom palladium sites with copper for enhanced ambient ammonia electrosynthesis. Angew. Chem. Int. Ed. **133**, 349–354 (2021). https://doi.org/10.1002/ange.202010159
14. S. Chen, L. Kuo, Z. Jian, L. Qian, L. Xijun et al., In Situ Transmission electron microscopy and three-dimensional electron tomography for catalyst studies. Chin. J. Struct. Chem. **41**, 2210056–2210076 (2022). https://doi.org/10.14102/j.cnki.0254-5861.2022-0187

15. Z. Du, J. Liang, S. Li, Z. Xu, T. Li et al., Alkylthiol surface engineering: an effective strategy toward enhanced electrocatalytic N_2-to-NH_3 fixation by a CoP nanoarray. J. Mater. Chem. A **9**, 13861–13866 (2021). https://doi.org/10.1039/d1ta02424h
16. X. Luo, W. Wu, Y. Wang, Y. Li, J. Ye et al., Relay Catalysis of Multi-Sites Promotes Oxygen Reduction Reaction. Adv. Funct. Mater. **33**, 2215021 (2023). https://doi.org/10.1002/adfm.202215021
17. F.V.E. dos Reis, V.S. Antonin, P. Hammer, M.C. Santos, P.H.C. Camargo, Carbon-supported TiO_2–Au hybrids as catalysts for the electrogeneration of hydrogen peroxide: investigating the effect of TiO_2 shape. J. Catal. **326**, 100–106 (2015). https://doi.org/10.1016/j.jcat.2015.04.007
18. Y. Guo, R. Zhang, S. Zhang, H. Hong, Y. Zhao et al., Ultrahigh oxygen-doped carbon quantum dots for highly efficient H_2O_2 production via two-electron electrochemical oxygen reduction. Energy Environ. Sci. **15**, 4167–4174 (2022). https://doi.org/10.1039/d2ee01797k
19. R. Ma, J. Wang, Y. Tang, J. Wang, Design strategies for single-atom iron electrocatalysts toward efficient oxygen reduction. J. Phys. Chem. Lett. **13**, 168–174 (2021). https://doi.org/10.1021/acs.jpclett.1c03753
20. S. Xu, R. Lu, K. Sun, J. Tang, Y. Cen et al., Synergistic effects in N, O-comodified carbon nanotubes boost highly selective electrochemical oxygen reduction to H_2O_2. Adv. Sci. **9**, 2201421 (2022). https://doi.org/10.1002/advs.202201421
21. F. An, X.-Q. Bao, X.-Y. Deng, Z.-Z. Ma, X.-G. Wang, Carbon-based metal-free oxygen reduction reaction electrocatalysts: past, present and future. New Carbon Mater. **37**, 338–354 (2022). https://doi.org/10.1016/s1872-5805(22)60590-0
22. B. Qiao, A. Wang, X. Yang, L.F. Allard, Z. Jiang et al., Single-atom catalysis of CO oxidation using Pt_1/FeO_x. Nat. Chem. **3**, 634–641 (2011). https://doi.org/10.1038/nchem.1095
23. Z. Lin, Q. Zhang, J. Pan, C. Tsounis, A.A. Esmailpour et al., Atomic Co decorated free-standing graphene electrode assembly for efficient hydrogen peroxide production in acid. Energy Environ. Sci. **15**, 1172–1182 (2022). https://doi.org/10.1039/d1ee02884g
24. W.J. Niu, J.Z. He, B.N. Gu, M.C. Liu, Y.L. Chueh, Opportunities and challenges in precise synthesis of transition metal single-atom supported by 2D Materials as catalysts toward oxygen reduction reaction. Adv. Funct. Mater. **31**, 2103558 (2021). https://doi.org/10.1002/adfm.202103558
25. X. Wan, X. Liu, Y. Li, R. Yu, L. Zheng et al., Fe–N–C electrocatalyst with dense active sites and efficient mass transport for high-performance proton exchange membrane fuel cells. Nat. Catal. **2**, 259–268 (2019). https://doi.org/10.1038/s41929-019-0237-3
26. L. Han, M. Hou, P. Ou, H. Cheng, Z. Ren et al., Local modulation of single-atomic Mn sites for enhanced ambient ammonia electrosynthesis. ACS Catal. **11**, 509–516 (2020). https://doi.org/10.1021/acscatal.0c04102
27. L. Han, S. Song, M. Liu, S. Yao, Z. Liang et al., Stable and efficient single-atom Zn catalyst for CO_2 reduction to CH_4. J. Am. Chem. Soc. **142**, 12563–12567 (2020). https://doi.org/10.1021/jacs.9b12111
28. W. Liu, H. Li, P. Ou, J. Mao, L. Han et al., Isolated Cu-Sn diatomic sites for enhanced electroreduction of CO_2 to CO. Nano Res. (2023). https://doi.org/10.1007/s12274-023-5513-5
29. M.B. Gawande, K. Ariga, Y. Yamauchi, Single-atom catalysts. Small **17**, 2101584 (2021). https://doi.org/10.1002/smll.202101584
30. H. Chen, X. Liang, Y. Liu, X. Ai, T. Asefa et al., Active site engineering in porous electrocatalysts. Adv. Mater. **32**, 2002435 (2020). https://doi.org/10.1002/adma.202002435
31. A. Kumar, G. Yasin, S. Ajmal, S. Ali, M.A. Mushtaq et al., Molecular MnN_4-complex immobilized on carbon black as efficient electrocatalyst for oxygen reduction reaction. Inter. J. Hydrogen Energy **47**, 17621–17629 (2022). https://doi.org/10.1016/j.ijhydene.2022.03.243
32. S. Chen, T. Luo, X. Li, K. Chen, J. Fu et al., Identification of the highly active $Co\text{-}N_4$ coordination motif for selective oxygen reduction to hydrogen peroxide. J. Am. Chem. Soc. **144**, 14505–14516 (2022). https://doi.org/10.1021/jacs.2c01194
33. L. Han, H. Cheng, W. Liu, H. Li, P. Ou et al., A single-atom library for guided monometallic and concentration-complex multimetallic designs. Nat. Mater. **21**, 681–688 (2022). https://doi.org/10.1038/s41563-022-01252-y
34. L. Gao, X. Gao, P. Jiang, C. Zhang, H. Guo et al., Atomically dispersed iron with densely exposed active sites as bifunctional oxygen catalysts for zinc-air flow batteries. Small **18**, 2105892 (2022). https://doi.org/10.1002/smll.202105892
35. L. Han, X. Liu, J. He, Z. Liang, H.T. Wang et al., Modification of the coordination environment of active sites on MoC for high-efficiency CH_4 production. Adv. Energy Mater. **11**, 2100044 (2021). https://doi.org/10.1002/aenm.202100044
36. L. Liang, K.-Y. Niu, L. Zhang, J. Tian, K. Zhou et al., Engineering oxygen vacancies in mesocrystalline CuO nanosheets for water oxidation. ACS Appl. Nano Mater. **4**, 6135–6144 (2021). https://doi.org/10.1021/acsanm.1c00941
37. L. Zhang, X. Wang, R. Wang, M. Hong, Structural evolution from metal–organic framework to hybrids of nitrogen-doped porous carbon and carbon nanotubes for enhanced oxygen reduction activity. Chem. Mater. **27**, 7610–7618 (2015). https://doi.org/10.1021/acs.chemmater.5b02708
38. M. Wang, H. Zhang, Y. Liu, Y. Pan, Research progress of precise structural regulation of single atom catalyst for accelerating electrocatalytic oxygen reduction reaction. J. Energy Chem. **72**, 56–72 (2022). https://doi.org/10.1016/j.jechem.2022.05.007
39. J. Guo, Y. Zheng, Z. Hu, C. Zheng, J. Mao et al., Direct seawater electrolysis by adjusting the local reaction environment of a catalyst. Nat. Energy **8**, 264–272 (2023). https://doi.org/10.1038/s41560-023-01195-x
40. K. Du, L. Zhang, J. Shan, J. Guo, J. Mao et al., Interface engineering breaks both stability and activity limits of ruo2 for sustainable water oxidation. Nat. Commun. **13**, 5448 (2022). https://doi.org/10.1038/s41467-022-33150-x

41. Y. Yang, K. Mao, S. Gao, H. Huang, G. Xia et al., O-, N-atoms-coordinated Mn cofactors within a graphene framework as bioinspired oxygen reduction reaction electrocatalysts. Adv. Mater. **30**, 1801732 (2018). https://doi.org/10.1002/adma.201801732
42. Y. Chen, R. Gao, S. Ji, H. Li, K. Tang et al., Atomic-level modulation of electronic density at cobalt single-atom sites derived from metal-organic frameworks: enhanced oxygen reduction performance. Angew. Chem. Int. Ed. **60**, 3212–3221 (2021). https://doi.org/10.1002/anie.202012798
43. X. Wang, Z. Chen, X. Zhao, T. Yao, W. Chen et al., Regulation of coordination number over single Co sites: triggering the efficient electroreduction of CO_2. Angew. Chem. Int. Ed. **57**, 1944–1948 (2018). https://doi.org/10.1002/anie.201712451
44. Y. Xu, W. Zhang, Y. Li, P. Lu, Z.-S. Wu, A general bimetal-ion adsorption strategy to prepare nickel single atom catalysts anchored on graphene for efficient oxygen evolution reaction. J. Energy Chem. **43**, 52–57 (2020). https://doi.org/10.1016/j.jechem.2019.08.006
45. Y. Hou, M. Qiu, M.G. Kim, P. Liu, G. Nam et al., Atomically dispersed nickel-nitrogen-sulfur species anchored on porous carbon nanosheets for efficient water oxidation. Nat. Commun. **10**, 1392 (2019). https://doi.org/10.1038/s41467-019-09394-5
46. X. Tao, R. Lu, L. Ni, V. Gridin, S.H. Al-Hilfi et al., Facilitating the acidic oxygen reduction of Fe–N–C catalysts by fluorine-doping. Mater. Horiz. **9**, 417–424 (2022). https://doi.org/10.1039/d1mh01307f
47. W. Xu, W. Song, Y. Kang, L. Jiao, Y. Wu et al., Axial ligand-engineered single-atom catalysts with boosted enzyme-like activity for sensitive immunoassay. Anal. Chem. **93**, 12758–12766 (2021). https://doi.org/10.1021/acs.analchem.1c02842
48. H.C. Zhang, P.X. Cui, D.H. Xie, Y.J. Wang, P. Wang et al., Axial N ligand-modulated ultrahigh activity and selectivity hyperoxide activation over single-atoms nanozymes. Adv. Sci. **10**, e2205681 (2023). https://doi.org/10.1002/advs.202205681
49. T. Chen, D. Zhou, S. Hou, Y. Li, Y. Liu et al., Designing hierarchically porous single atoms of Fe-N_5 catalytic sites with high oxidase-like activity for sensitive detection of organophosphorus pesticides. Anal. Chem. **94**, 15270–15279 (2022). https://doi.org/10.1021/acs.analchem.2c02540
50. H. Zhang, L. Huang, J. Chen, L. Liu, X. Zhu et al., Bionic design of cytochrome C oxidase-like single-atom nanozymes for oxygen reduction reaction in enzymatic biofuel cells. Nano Energy **83**, 105798 (2021). https://doi.org/10.1016/j.nanoen.2021.105798
51. C. Xu, Y.P. Zhang, T.L. Zheng, Z.Q. Wang, Y.M. Zhao et al., Contracted Fe-N_5-C_{11} sites in single-atom catalysts boosting catalytic performance for oxygen reduction reaction. ACS Appl. Mater. Interfaces **15**, 32341–32351 (2023). https://doi.org/10.1021/acsami.3c03982
52. Y.M. Zhao, P.C. Zhang, C. Xu, X.Y. Zhou, L.M. Liao et al., Design and preparation of Fe-N_5 catalytic sites in single-atom catalysts for enhancing the oxygen reduction reaction in fuel cells. ACS Appl. Mater. Interfaces **12**, 17334–17342 (2020). https://doi.org/10.1021/acsami.9b20711
53. F.X. Ma, Z.Q. Liu, G. Zhang, H.S. Fan, Y. Du et al., Self-sacrificing template synthesis of carbon nanosheets assembled hollow spheres with abundant active Fe-N_4O_1 moieties for electrocatalytic oxygen reduction. Small **19**, 2207991 (2023). https://doi.org/10.1002/smll.202207991
54. T. Liu, Y. Wang, Y. Li, Two-dimensional organometallic frameworks with pyridinic single-metal-atom sites for bifunctional ORR/OER. Adv. Funct. Mater. **32**, 2207110 (2022). https://doi.org/10.1002/adfm.202207110
55. X. Liu, Y. Liu, W. Yang, X. Feng, B. Wang, Controlled Modification of axial coordination for transition-metal single-atom electrocatalyst. Chem **28**, e202201471 (2022). https://doi.org/10.1002/chem.202201471
56. A. Pizarro, G. Abarca, C. Gutiérrez-Cerón, D. Cortés-Arriagada, F. Bernardi et al., Building pyridinium molecular wires as axial ligands for tuning the electrocatalytic activity of iron phthalocyanines for the oxygen reduction reaction. ACS Catal. **8**, 8406–8419 (2018). https://doi.org/10.1021/acscatal.8b01479
57. B. Ji, J. Gou, Y. Zheng, X. Pu, Y. Wang et al., Coordination chemistry of large-sized yttrium single-atom catalysts for oxygen reduction reaction. Adv. Mater. **35**, e2300381 (2023). https://doi.org/10.1002/adma.202300381
58. J. Xi, H.S. Jung, Y. Xu, F. Xiao, J.W. Bae et al., Synthesis strategies, catalytic applications, and performance regulation of single-atom catalysts. Adv. Funct. Mater. **31**, 2008318 (2021). https://doi.org/10.1002/adfm.202008318
59. F. Xiao, G.-L. Xu, C.-J. Sun, M. Xu, W. Wen et al., Nitrogen-coordinated single iron atom catalysts derived from metal organic frameworks for oxygen reduction reaction. Nano Energy **61**, 60–68 (2019). https://doi.org/10.1016/j.nanoen.2019.04.033
60. X. Wang, Y. Wang, X. Sang, W. Zheng, S. Zhang et al., Dynamic activation of adsorbed intermediates via axial traction for the promoted electrochemical CO_2 reduction. Angew. Chem. Int. Ed. **60**, 4192–4198 (2021). https://doi.org/10.1002/anie.202013427
61. L. Peng, J. Yang, Y. Yang, F. Qian, Q. Wang et al., Mesopore-rich Fe–N–C catalyst with FeN_4–O–NC single-atom sites delivers remarkable oxygen reduction reaction performance in alkaline media. Adv. Mater. **34**, 2202544 (2022). https://doi.org/10.1002/adma.202202544
62. C. Xu, Y. Si, B. Hu, X. Xu, B. Hu et al., Promoting oxygen reduction via crafting bridge-bonded oxygen ligands on a single-atom iron catalyst. Inorg. Chem. Front **9**, 3306–3318 (2022). https://doi.org/10.1039/d2qi00668e
63. F. Luo, A. Roy, L. Silvioli, D.A. Cullen, A. Zitolo et al., P-block single-metal-site tin/nitrogen-doped carbon fuel cell cathode catalyst for oxygen reduction reaction. Nat. Mater. **19**, 1215–1223 (2020). https://doi.org/10.1038/s41563-020-0717-5
64. L. Hu, C. Dai, L. Chen, Y. Zhu, Y. Hao et al., Metal-triazolate-framework-derived FeN_4Cl_1 single-atom catalysts

with hierarchical porosity for the oxygen reduction reaction. Angew. Chem. Int. Ed. **60**, 27324–27329 (2021). https://doi.org/10.1002/anie.202113895

65. J. Huang, Q. Lu, X. Ma, X. Yang, Bio-inspired FeN_5 moieties anchored on a three-dimensional graphene aerogel to improve oxygen reduction catalytic performance. J. Mater. Chem. A **6**, 18488–18497 (2018). https://doi.org/10.1039/c8ta06455e
66. G. Qu, K. Wei, K. Pan, J. Qin, J. Lv et al., Emerging materials for electrochemical CO_2 reduction: progress and optimization strategies of carbon-based single-atom catalysts. Nanoscale **15**, 3666–3692 (2023). https://doi.org/10.1039/d2nr06190b
67. Y. Zhao, P.V. Kumar, X. Tan, X. Lu, X. Zhu et al., Modulating Pt-O-Pt atomic clusters with isolated cobalt atoms for enhanced hydrogen evolution catalysis. Nat. Commun. **13**, 2430 (2022). https://doi.org/10.1038/s41467-022-30155-4
68. Y. Dai, B. Liu, Z. Zhang, P. Guo, C. Liu et al., Tailoring the d-orbital splitting manner of single atomic sites for enhanced oxygen reduction. Adv. Mater. **35**, 2210757 (2023). https://doi.org/10.1002/adma.202210757
69. J. Guo, X. Yan, Q. Liu, Q. Li, X. Xu et al., The synthesis and synergistic catalysis of iron phthalocyanine and its graphene-based axial complex for enhanced oxygen reduction. Nano Energy **46**, 347–355 (2018). https://doi.org/10.1016/j.nanoen.2018.02.026
70. Y. Mu, T. Wang, J. Zhang, C. Meng, Y. Zhang et al., Single-atom catalysts: Advances and challenges in metal-support interactions for enhanced electrocatalysis. Electrochem. Energy Rev. **5**, 145–186 (2022). https://doi.org/10.1007/s41918-021-00124-4
71. B. Yang, X. Li, Q. Cheng, X. Jia, Y. Liu et al., A highly efficient axial coordinated CoN_5 electrocatalyst via pyrolysis-free strategy for alkaline polymer electrolyte fuel cells. Nano Energy **101**, 107565 (2022). https://doi.org/10.1016/j.nanoen.2022.107565
72. J. Riquelme, K. Neira, J.F. Marco, P. Hermosilla-Ibáñez, W. Orellana et al., Biomimicking vitamin B12. A Co phthalocyanine pyridine axial ligand coordinated catalyst for the oxygen reduction reaction. Electrochim. Acta **265**, 547–555 (2018). https://doi.org/10.1016/j.electacta.2018.01.177
73. W. Fan, Z. Duan, W. Liu, R. Mehmood, J. Qu et al., Rational design of heterogenized molecular phthalocyanine hybrid single-atom electrocatalyst towards two-electron oxygen reduction. Nat. Commun. **14**, 1426 (2023). https://doi.org/10.1038/s41467-023-37066-y
74. Z. Zhang, C. Feng, C. Liu, M. Zuo, L. Qin et al., Electrochemical deposition as a universal route for fabricating single-atom catalysts. Nat. Commun. **11**, 1215 (2020). https://doi.org/10.1038/s41467-020-14917-6
75. J. Guo, H. Liu, D. Li, J. Wang, X. Djitcheu et al., A minireview on the synthesis of single atom catalysts. RSC Adv. **12**, 9373–9394 (2022). https://doi.org/10.1039/d2ra00657j
76. F.X. Hu, T. Hu, S. Chen, D. Wang, Q. Rao et al., Single-atom cobalt-based electrochemical biomimetic uric acid sensor with wide linear range and ultralow detection limit. Nano-Micro Lett. **13**, 7 (2020). https://doi.org/10.1007/s40820-020-00536-9
77. T. Zhang, J. Jin, J. Chen, Y. Fang, X. Han et al., Pinpointing the axial ligand effect on platinum single-atom-catalyst towards efficient alkaline hydrogen evolution reaction. Nat. Commun. **13**, 6875 (2022). https://doi.org/10.1038/s41467-022-34619-5
78. L. Li, Y. Wen, G. Han, F. Kong, L. Du et al., Architecting FeN_x on high graphitization carbon for high-performance oxygen reduction by regulating *d-band* center. Small **19**, e2300758 (2023). https://doi.org/10.1002/smll.202300758
79. W. Li, Z. Guo, J. Yang, Y. Li, X. Sun et al., Advanced strategies for stabilizing single-atom catalysts for energy storage and conversion. Electrochem. Energy Rev. **5**, 9 (2022). https://doi.org/10.1007/s41918-022-00169-z
80. Y. Wang, J. Hao, Y. Liu, M. Liu, K. Sheng et al., Recent advances in regulating the performance of acid oxygen reduction reaction on carbon-supported non-precious metal single atom catalysts. J. Energy Chem. **76**, 601–616 (2023). https://doi.org/10.1016/j.jechem.2022.09.047
81. H. Jin, Z. Xu, Z.Y. Hu, Z. Yin, Z. Wang et al., Mesoporous Pt@Pt-skin Pt_3Ni core-shell framework nanowire electrocatalyst for efficient oxygen reduction. Nat. Commun. **14**, 1518 (2023). https://doi.org/10.1038/s41467-023-37268-4
82. W. Liu, L. Han, H.-T. Wang, X. Zhao, J.A. Boscoboinik et al., FeMo sub-nanoclusters/single atoms for neutral ammonia electrosynthesis. Nano Energy **77**, 105078 (2020). https://doi.org/10.1016/j.nanoen.2020.105078
83. X. Peng, R. Zhang, Y. Mi, H.T. Wang, Y.C. Huang et al., Disordered Au nanoclusters for efficient ammonia electrosynthesis. Chem. Sus. Chem. (2023). https://doi.org/10.1002/cssc.202201385
84. L. Chai, L. Zhang, X. Wang, L. Xu, C. Han et al., Bottom-up synthesis of MOF-derived hollow N-doped carbon materials for enhanced ORR performance. Carbon **146**, 248–256 (2019). https://doi.org/10.1016/j.carbon.2019.02.006
85. S. Sarkar, S.C. Peter, An overview on Pt_3X Electrocatalysts for oxygen reduction reaction. Chem. Asian J. **16**, 1184–1197 (2021). https://doi.org/10.1002/asia.202100166
86. W. Zhu, S. Chen, Recent progress of single-atom catalysts in the electrocatalytic reduction of oxygen to hydrogen peroxide. Electroanalysis **32**, 2591–2602 (2020). https://doi.org/10.1002/elan.202060334
87. N. Wang, S. Ma, P. Zuo, J. Duan, B. Hou, Recent progress of electrochemical production of hydrogen peroxide by two-electron oxygen reduction reaction. Adv. Sci. **8**, 2100076 (2021). https://doi.org/10.1002/advs.202100076
88. D.-W. Wang, D. Su, Heterogeneous nanocarbon materials for oxygen reduction reaction. Energy Environ. Sci. **7**, 576–591 (2014). https://doi.org/10.1039/c3ee43463j
89. X. Yang, C. Priest, Y. Hou, G. Wu, Atomically dispersed dual-metal-site PGM-free electrocatalysts for oxygen reduction reaction: opportunities and challenges. Sus. Mat. **2**, 569–590 (2022). https://doi.org/10.1002/sus2.69

90. L. Zhang, T. Gu, K. Lu, L. Zhou, D.S. Li et al., Engineering synergistic edge-N dipole in metal-free carbon nanoflakes toward intensified oxygen reduction electrocatalysis. Adv. Funct. Mater. **31**, 2103187 (2021). https://doi.org/10.1002/adfm.202103187
91. L. Zhang, Z. Su, F. Jiang, L. Yang, J. Qian et al., Highly graphitized nitrogen-doped porous carbon nanopolyhedra derived from ZIF-8 nanocrystals as efficient electrocatalysts for oxygen reduction reactions. Nanoscale **6**, 6590–6602 (2014). https://doi.org/10.1039/C4NR00348A
92. S. Yuan, J. Zhang, L. Hu, J. Li, S. Li et al., Decarboxylation-induced defects in MOF-derived single cobalt atom@carbon electrocatalysts for efficient oxygen reduction. Angew. Chem. Int. Ed. **60**, 21685–21690 (2021). https://doi.org/10.1002/anie.202107053
93. J. Zhang, M. Zhang, Y. Zeng, J. Chen, L. Qiu et al., Single Fe atom on hierarchically porous S, N-codoped nanocarbon derived from porphyra enable boosted oxygen catalysis for rechargeable zn-air batteries. Small (2019). https://doi.org/10.1002/smll.201900307
94. N. Agarwal, S.J. Freakley, R.U. McVicker, S.M. Althahban et al., Aqueous Au–Pd colloids catalyze selective CH_4 oxidation to CH_3OH with O_2 under mild conditions. Science **358**, 223–227 (2017). https://doi.org/10.1126/science.aan6515
95. Y. Zhang, Q. Chen, A. Guo, X. Wang, Y. Wang et al., Carbon-nanosheet-driven spontaneous deposition of Au nanoparticles for efficient electrochemical utilizations toward H_2O_2 generation and detection. Chem. Eng. J. **445**, 136586 (2022). https://doi.org/10.1016/j.cej.2022.136586
96. Y.R. Zheng, S. Hu, X.L. Zhang, H. Ju, Z. Wang et al., Black phosphorous mediates surface charge redistribution of $CoSe_2$ for electrochemical H_2O_2 production in acidic electrolytes. Adv. Mater. **34**, 2205414 (2022). https://doi.org/10.1002/adma.202205414
97. Y. Xia, X. Zhao, C. Xia, Z.Y. Wu, P. Zhu et al., Highly active and selective oxygen reduction to H_2O_2 on boron-doped carbon for high production rates. Nat. Commun. **12**, 4225 (2021). https://doi.org/10.1038/s41467-021-24329-9
98. S. Yang, A. Verdaguer-Casadevall, L. Arnarson, L. Silvioli, V. Čolić et al., Toward the decentralized electrochemical production of H_2O_2: a focus on the catalysis. ACS Catal. **8**, 4064–4081 (2018). https://doi.org/10.1021/acscatal.8b00217
99. J. Gao, B. Liu, Progress of electrochemical hydrogen peroxide synthesis over single atom catalysts. ACS Mater. Lett. **2**, 1008–1024 (2020). https://doi.org/10.1021/acsmaterialslett.0c00189
100. A.R. Payne, Hysteresis of rubbers loaded with carbon black. Nature **201**, 1213–1214 (1964). https://doi.org/10.1038/2011213a0
101. J. Barrio, A. Pedersen, S.C. Sarma, A. Bagger, M. Gong et al., FeNC oxygen reduction electrocatalyst with high utilization penta-coordinated sites. Adv. Mater. (2023). https://doi.org/10.1002/adma.202211022
102. M.P. Oyarzún, N. Silva, D. Cortés-Arriagada, J.F. Silva, I.O. Ponce et al., Enhancing the electrocatalytic activity of Fe phthalocyanines for the oxygen reduction reaction by the presence of axial ligands: pyridine-functionalized single-walled carbon nanotubes. Electrochim. Acta **398**, 139263 (2021). https://doi.org/10.1016/j.electacta.2021.139263
103. Y. Zhou, Y.F. Xing, J. Wen, H.B. Ma, F.B. Wang et al., Axial ligands tailoring the ORR activity of cobalt porphyrin. Sci. Bull. **64**, 1158–1166 (2019). https://doi.org/10.1016/j.scib.2019.07.003
104. Y. Niu, X. Huang, W. Hu, Fe_3C nanoparticle decorated Fe/N doped graphene for efficient oxygen reduction reaction electrocatalysis. J. Power Sources **332**, 305–311 (2016). https://doi.org/10.1016/j.jpowsour.2016.09.130
105. P.J. Wei, G.Q. Yu, Y. Naruta, J.G. Liu, Covalent grafting of carbon nanotubes with a biomimetic heme model compound to enhance oxygen reduction reactions. Angew. Chem. Int. Ed. **53**, 6659–6663 (2014). https://doi.org/10.1002/anie.201403133
106. L. Yang, Y. Wang, Z. Lu, R. Cheng, N. Wang et al., Construction of multi-dimensional NiCO/C/CNT/rGO aerogel by MOF derivative for efficient microwave absorption. Carbon **205**, 411–421 (2023). https://doi.org/10.1016/j.carbon.2023.01.057
107. G. Panomsuwan, N. Saito, T. Ishizaki, Nitrogen-doped carbon nanoparticle-carbon nanofiber composite as an efficient metal-free cathode catalyst for oxygen reduction reaction. ACS Appl. Mater. Interfaces **8**, 6962–6971 (2016). https://doi.org/10.1021/acsami.5b10493
108. R. Venegas, F.J. Recio, J. Riquelme, K. Neira, J.F. Marco et al., Biomimetic reduction of O_2 in an acid medium on iron phthalocyanines axially coordinated to pyridine anchored on carbon nanotubes. J. Mater. Chem. A **5**, 12054–12059 (2017). https://doi.org/10.1039/c7ta02381b
109. W. Zhang, E.J. Meeus, L. Wang, L.H. Zhang, S. Yang et al., Boosting electrochemical oxygen reduction performance of iron phthalocyanine through axial coordination sphere interaction. ChemSusChem (2022). https://doi.org/10.1002/cssc.202102379
110. R. Cao, R. Thapa, H. Kim, X. Xu, M. Gyu Kim et al., Promotion of oxygen reduction by a bio-inspired tethered iron phthalocyanine carbon nanotube-based catalyst. Nat. Commun. **4**, 2076 (2013). https://doi.org/10.1038/ncomms3076
111. W. Xia, Z. Hou, J. Tang, J. Li, W. Chaikittisilp et al., Materials informatics-guided superior electrocatalyst: a case of pyrolysis-free single-atom coordinated with N-graphene nanomesh. Nano Energy **94**, 106868 (2022). https://doi.org/10.1016/j.nanoen.2021.106868
112. M. Viera, J. Riquelme, C. Aliaga, J.F. Marco, W. Orellana et al., Oxygen reduction reaction at penta-coordinated Co phthalocyanines. Front Chem. **8**, 22 (2020). https://doi.org/10.3389/fchem.2020.00022
113. F. Liu, G. Zhu, D. Yang, D. Jia, F. Jin et al., Systematic exploration of N, C configurational effects on the ORR performance of Fe–N doped graphene catalysts based on DFT calculations. RSC Adv. **9**, 22656–22667 (2019). https://doi.org/10.1039/c9ra02822f
114. F. Liu, N. Yan, G. Zhu, Z. Liu, S. Ma et al., Fe–N–C single-atom catalysts with an axial structure prepared by a new

design and synthesis method for ORR. New J. Chem. **45**, 13004–13014 (2021). https://doi.org/10.1039/d1nj01380g

115. Y. Lin, P. Liu, E. Velasco, G. Yao, Z. Tian et al., Fabricating single-atom catalysts from chelating metal in open frameworks. Adv. Mater. **31**, 1808193 (2019). https://doi.org/10.1002/adma.201808193
116. L. Li, Y.-J. Chen, H.-R. Xing, N. Li, J.-W. Xia et al., Single-atom Fe-N_5 catalyst for high-performance zinc-air batteries. Nano Res. **15**, 8056–8064 (2022). https://doi.org/10.1007/s12274-022-4424-1
117. Y. Qin, C. Guo, Z. Ou, C. Xu, Q. Lan et al., Regulating single-atom Mn sites by precisely axial pyridinic-nitrogen coordination to stabilize the oxygen reduction. J. Energy Chem. **80**, 542–552 (2023). https://doi.org/10.1016/j.jechem.2023.01.048
118. Q. Wang, G. Long, X. Gao, J. Chen, C. You et al., A highly active and stable single-atom catalyst for oxygen reduction with axial Fe–O coordination prepared through a fast medium-temperature pyrolysis process. Appl. Catal. B: Environ. **337**, 123009 (2023). https://doi.org/10.1016/j.apcatb.2023.123009
119. F. Kraushofer, G.S. Parkinson, Single-atom catalysis: Insights from model systems. Chem. Rev. **122**, 14911–14939 (2022). https://doi.org/10.1021/acs.chemrev.2c00259
120. X. Wang, Y. An, L. Liu, L. Fang, Y. Liu et al., Atomically dispersed pentacoordinated-zirconium catalyst with axial oxygen ligand for oxygen reduction reaction. Angew. Chem. Int. Ed. **61**, e202209746 (2022). https://doi.org/10.1002/anie.202209746
121. S. Zhang, Q. Zhou, L. Fang, R. Wang, T. Lu et al., Gram-scale synthesis and unraveling the activity origin of atomically dispersed Co-N_4O sites toward superior electrocatalytic oxygen reduction. Appl. Catal. B: Environ. **328**, 122489 (2023). https://doi.org/10.1016/j.apcatb.2023.122489
122. L. Cheng, H. Huang, Z. Lin, Y. Yang, Q. Yuan et al., N and O multi-coordinated vanadium single atom with enhanced oxygen reduction activity. J. Colloid Interface Sci. **594**, 466–473 (2021). https://doi.org/10.1016/j.jcis.2021.03.074
123. Y. Liu, X. Liu, Z. Lv, R. Liu, L. Li et al., Tuning the spin state of the iron Center by bridge-bonded Fe-O-Ti ligands for enhanced oxygen reduction. Angew. Chem. Int. Ed. (2022). https://doi.org/10.1002/anie.202117617
124. K. Chen, K. Liu, P. An, H. Li, Y. Lin et al., Iron phthalocyanine with coordination induced electronic localization to boost oxygen reduction reaction. Nat. Commun. **11**, 4173 (2020). https://doi.org/10.1038/s41467-020-18062-y
125. P. Cao, X. Quan, X. Nie, K. Zhao, Y. Liu et al., Metal single-site catalyst design for electrocatalytic production of hydrogen peroxide at industrial-relevant currents. Nat. Commun. **14**, 172 (2023). https://doi.org/10.1038/s41467-023-35839-z
126. C. Xiao, L. Cheng, Y. Zhu, G. Wang, L. Chen et al., Super-coordinated nickel $N_4Ni_1O_2$ site single-atom catalyst for selective H_2O_2 electrosynthesis at high current densities. Angew. Chem. Int. Ed. **61**, e202206544 (2022). https://doi.org/10.1002/anie.202206544
127. L. Li, S. Huang, R. Cao, K. Yuan, C. Lu et al., Optimizing microenvironment of asymmetric N, S-coordinated single-atom Fe via axial fifth coordination toward efficient oxygen electroreduction. Small **18**, 2105387 (2022). https://doi.org/10.1002/smll.202105387
128. L. Gong, H. Zhang, Y. Wang, E. Luo, K. Li et al., Bridge bonded oxygen ligands between approximated FeN_4 sites confer catalysts with high ORR performance. Angew. Chem. Int. Ed. **59**, 13923–13928 (2020). https://doi.org/10.1002/anie.202004534
129. Y. Guo, H. Yin, F. Cheng, M. Li, S. Zhang et al., Altering ligand microenvironment of atomically dispersed CrN_4 by axial ligand sulfur for enhanced oxygen reduction reaction in alkaline and acidic medium. Small **19**, 2206861 (2023). https://doi.org/10.1002/smll.202206861
130. S. Li, L. Xia, J. Li, Z. Chen, W. Zhang et al., Tuning structural and electronic configuration of FeN_4 via external S for enhanced oxygen reduction reaction. Energy Environ. Mater. (2023). https://doi.org/10.1002/eem2.12560
131. C. Chen, Z. Chen, J. Zhong, X. Song, D. Chen et al., Regulating electronic structure of CoN_4 with axial Co-S for promoting oxygen reduction and zn-air battery performance. Nano Res. **16**, 4211–4218 (2023). https://doi.org/10.1007/s12274-022-5164-y
132. C. Xin, W. Shang, J. Hu, C. Zhu, J. Guo et al., Integration of morphology and electronic structure modulation on atomic iron-nitrogen-carbon catalysts for highly efficient oxygen reduction. Adv. Funct. Mater. **32**, 2108345 (2021). https://doi.org/10.1002/adfm.202108345
133. Y. Han, Y. Wang, R. Xu, W. Chen, L. Zheng et al., Electronic structure engineering to boost oxygen reduction activity by controlling the coordination of the central metal. Energy Environ. Sci. **11**, 2348–2352 (2018). https://doi.org/10.1039/c8ee01481g
134. X. Zhang, L. Truong-Phuoc, X. Liao, V. Papaefthimiou, M. Pugliesi et al., Inducing atomically dispersed Cl-FeN_4 sites for ORRs in the SiO_2-mediated synthesis of highly mesoporous N-enriched C-networks. J. Mater. Chem. A **10**, 6153–6164 (2022). https://doi.org/10.1039/d1ta09519f
135. S. Ding, J.A. Barr, Q. Shi, Y. Zeng, P. Tieu et al., Engineering atomic single metal-fen(4)cl sites with enhanced oxygen-reduction activity for high-performance proton exchange membrane fuel cells. ACS Nano **16**, 15165–15174 (2022). https://doi.org/10.1021/acsnano.2c06459
136. A. Radwan, H. Jin, D. He, S. Mu, Design engineering, synthesis protocols, and energy applications of mof-derived electrocatalysts. Nano-Micro Lett. **13**, 132 (2021). https://doi.org/10.1007/s40820-021-00656-w
137. B. Ji, J. Gou, Y. Zheng, X. Pu, Y. Wang et al., Coordination chemistry of large-size yttrium single-atom catalysts for oxygen reduction reaction. Adv. Mater. **35**, 2300381 (2023). https://doi.org/10.1002/adma.202300381
138. K.M. Zhao, S. Liu, Y.Y. Li, X. Wei, G. Ye et al., Insight into the mechanism of axial ligands regulating the catalytic activity of Fe–N_4 sites for oxygen reduction reaction. Adv.

Energy Mater. **12**, 2103588 (2022). https://doi.org/10.1002/aenm.202103588

139. X. Yan, X. Xu, Q. Liu, J. Guo, L. Kang et al., Functionalization of multi-walled carbon nanotubes with iron phthalocyanine via a liquid chemical reaction for oxygen reduction in alkaline media. J. Power Sources **389**, 260–266 (2018). https://doi.org/10.1016/j.jpowsour.2018.03.042
140. G. Luo, Y. Wang, Y. Li, Two-dimensional iron-porphyrin sheet as a promising catalyst for oxygen reduction reaction: a computational study. Sci. Bull **62**, 1337–1343 (2017). https://doi.org/10.1016/j.scib.2017.08.015
141. X. She, J. Gao, Y. Gao, H. Tang, K. Li et al., Axial ligand engineering for highly efficient oxygen reduction catalysts in transition metal–N_4 doped graphene. New J. Chem. **46**, 16138–16150 (2022). https://doi.org/10.1039/d2nj03058f
142. R. Lu, C. Quan, C. Zhang, Q. He, X. Liao et al., Establishing a theoretical insight for penta-coordinated iron-nitrogen-carbon catalysts toward oxygen reaction. Nano Res. **15**, 6067–6075 (2022). https://doi.org/10.1007/s12274-022-4318-2
143. F.X. Hu, T. Hu, S. Chen, D. Wang, Q. Rao et al., Single-atom cobalt-based electrochemical biomimetic uric acid sensor with wide linear range and ultralow detection limit. Nano-Micro Lett. **13**, 7 (2021). https://doi.org/10.1007/s40820-020-00536-9
144. X. Zhu, X. Tan, K.-H. Wu, C.-L. Chiang, Y.-C. Lin et al., N, P co-coordinated Fe species embedded in carbon hollow spheres for oxygen electrocatalysis. J. Mater. Chem. A **7**, 14732–14742 (2019). https://doi.org/10.1039/c9ta03011e
145. X. Zeng, J. Shui, X. Liu, Q. Liu, Y. Li et al., Single-atom to single-atom grafting of Pt_1 onto Fe–N_4 Center: Pt_1@Fe–N–C multifunctional electrocatalyst with significantly enhanced properties. Adv. Energy Mater. **8**, 1701345 (2018). https://doi.org/10.1002/aenm.201701345
146. B. Ji, J. Gou, Y. Zheng, X. Zhou, P. Kidkhunthod et al., Metalloid-cluster ligands enabling stable and active FeN_4-Te_n motifs for the oxygen reduction reaction. Adv. Mater. **34**, 2202714 (2022). https://doi.org/10.1002/adma.202202714
147. L. Han, X. Peng, H.-T. Wang, P. Ou, Y. Mi et al., Chemically coupling SnO_2 quantum dots and MXene for efficient CO_2 electroreduction to formate and Zn–CO_2 battery. Proc. Natl. Acad. Sci. (2022). https://doi.org/10.1073/pnas.2207326119
148. M. Aresta, A. Dibenedetto, A. Angelini, Catalysis for the valorization of exhaust carbon: from CO2 to chemicals, materials, and fuels. Technological use of CO2. Chem. Rev. **114**, 1709–1742 (2014). https://doi.org/10.1021/cr4002758
149. J. Dong, Y. Cheng, Y. Li, X. Peng, R. Zhang et al., Abundant (110) facets on $PdCu_3$ alloy promote electrochemical conversion of CO_2 to CO. ACS Appl. Mater. Interfaces **14**, 41969–41977 (2022). https://doi.org/10.1021/acsami.2c09615
150. D. Xue, H. Xia, W. Yan, J. Zhang, S. Mu, Defect engineering on carbon-based catalysts for electrocatalytic CO_2 reduction. Nano-Micro Lett. **13**, 5 (2021). https://doi.org/10.1007/s40820-020-00538-7
151. X. Wu, H. Zhang, S. Zuo, J. Dong, Y. Li et al., Engineering the coordination sphere of isolated active sites to explore the intrinsic activity in single-atom catalysts. Nano-Micro Lett. **13**, 136 (2021). https://doi.org/10.1007/s40820-021-00668-6
152. J. Tuo, Y. Lin, Y. Zhu, H. Jiang, Y. Li et al., Local structure tuning in Fe-N-C catalysts through support effect for boosting CO_2 electroreduction. Appl. Catal. B: Environ. **272**, 118960 (2020). https://doi.org/10.1016/j.apcatb.2020.118960
153. H. Cheng, X. Wu, X. Li, Y. Zhang, M. Feng et al., Zeolitic imidazole framework-derived FeN_5-doped carbon as superior CO_2 electrocatalysts. J. Catal. **395**, 63–69 (2021). https://doi.org/10.1016/j.jcat.2020.12.032
154. Z. Li, J. Jiang, X. Liu, Z. Zhu, J. Wang et al., Coupling atomically dispersed Fe-N_5 sites with defective N-doped carbon boosts CO_2 electroreduction. Small **18**, 2203495 (2022). https://doi.org/10.1002/smll.202203495
155. J.R. Huang, X.F. Qiu, Z.H. Zhao, H.L. Zhu, Y.C. Liu et al., Single-product faradaic efficiency for electrocatalytic of CO2 to CO at current density larger than 1.2 A cm^{-2} in neutral aqueous solution by a single-atom nanozyme. Angew. Chem. Int. Ed. (2022). https://doi.org/10.1002/anie.202210985
156. H. Zhang, J. Li, S. Xi, Y. Du, X. Hai et al., A graphene-supported single-atom FeN_5 catalytic site for efficient electrochemical CO_2 reduction. Angew. Chem. Int. Ed. **58**, 14871–14876 (2019). https://doi.org/10.1002/anie.201906079
157. M. Zhu, J. Chen, R. Guo, J. Xu, X. Fang et al., Cobalt phthalocyanine coordinated to pyridine-functionalized carbon nanotubes with enhanced CO_2 electroreduction. Appl. Catal. B: Environ. **251**, 112–118 (2019). https://doi.org/10.1016/j.apcatb.2019.03.047
158. Y. Pan, R. Lin, Y. Chen, S. Liu, W. Zhu et al., Design of single-atom Co-N_5 catalytic site: a robust electrocatalyst for CO_2 reduction with nearly 100% co selectivity and remarkable stability. J. Am. Chem. Soc. **140**, 4218–4221 (2018). https://doi.org/10.1021/jacs.8b00814
159. X. Li, S.-G. Han, W. Wu, K. Zhang, B. Chen et al., Convergent paired electrosynthesis of dimethyl carbonate from carbon dioxide enabled by designing the superstructure of axial oxygen coordinated nickel single-atom catalysts. Energy Environ. Sci. **16**, 502–512 (2023). https://doi.org/10.1039/d2ee03022e
160. M. Huang, B. Deng, X. Zhao, Z. Zhang, F. Li et al., Template-sacrificing synthesis of well-defined asymmetrically coordinated single-atom catalysts for highly efficient CO_2 electrocatalytic reduction. ACS Nano **16**, 2110–2119 (2022). https://doi.org/10.1021/acsnano.1c07746
161. J. Wang, Q. Hao, H. Zhong, K. Li, X. Zhang, Ligand centered electrocatalytic efficient CO_2 reduction reaction at low overpotential on single-atom Ni regulated molecular catalyst. Nano Res. **15**, 5816–5823 (2022). https://doi.org/10.1007/s12274-022-4197-6
162. X. Chen, W. Liu, Y. Sun, T. Tan, C.X. Du et al., KOH-enabled axial-oxygen coordinated Ni single-atom catalyst for efficient electrocatalytic CO_2 reduction. Small Methods **7**, 2201311 (2023). https://doi.org/10.1002/smtd.202201311
163. T. Zhang, X. Han, H. Liu, M. Biset-Peiró, J. Li et al., Site-specific axial oxygen coordinated FeN_4 active sites for highly selective electroreduction of carbon dioxide. Adv. Funct.

Mater. **32**, 2111446 (2022). https://doi.org/10.1002/adfm.202111446

164. X. Wang, Y. Pan, H. Ning, H. Wang, D. Guo et al., Hierarchically micro- and meso-porous Fe-N_4O-doped carbon as robust electrocatalyst for CO_2 reduction. Appl. Catal. B: Environ. **266**, 118630 (2020). https://doi.org/10.1016/j.apcatb.2020.118630
165. Z. Chen, A. Huang, K. Yu, T. Cui, Z. Zhuang et al., Fe_1N_4–O_1 site with axial Fe–O coordination for highly selective CO_2 reduction over a wide potential range. Energy Environ. Sci. **14**, 3430–3437 (2021). https://doi.org/10.1039/d1ee00569c
166. Y. Deng, J. Zhao, S. Wang, R. Chen, J. Ding et al., Operando spectroscopic analysis of axial oxygen-coordinated single-Sn-atom sites for electrochemical CO_2 reduction. J. Am. Chem. Soc. **145**, 7242–7251 (2023). https://doi.org/10.1021/jacs.2c12952
167. Y. Wu, C. Chen, X. Yan, X. Sun, Q. Zhu et al., Boosting CO_2 electroreduction over a cadmium single-atom catalyst by tuning of the axial coordination structure. Angew. Chem. Int. Ed. **60**, 20803–20810 (2021). https://doi.org/10.1002/anie.202105263
168. C. Hu, Y. Zhang, A. Hu, Y. Wang, X. Wei et al., Near- and long-range electronic modulation of single metal sites to boost CO_2 electrocatalytic reduction. Adv. Mater. **35**, 2209298 (2023). https://doi.org/10.1002/adma.202209298
169. Z. Li, R. Wu, S. Xiao, Y. Yang, L. Lai et al., Axial chlorine coordinated iron-nitrogen-carbon single-atom catalysts for efficient electrochemical CO_2 reduction. Chem. Eng. J. **430**, 132882 (2022). https://doi.org/10.1016/j.cej.2021.132882
170. B. Zhang, J. Zhang, J. Shi, D. Tan, L. Liu et al., Manganese acting as a high-performance heterogeneous electrocatalyst in carbon dioxide reduction. Nat. Commun. **10**, 2980 (2019). https://doi.org/10.1038/s41467-019-10854-1
171. J.-X. Peng, W. Yang, Z. Jia, L. Jiao, H.-L. Jiang, Axial coordination regulation of MOF-based single-atom Ni catalysts by halogen atoms for enhanced CO_2 electroreduction. Nano Res. **15**, 10063–10069 (2022). https://doi.org/10.1007/s12274-022-4467-3
172. C. Zhang, S. Yang, J. Wu, M. Liu, S. Yazdi et al., Electrochemical CO_2 reduction with atomic iron-dispersed on nitrogen-doped graphene. Adv. Energy Mater. **8**, 1703487 (2018). https://doi.org/10.1002/aenm.201703487
173. Y. Li, B. Wei, Z. Li, L. Fan, Q. Jiang et al., Morphological attributes govern CO_2 reduction on mesoporous carbon nanosphere with embedded axial Co-N_5 sites. (2021). Preprint (Version 1) available at Research Square. https://doi.org/10.21203/rs.3.rs-999257/v1
174. X. Hu, S. Yao, L. Chen, X. Zhang, M. Jiao et al., Understanding the role of axial O in CO_2 electroreduction on NiN_4 single-atom catalysts: via simulations in realistic electrochemical environment. J. Mater Chem. A **9**, 23515–23521 (2021). https://doi.org/10.1039/D1TA07791K
175. D. Zhou, X. Li, H. Shang, F. Qin, W. Chen, Atomic regulation of metal-organic framework derived carbon-based single-atom catalysts for the electrochemical CO_2 reduction reaction. J. Mater. Chem. A **9**, 23382–23418 (2021). https://doi.org/10.1039/d1ta06915b
176. J. Wang, M. Zheng, X. Zhao, W. Fan, Structure-performance descriptors and the role of the axial oxygen atom on M-N_4–C single-atom catalysts for electrochemical CO_2 reduction. ACS Catal. **12**, 5441–5454 (2022). https://doi.org/10.1021/acscatal.2c00429
177. J. Wang, H. Li, S. Liu, Y. Hu, J. Zhang et al., Turning on Zn 4s electrons in a N_2-Zn-B_2 configuration to stimulate remarkable ORR performance. Angew. Chem. Int. Ed. **60**, 181–185 (2021). https://doi.org/10.1002/ange.202009991
178. X. Sun, Y. Tuo, C. Ye, C. Chen, Q. Lu et al., Phosphorus induced electron localization of single iron sites for boosted CO_2 electroreduction reaction. Angew. Chem. Int. Ed. **60**, 23614–23618 (2021). https://doi.org/10.1002/anie.202110433
179. L. Sun, V. Reddu, T. Su, X. Chen, T. Wu et al., Effects of axial functional groups on heterogeneous molecular catalysts for electrocatalytic CO_2 reduction. Small Struct. **2**, 2100093 (2021). https://doi.org/10.1002/sstr.202100093
180. M. Ma, Q. Tang, Axial coordination modification of M-N_4 single-atom catalysts to regulate the electrocatalytic CO_2 reduction reaction. J. Mater. Chem. C **10**, 15948–15956 (2022). https://doi.org/10.1039/d2tc02467e
181. Y. Liu, D. Wang, B. Yang, Z. Li, X. Peng et al., Efficiently electrochemical CO_2 reduction on molybdenum-nitrogen-carbon catalysts with optimized p-block axial ligands. Chem. Eng. Sci. **273**, 118638 (2023). https://doi.org/10.1016/j.ces.2023.118638
182. L. Zhang, L. Han, H. Liu, X. Liu, J. Luo, Potential-cycling synthesis of single platinum atoms for efficient hydrogen evolution in neutral media. Angew. Chem. Int. Ed. **129**, 13882–13886 (2017). https://doi.org/10.1002/ange.201706921
183. L. Zhang, Y. Yang, M.A. Ziaee, K. Lu, R. Wang, Nanohybrid of carbon quantum dots/molybdenum phosphide nanoparticle for efficient electrochemical hydrogen evolution in alkaline medium. ACS Appl. Mater. Interfaces **10**, 9460–9467 (2018). https://doi.org/10.1021/acsami.8b00211
184. Y. Xu, X. Zhang, Y. Liu, R. Wang, Y. Yang et al., A critical review of research progress for metal alloy materials in hydrogen evolution and oxygen evolution reaction. Environ. Sci. Pollut. Res. **30**, 11302–11320 (2023). https://doi.org/10.1007/s11356-022-24728-5
185. Y. Shi, Z.-R. Ma, Y.-Y. Xiao, Y.-C. Yin, W.-M. Huang et al., Electronic metal–support interaction modulates single-atom platinum catalysis for hydrogen evolution reaction. Nat. Commun. **12**, 3021 (2021). https://doi.org/10.1038/s41467-021-23306-6
186. P. Zhu, X. Xiong, D. Wang, Regulations of active moiety in single atom catalysts for electrochemical hydrogen evolution reaction. Nano Res. **15**, 5792–5815 (2022). https://doi.org/10.1007/s12274-022-4265-y
187. D. Liu, G. Xu, H. Yang, H. Wang, B.Y. Xia, Rational design of transition metal phosphide-based electrocatalysts for hydrogen evolution. Adv. Funct. Mater. **33**, 2208358 (2023). https://doi.org/10.1002/adfm.202208358

188. X.P. Yin, H.J. Wang, S.F. Tang, X.L. Lu, M. Shu et al., Engineering the coordination environment of single-atom platinum anchored on graphdiyne for optimizing electrocatalytic hydrogen evolution. Angew. Chem. Int. Ed. **57**, 9382–9386 (2018). https://doi.org/10.1002/anie.201804817
189. M. Li, M. Wang, D. Liu, Y. Pan, S. Liu et al., Atomically-dispersed NiN_4-Cl active sites with axial Ni–Cl coordination for accelerating electrocatalytic hydrogen evolution. J. Mater. Chem. A **10**, 6007–6015 (2022). https://doi.org/10.1039/d1ta08287f
190. Z. Li, B. Li, M. Yu, C. Yu, P. Shen, Amorphous metallic ultrathin nanostructures: a latent ultra-high-density atomic-level catalyst for electrochemical energy conversion. Int. J. Hydrog. Energy **47**, 26956–26977 (2022). https://doi.org/10.1016/j.ijhydene.2022.06.049
191. J. Wang, S.-J. Kim, J. Liu, Y. Gao, S. Choi et al., Redirecting dynamic surface restructuring of a layered transition metal oxide catalyst for superior water oxidation. Nat. Catal. **4**, 212–222 (2021). https://doi.org/10.1038/s41929-021-00578-1
192. B. Cheng, K. Kong, L. Zhang, R. Sa, T. Gu et al., Accelerating water oxidation kinetics via synergistic in-layer modification and interlayer reconstruction over hetero-epitaxial Fe-Mn-O nanosheets. Chem. Eng. J. **441**, 136122 (2022). https://doi.org/10.1016/j.cej.2022.136122
193. J. Tian, F. Jiang, D. Yuan, L. Zhang, Q. Chen et al., Electric-field assisted in situ hydrolysis of bulk metal-organic frameworks (MOFs) into ultrathin metal oxyhydroxide nanosheets for efficient oxygen evolution. Angew. Chem. Int. Ed. **59**, 13101–13108 (2020). https://doi.org/10.1002/anie.202004420
194. L. Zhang, T. Mi, M.A. Ziaee, L. Liang, R. Wang, Hollow POM@ MOF hybrid-derived porous Co_3O_4/$CoMoO_4$ nanocages for enhanced electrocatalytic water oxidation. J. Mater. Chem. A **6**, 1639–1647 (2018). https://doi.org/10.1039/C7TA08683K
195. J. Wang, L. Han, B. Huang, Q. Shao, H.L. Xin et al., Amorphization activated ruthenium-tellurium nanorods for efficient water splitting. Nat. Commun. **10**, 5692 (2019). https://doi.org/10.1038/s41467-019-13519-1
196. L. Han, P. Ou, W. Liu, X. Wang, H.-T. Wang et al., Design of Ru–Ni diatomic sites for efficient alkaline hydrogen oxidation. Sci. Adv. (2022). https://doi.org/10.1126/sciadv.abm377
197. W.H. Lee, Y.J. Ko, J.Y. Kim, B.K. Min, Y.J. Hwang et al., Single-atom catalysts for the oxygen evolution reaction: recent developments and future perspectives. Chem. Commun. **56**, 12687–12697 (2020). https://doi.org/10.1039/d0cc04752j
198. Q. Deng, J. Zhao, T. Wu, G. Chen, H.A. Hansen et al., 2D transition metal–TCNQ sheets as bifunctional single-atom catalysts for oxygen reduction and evolution reaction (ORR/OER). J. Catal. **370**, 378–384 (2019). https://doi.org/10.1016/j.jcat.2018.12.012
199. Y.L. Zhang, B. Liu, Y.K. Dai, Y.F. Xia, P. Guo et al., Electronic delocalization regulates the occupancy and energy level of Co $3d_{z2}$ orbitals to enhance bifunctional oxygen catalytic activity. Adv. Funct. Mater. **32**, 2209499 (2022). https://doi.org/10.1002/adfm.202209499
200. T. Li, T. Lu, H. Zhong, S. Xi, M. Zhang et al., Atomically dispersed V-O_2N_3 sites with axial V–O coordination on multichannel carbon nanofibers achieving superior electrocatalytic oxygen evolution in acidic media. Adv. Energy Mater. **13**, 2203274 (2022). https://doi.org/10.1002/aenm.202203274
201. Y. Liu, S. Zhang, C. Jiao, H. Chen, G. Wang et al., Axial phosphate coordination in co single atoms boosts electrochemical oxygen evolution. Adv. Sci. **10**, 2206107 (2023). https://doi.org/10.1002/advs.202206107
202. Y. Yang, C. Hu, J. Shan, C. Cheng, L. Han et al., Electrocatalytically activating and reducing N_2 molecule by tuning activity of local hydrogen radical. Angew. Chem. Int. Ed. **62**, e202300989 (2023). https://doi.org/10.1002/anie.202300989
203. Y. Huang, C. Tang, Q. Li, J. Gong, Computational studies for boosting nitrate electroreduction activity of Fe-N_4-C Single-Atom catalyst via axial fifth ligand. Appl. Surf. Sci. **616**, 156440 (2023). https://doi.org/10.1016/j.apsusc.2023.156440
204. L. Liu, T. Xiao, H. Fu, Z. Chen, X. Qu et al., Construction and identification of highly active single-atom Fe_1-NC catalytic site for electrocatalytic nitrate reduction. Appl. Catal. B: Environ. **323**, 122181 (2023). https://doi.org/10.1016/j.apcatb.2022.122181
205. A. Wu, J. Yang, B. Xu, X.-Y. Wu, Y. Wang et al., Direct ammonia synthesis from the air via gliding arc plasma integrated with single atom electrocatalysis. Appl. Catal. B: Environ. **299**, 120667 (2021). https://doi.org/10.1016/j.apcatb.2021.120667